



University of Kentucky
UKnowledge

Theses and Dissertations--Mechanical
Engineering

Mechanical Engineering


2022

In-Situ Characterization of Burr Formation in Finish Machining of Inconel 718

Hamzah M. Zannoun

University of Kentucky, hzannoun@gmail.com

Author ORCID Identifier:

 <https://orcid.org/0000-0002-9730-1285>

Digital Object Identifier: <https://doi.org/10.13023/etd.2022.418>

[Right click to open a feedback form in a new tab to let us know how this document benefits you.](#)

Recommended Citation

Zannoun, Hamzah M., "In-Situ Characterization of Burr Formation in Finish Machining of Inconel 718" (2022). *Theses and Dissertations--Mechanical Engineering*. 205.
https://uknowledge.uky.edu/me_etds/205

This Master's Thesis is brought to you for free and open access by the Mechanical Engineering at UKnowledge. It has been accepted for inclusion in Theses and Dissertations--Mechanical Engineering by an authorized administrator of UKnowledge. For more information, please contact UKnowledge@lsv.uky.edu.

STUDENT AGREEMENT:

I represent that my thesis or dissertation and abstract are my original work. Proper attribution has been given to all outside sources. I understand that I am solely responsible for obtaining any needed copyright permissions. I have obtained needed written permission statement(s) from the owner(s) of each third-party copyrighted matter to be included in my work, allowing electronic distribution (if such use is not permitted by the fair use doctrine) which will be submitted to UKnowledge as Additional File.

I hereby grant to The University of Kentucky and its agents the irrevocable, non-exclusive, and royalty-free license to archive and make accessible my work in whole or in part in all forms of media, now or hereafter known. I agree that the document mentioned above may be made available immediately for worldwide access unless an embargo applies.

I retain all other ownership rights to the copyright of my work. I also retain the right to use in future works (such as articles or books) all or part of my work. I understand that I am free to register the copyright to my work.

REVIEW, APPROVAL AND ACCEPTANCE

The document mentioned above has been reviewed and accepted by the student's advisor, on behalf of the advisory committee, and by the Director of Graduate Studies (DGS), on behalf of the program; we verify that this is the final, approved version of the student's thesis including all changes required by the advisory committee. The undersigned agree to abide by the statements above.

Hamzah M. Zannoun, Student

Dr. Julius M. Schoop, Major Professor

Dr. Jesse B. Hoagg, Director of Graduate Studies

IN-SITU CHARACTERIZATION OF BURR FORMATION IN FINISH MACHINING
OF INCONEL 718

THESIS

A thesis submitted in partial fulfillment of
the requirements for the degree of Master of Science in
Mechanical Engineering in the College of Engineering
at the University of Kentucky

By

Hamzah M. Zannoun

Lexington, Kentucky

Director: Dr. Julius M. Schoop, Professor of Mechanical Engineering

Lexington, Kentucky

2022

Copyright © Hamzah Zannoun 2022

ABSTRACT OF THESIS

IN-SITU CHARACTERIZATION OF BURR FORMATION IN FINISH MACHINING OF INCONEL 718

One of the undesirable byproducts that occur during the machining process is the development of burrs, which are defined as rough excess material that forms around the geometric discontinuities of a part. Burrs are especially problematic because they have negative impacts across the triple bottom line: economic, environmental, societal. For one, they are expensive to remove because the deburring process is entirely manual and requires skill. Further, burr material is typically discarded which is adding to the already mounting waste generated from machining such as in coolant and chip disposal. Lastly, there are many societal implications, such as operator injury during assembly and the failure of parts in service because of leftover burrs that turned into stress concentrations.

Therefore, optimizing the machining process to minimize burrs and promote sustainable manufacturing is a central challenge for manufacturers today. However, the burr formation mechanism is complex, and research on the phenomenon is scarce. The current state of the art focuses almost exclusively on drilling and micro-milling processes, with very little work investigating burr formation in the conventional machining processes of turning and milling. Research as it pertains to materials that are difficult-to-machine like nickel and titanium-based superalloys is even less common, as most of the literature focuses on softer materials like aluminum and steel alloys. Superalloys are especially crucial to the aerospace industry, comprising most of the components in jet engines.

Thus, the objective of this study was to characterize burr formation for nickel-based superalloy Inconel 718 using a custom-built in-situ testbed capable of ultra-high-speed imaging in orthogonal cuts. Experiments were carried out to measure the variation in burr development with respect to several cutting parameters: uncut chip thickness, tool-wear, and cutting speed. Firstly, the exit and side burr geometry were measured after each machining trial for a variety of different metrics. Results showed that all cutting parameters have an influence on the burr geometry, although not every cutting parameter had statistical significance on certain burr metrics. For instance, it was found that side burrs were much more sensitive to tool-wear than exit burrs. Then, by combining digital image correlation (DIC) with a physics-based model, the flow stress was calculated during exit burr

formation and results revealed that the stress at the exit burr root was approximately equal to the flow stress. Finally, this study investigates the fracture phenomenon during exit burr formation—it was found that besides the requirement of high strain rate and depth of cut, negative exit burrs, there is a microstructural size effect, which had not been reported by prior work.

KEYWORDS: Burr Formation, Finish Machining, Inconel 718, Tool-Wear, In-Situ Characterization, Digital Image Correlation (DIC)

Hamzah M. Zannoun

(Name of Student)

December 1st, 2022

Date

IN-SITU CHARACTERIZATION OF BURR FORMATION IN FINISH
MACHINING OF INCONEL 718

By
Hamzah M. Zannoun

Dr. Julius M. Schoop

Director of Thesis

Dr. Jesse B. Hoagg

Director of Graduate Studies

December 1st, 2022

Date

ACKNOWLEDGMENTS

I would like to start by thanking my amazing advisor, Professor Julius Schoop. I first approached Dr. Schoop because I was interested in machining, given my passion for automotive and aerospace engine manufacturing. Despite my limited knowledge of the subject, he was still very enthusiastic about me joining the team. Throughout my entire time working under him, he would always come in with a smile on his face—I have yet to ever see him in a bad mood. Despite his busy schedule, he always makes time for students to discuss research, give professional advice, and get to know them on a more personal level. To me, Dr. Schoop was far more than just an academic advisor. He was also a mentor, role model, and friend. I felt I could really be myself around him and selecting him as my advisor was honestly the best decision of my academic career. Thank you, Dr. Schoop, for being the best advisor a student could ask for.

Next, I would like to thank my two committee members, Professor I.S. Jawahir and Professor Fazleena Badurdeen. Dr. Jawahir is one of the humblest and kindest professors I have ever met. Despite his immense reputation, he is extremely friendly and personable with everyone he meets, especially students. I had many enlightening conversations with Dr. Jawahir, and I could tell that he was invested in my success. He is a shining example of a great leader, making ISM such an accommodating and enjoyable place to work. Dr. Badurdeen is another professor I have an incredible amount of respect for. I have had the pleasure of taking four classes with Dr. Badurdeen, more than any other professor during my time at UK, and every time I walked away with invaluable skills and knowledge on sustainable manufacturing. I thank you both for everything you do at ISM, it has been an honor knowing you personally and professionally. Big thanks also go out to Dana Harrod for everything she does—I could not imagine ISM without her. I would also like to show my appreciation for Professor John Balk and Dr. Mike Detisch for allowing me to use equipment at the EMC, which improved the quality of my thesis work tremendously. Special recognition goes out to Professor Scott Stephens, who I learned a lot from during my time as his TA.

There are a great many individuals that I met during my time as a graduate student that I would like to thank, starting of course with my fellow collaborators in the Schoop

Research Group: E-Lexus Thornton, Mehedi Hasan, Victor Sodje, David Adeniji, Gatewood Arnold, Guher Toker, Avery Hartley, Dan Caudill, and Kyle Olige. It was a pleasure working with you on papers and research projects, but I am also grateful for all the fun conversations and good times we had. I am proud to call you all my friends. Special thanks go out to the undergraduate students of the group: Zach Rohrer, Naol Wolde, Jaden Kim, Jakob Eichhorn, and Connor Vomero, who were all instrumental in assisting me with my research. I would like to recognize Zach Rohrer in particular, who went above and beyond in aiding me during my experiments, saving me countless hours. I also want to acknowledge all my other colleagues from ISM: Gisele Guedes, Syed Ibn Mohsin, and Yangyang Wu. There are also the two exchange students from Germany: Matthias Wimmer and German Gonzalez Fernandez. It was awesome getting to know you guys during the short time that you were here. Furthermore, I would like to give sincerest appreciation to my other longtime friends: Seth Bottom, Korbin Jackson, Evan Lindsay, Bruno Tacchi, John Hinkebein, Hector Rosa, and Joe Gomez. Thank you, guys, for sticking with me through the years.

Last but certainly not least, I give utmost thanks to my family: my younger brother, Hisham, but particularly my parents, who paved the way for me to have a stress-free experience in college. They provided me with all the support I needed to succeed not only in school but also in life, and I could not have done any of this without them. They sacrificed a lot so that I could have a bright future, and for that I am eternally grateful. Thank you for everything, mama and baba, I hope I made you proud.

TABLE OF CONTENTS

| | |
|--------------------------------------------------------------------|------|
| ABSTRACT OF THESIS | II |
| ACKNOWLEDGMENTS | III |
| TABLE OF CONTENTS..... | V |
| LIST OF TABLES | VII |
| LIST OF FIGURES | VIII |
| CHAPTER 1. Introduction..... | 1 |
| CHAPTER 2. Background and Literature Review | 5 |
| 2.1 Machining of Nickel-Based Superalloys | 5 |
| 2.2 Effects of Cutting Conditions on Surface Integrity | 7 |
| 2.2.1 Cutting Tool Condition | 10 |
| 2.2.2 Surface Roughness..... | 13 |
| 2.2.3 Machining-Induced Residual Stress | 17 |
| 2.2.4 Microhardness and Microstructure | 20 |
| 2.3 Burr Formation..... | 25 |
| 2.3.1 Types of Burrs and Formation Mechanism | 26 |
| 2.3.2 Effects of Cutting Conditions on Burrs | 30 |
| CHAPTER 3. Experimental Setup and Measurement | 36 |
| 3.1 In-Situ Testbed for High-Speed Imaging of Orthogonal Cuts..... | 36 |
| 3.2 Sample and Tool Preparation..... | 39 |
| 3.2.1 Sample Polishing and Etching | 39 |
| 3.2.2 Tool Sharpening and Imposition of Flank-Wear | 40 |
| 3.3 Force Measurement..... | 42 |
| 3.4 Displacement Measurement..... | 43 |
| 3.5 Optical Microscopy for Capturing Burrs | 46 |
| CHAPTER 4. Characterization of Burr Geometry | 47 |
| 4.1 Exit Burr Development | 47 |
| 4.1.1 Effects of Uncut Chip Thickness on Exit Burrs..... | 50 |
| 4.1.2 Effects of Tool-Wear on Exit Burrs..... | 52 |
| 4.1.3 Effects of Cutting Speed on Exit Burrs..... | 53 |

| | |
|--------------------------------------------------------------|----|
| 4.2 Side Burr Development..... | 53 |
| 4.2.1 Effects of Uncut Chip Thickness on Side Burrs | 55 |
| 4.2.2 Effects of Tool-Wear on Side Burrs | 56 |
| 4.2.3 Effects of Cutting Speed on Side Burrs | 57 |
| CHAPTER 5. Displacement and Stress Analysis | 59 |
| 5.1 Subsurface Displacement at Exit Burr Root | 59 |
| 5.2 Subsurface Stress at Exit Burr Root..... | 60 |
| CHAPTER 6. Exit Burr Fracture Analysis | 65 |
| 6.1 Effects of Cutting Parameters on Exit Burr Fracture..... | 65 |
| 6.2 Effects of Tool-Wear on Exit Burr Fracture | 68 |
| 6.3 Effects of Microstructure on Exit Burr Fracture | 69 |
| CHAPTER 7. Conclusions and Outlook..... | 71 |
| 7.1 Summary of Findings..... | 71 |
| 7.2 Future Work | 73 |
| APPENDIX..... | 75 |
| REFERENCES | 79 |
| VITA..... | 91 |

LIST OF TABLES

| | |
|------------------------------------------------------------------------------|----|
| Table 2-1. Positive Exit Burr Metrics Proposed by Ko and Dornfeld [82] | 28 |
| Table 3-1. Experimental matrix for in-situ trials | 38 |
| Table 3-2. Polishing recipe for Inconel 718 in-situ workpiece..... | 40 |

LIST OF FIGURES

| | |
|-------------------------------------------------------------------------------------------------------------------------------------------------------------------------------------------------------------------------------------------------------------------------------------------------------------------------------------------------------------------------------------------------------------------------------------------------------------------|----|
| Figure 1-1. Burrs in (a) milling (reproduced from [8] under the CC license); (b) turning (reproduced from [9] with permission of Springer Nature, License Number 5440320873157); (c) drilling (reproduced from [5, 8, 10] under the CC license and with permission of Springer Nature and Elsevier, License Numbers 5440370956751 and 5440371134411) | 3 |
| Figure 1-2. Framework of factors affecting total machining performance (reproduced from [6] with permission of ASME) | 4 |
| Figure 2-1. Correlation between material properties and machining defects (reproduced from [15] with permission of Springer Nature, License Number 5427931460106)..... | 5 |
| Figure 2-2. Tool-wear modes and mechanisms. Images reproduced from [19-25] with permission of Elsevier and Springer Nature, License Numbers 5440380404232, 5440381087265, 5440400334357, 5440381365393, 5440390090010, 5440390338603, 5440391308844..... | 7 |
| Figure 2-3. Cutting force variation with cutting speed for Inconel 718 (reproduced from [24, 28] with permission of Springer Nature and Elsevier, License Numbers 5427940633570 and 5427960339270) | 8 |
| Figure. 2-4 Cutting temperature variation with cutting speed and feed rate (reproduced from [19] with permission of Elsevier, License Number 5427950598778) | 9 |
| Figure 2-5. Change in flank-wear with cutting speed for Inconel 718 under (a) dry conditions (reproduced from [24] with permission of Springer Nature, License Number 5427940633570) and (b) wet conditions (reproduced from [39] under the CC-BY-NC-ND License)..... | 11 |
| Figure 2-6. (a) Forces in relation to feed rate and duration of cut (reproduced from [42] with permission of Elsevier, License Number 5427961127336); (b) flank-wear in relation to feed rate (reproduced from [19, 45] with permission of Elsevier, License Numbers 5427960912537 and 5427950598778); (c) flank-wear with number of impacts/cutting length (reproduced from [44] with permission of Elsevier, License Number 5428000043935) for Inconel 718..... | 13 |
| Figure 2-7. Surface roughness variation with tool-wear (reproduced from [24] with permission of Springer Nature, License Number 5427940633570) | 14 |
| Figure 2-8. Surface roughness variation with cutting speed for (a) bainite steel (reproduced from [54] with permission of Elsevier, License Number 5427961284848) and (b) Inconel 718 (reproduced from [39] under the CC-BY-NC-ND License)..... | 16 |
| Figure 2-9. Effect of feed rate on surface roughness in CT and UAT for Inconel 718 and Inconel 625 (reproduced from [32] under the CC-BY License)..... | 16 |

| | |
|--------------------------------------------------------------------------------------------------------------------------------------------------------------------------------------------------------------------------------------|----|
| Figure 2-10. RS profile at various feed rates for Inconel 718 (reproduced from [31] with permission of Elsevier, License Number 5427970504660)..... | 18 |
| Figure 2-11. Fatigue life variation with feed rate for face milling of Inconel 718 (reproduced from [53] with permission of Springer Nature, License Number 5427970703568) | 20 |
| Figure 2-12. The three grain deformation zones (reproduced from [15] with permission of Springer Nature, License Number 5427971400371, originally modified from [72] with permission of Elsevier, License Number 5427971266957)..... | 22 |
| Figure 2-13. Change in microhardness with varying cutting speed for Ni-alloy FGH95 (reproduced from [74] with permission of Springer Nature, License Number 5427980085840) | 23 |
| Figure 2-14. Variation in deformation depth with respect to various parameters for Inconel 718 (reproduced from [41] with permission of Taylor & Francis) | 24 |
| Figure 2-15. High-speed in-situ images of positive exit burr (a) initiation; (b) development; (c) final formation (after cut) at $VB = 0 \mu\text{m}$, $h = 80 \mu\text{m}$, $v_c = 6 \text{ m/min}$ | 27 |
| Figure 2-16. Schematic of exit burr development [82]..... | 28 |
| Figure 2-17. Process of fracture in negative exit burr formation ($VB = 0 \mu\text{m}$, $h = 80 \mu\text{m}$, $v_c = 60 \text{ m/min}$) | 29 |
| Figure 2-18. Change in burr height with number of holes drilled for stainless steel 304 (reproduced from [100] with permission of Elsevier, License Number 5427980351490). | 31 |
| Figure 2-19. Effect of feed rate and cutting speed on burr height for stainless steel 304 (reproduced from [100] with permission of Elsevier, License Number 5427980351490). | 34 |
| Figure 2-20. Effect of grain size and feed rate on burr formation for wrought Alloy 718 (reproduced from [111] with permission of Springer Nature, License Number 5427980508001) | 34 |
| Figure 3-1. In-situ testbed used for physics-informed and data-driven characterization of machining processes | 37 |
| Figure 3-2. Images of (a) geometry and (b) microstructure of slotted and polished Inconel 718 in-situ workpiece sample | 39 |
| Figure 3-3. Flank-wear ($VB = 150 \mu\text{m}$) and hone ($r_\beta \sim 30 \mu\text{m}$) for a worn tool | 42 |
| Figure 3-4. Calculation of force averages in MATLAB..... | 43 |

| | |
|---------------------------------------------------------------------------------------------------------------------------------------------------------------------------------------------------------------------------------------------------------------------------|----|
| Figure 3-5. In-situ imaging procedure for conducting subsurface analysis with DIC (reproduced from [115] with permission of Springer Nature, License Number 5427980654590) | 44 |
| Figure 3-6. Keyence VHX-7000 digital microscope used for scanning and measuring burrs | 46 |
| Figure 4-1. Schematic representation of exit burr parameters: (a) thickness (b_t); (b) height (b_h); (c) initiation distance (ω); (d) inclination angle (ψ); (e) initial negative shear angle (β_0); (f) initiation angle (η)..... | 47 |
| Figure 4-2. Visual of burr initiation point from a vertical view of the machined surface.. | 48 |
| Figure 4-3. Average profiles for exit burr thickness (b_t) at (a) $v_c = 6$ m/min (significant effect of tool-wear) and (b) $v_c = 60$ m/min (no significant effect of tool-wear) | 49 |
| Figure 4-4. Average profiles for exit burr height (b_h) at (a) $v_c = 6$ m/min and (b) $v_c = 60$ m/min. No significant effect of tool-wear..... | 49 |
| Figure 4-5. Average profiles for inclination angle (ψ) at (a) $v_c = 6$ m/min and (b) $v_c = 60$ m/min. No significant effect of tool-wear..... | 49 |
| Figure 4-6. Average profiles for initiation distance (ω) at (a) $v_c = 6$ m/min and (b) $v_c = 60$ m/min. Significant effect of tool-wear..... | 50 |
| Figure 4-7. Average profiles for initial negative shear angle (β_0) at (a) $v_c = 6$ m/min and (b) $v_c = 60$ m/min. No significant effect of tool-wear | 50 |
| Figure 4-8. Average profiles for initiation angle (η) at (a) $v_c = 6$ m/min and (b) $v_c = 60$ m/min. No significant effect of tool-wear..... | 50 |
| Figure 4-9. Side view of cavity at the top of exit burrs observed at high uncut chip thickness ($h = 80 \mu\text{m}$) and high cutting speed ($v_c = 60$ m/min) | 51 |
| Figure 4-10. Average profiles for side burr thickness (sb_t) at (a) $v_c = 6$ m/min and (b) $v_c = 60$ m/min. Significant effect of tool-wear..... | 54 |
| Figure 4-11. Overview of side burr thickness (sb_t) images at (a) $v_c = 6$ m/min and (b) $v_c = 60$ m/min..... | 54 |
| Figure 4-12. Overview of side burr height (sb_h) images at (a) $v_c = 6$ m/min and (b) $v_c = 60$ m/min | 55 |
| Figure 5-1. Vertical displacement (δ_v) calculated at exit burr root from DIC displacement fields..... | 60 |

| | |
|-------------------------------------------------------------------------------------------------------------------------------------------------------------------------------------------------------------------------------------------------------------------------------------------------------------------|----|
| Figure 5-2. Schematic illustration of the process for calibrating contact width (2a): (a) modeling results of von Mises stress; (b) DIC displacement field (reproduced from [115] with permission of Springer Nature, License Number 5427980654590) | 61 |
| Figure 5-3. Vertical displacement field from DIC analysis overlaid on in-situ optical micrographs for (a) $v_c = 6$ m/min and (b) $v_c = 60$ m/min; Model-generated von Mises (σ_{VM}) stress fields overlaid on DIC vertical displacement fields for (c) $v_c = 6$ m/min and (d) $v_c = 60$ m/min | 62 |
| Figure 5-4. Model-analyzed normalized stress at exit burr root | 63 |
| Figure 6-1. Positive to negative exit burr transition for $VB = 0$ μm , $h = 80$ μm , $v_c = 60$ m/min | 66 |
| Figure 6-2. Vertical view of positive to negative exit burr transition at $VB = 0$ μm , $h = 80$ μm , $v_c = 60$ m/min for (a) Trial 1 and (b) Trial 2 | 67 |
| Figure 6-3. Negative burr formation development at $VB = 0$ μm , $h = 80$ μm , $v_c = 60$ m/min with (a) true uncut chip thickness (h_{true}) and (b) exit burr thickness (b_t)..... | 68 |
| Figure 6-4. Vertical view of positive to negative exit burr transition at $h = 80$ μm , $v_c = 60$ m/min for (a) $VB = 50$ μm and (b) $VB = 150$ μm | 69 |
| Figure 6-5. Relationship between and grain size (d_v) and negative exit burr size (b_t).... | 70 |
| Figure A1. MATLAB script for force average calculation..... | 75 |
| Figure A2. MATLAB script for automatic image capture using in-situ testbed vertical microscope | 78 |

Machining is the world's largest manufacturing process, accounting for 5% of the global GDP [1]. Machining is a subtractive process where material is removed using a cutting tool from a rotating or stationary workpiece, with the two main machining processes being turning and milling. Turning involves a rotating workpiece with a tool that is fed horizontally along the axis (longitudinal turning) or along the face (face turning). Milling involves a stationary workpiece that is cut with a rotating tool that follows a programmed path. After primary processing (forging/casting), there is secondary processing, which may involve rough machining—in rough machining (roughing), excessive amounts of material are removed to obtain the desired shape. After secondary processing comes finish machining (finishing). In finishing, minimal amounts of material are removed to improve the surface finish of the workpiece to meet the desired quality specifications such as surface roughness and residual stress (RS). Given the wasteful nature of roughing and considering recent trends towards near-net-shape manufacturing (e.g., via precision casting or additive manufacturing), finishing is becoming increasingly more relevant in industry and will thus be the focus of this work.

Machining is especially prevalent in the aerospace industry for producing jet engine components, which are usually comprised of resilient materials known as so-called superalloys. Most superalloys are nickel-based, and the most prevalent is Inconel 718 [2], which is the focus of this study. Nickel-based superalloys (Ni-alloys) are metals capable of withstanding elevated temperatures because of their excellent material properties such as high yield strength, high hardness, and wear resistance, making them ideal for the extreme environment of jet engines. It is these attributes, however, that make them difficult to machine. For instance, low thermal conductivity leads to the buildup of high temperatures at the tool-workpiece interface where much of the heat is transferred into the tool, accelerating tool-wear. Worn tools are undesirable because they result in low cutting efficiency and subsequently, worse part quality. To avoid negative effects such as this, cutting parameters must be optimized (i.e., the feed rate and cutting speeds, also known as 'feeds and speeds'). Companies are trying to increase productivity by machining faster, but the thermomechanical effects present in machining must be considered to maintain surface

integrity. In this context, the objective of the present work was to gain a comprehensive understanding the phenomenon of burr formation in machining, particularly the relationship between tool-wear and cutting parameters.

Burr formation is one of the undesirable byproducts that occur in machining processes. The International Organization for Standardization (ISO) 13715 defines burrs as the “*rough remainder of material outside the ideal geometrical shape of an external edge, residue of machining or of a forming process.*” Figure 1-1 shows examples of the kinds of burrs seen in industry across various machining processes. Burrs are problematic because of their negative impacts across the triple bottom line (TBL) of sustainable manufacturing: economic, environmental, societal impacts. For one, they are expensive to remove because they require post-finishing in the form of deburring, which is an entirely manual operation that requires skill [3]. Deburring is a non-productive operation that can account for up to 30% of manufacturing expenses in jet engine parts and up to 20% of manufacturing expenses in automotive parts [4]. Further, the copious amounts of burr material are typically discarded which adds to the already mounting waste generated from machining such as in coolant and chip disposal. Lastly, there are many societal implications, such as operator injury during assembly and the failure of parts in service because of leftover burrs that turned into stress concentrations [5]. Therefore, optimizing the machining process to minimize burrs will contribute greatly to achieving some of the tenants of sustainable machining: reduced costs, improved environmental friendliness, less waste, and better personnel health/safety [6, 7].

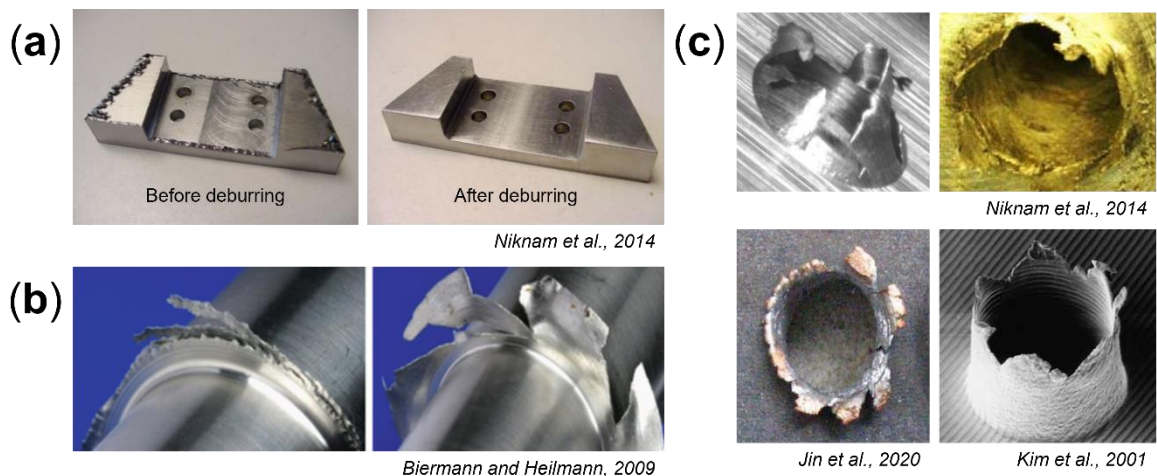


Figure 1-1. Burrs in (a) milling (reproduced from [8] under the CC license); (b) turning (reproduced from [9] with permission of Springer Nature, License Number 5440320873157); (c) drilling (reproduced from [5, 8, 10] under the CC license and with permission of Springer Nature and Elsevier, License Numbers 5440370956751 and 5440371134411).

Despite its ubiquitous occurrence in machining operations, burr formation has not been widely explored in literature, and much of the notable work is decades old. The “first wave” of burr formation studies occurred between 1965 and 1980 [11]; and there has only been marginal strides in research on the topic since. The literature that does exist focuses primarily on two specific machining processes: drilling and micro-machining. While both are important in industry, drilling is not finish machining process but rather a rough machining process, so surface integrity is not the primary concern. Micro-machining on the other hand, is a more niche process compared to its more conventional counterparts. Furthermore, very little work has sought to explore the other more widely used processes of turning and milling. Additionally, the materials explored in prior studies are typically more ductile metals like aluminum and stainless steel—very few works have addressed burr formation in Ni-alloys like Inconel 718, which are crucial to the aerospace industry and known for their excessive work hardening. Since research on burr formation is relatively sparse, efforts on modeling are lacking as well.

Given how problematic and expensive burr formation is in the manufacturing space, there is a demand for more research on the subject to further developments for optimizing machining processes by finding ways to reduce or eliminate it. While some burr formation is likely unavoidable, it can be substantially mitigated with process control—that is, the proper selection of parameters like feeds and speeds, depth of cut, and tool path, as well as physics-informed tool-life criteria. Optimizing machining processes through the suppression of burrs requires an understanding of “total machining performance”, which refers to the interacting nature between performance parameters such as tool-wear, chip segmentation, burr formation, etc. (see Figure 1-2). For example, cutting with worn tools will result in more friction at the tool-workpiece interfaces which alters the chip formation—changes in the chip formation affect the deformation in the primary shear zone, which then directly affects the state of stress in the cutting area. Furthermore, this study

sought to not only analyze the formation of burrs, but also consider how they are related to other machining aspects such as tool condition and microstructure state.

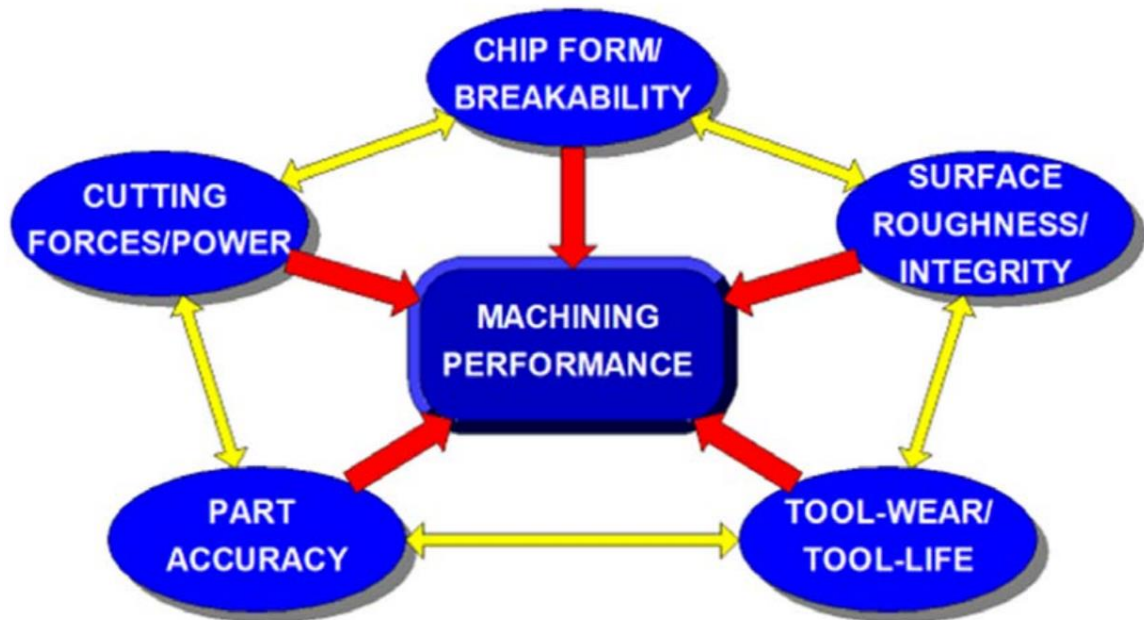


Figure 1-2. Framework of factors affecting total machining performance (reproduced from [6] with permission of ASME).

Thus, the objective of this study was to characterize burr formation in nickel-based superalloy Inconel 718 via a high-speed, high-resolution in-situ experimental method. Experiments were carried out to measure the variation in burr geometry with respect to varying factors like tool-wear condition, uncut chip thickness (i.e., the feed), and cutting speed. Results showed that all these factors have a significant effect on some aspects of burr formation, although certain burr metrics were found to be insensitive with respect to different process conditions. Using a physics-based model, the flow stress was calculated at the exit burr root, and it was found to be approximately equal to the flow stress. Finally, this study investigates the conditions for fracture during exit burr development—results show that negative exit burrs are a contingent upon high strain rate and high uncut chip thickness, which had been reported in prior work, but also dependent on the microstructural state, which has not been previously observed.

2.1 Machining of Nickel-Based Superalloys

Ni-alloys are notoriously difficult to cut due to their material properties. The focus of this work is on Inconel 718, a thermal resistant Ni-alloy used in gas turbines, rocket engines, and turbine blades [12]. Inconel 718 is typically composed of around 54% nickel (Ni), 22% iron (Fe), 17% chromium (Cr), 5% niobium (Nb), 1% titanium (Ti), and 0.5% aluminum (Al). These elements give it great oxidation and corrosion resistance, as well as fatigue and tensile strength at elevated temperatures [12-14]. Inconel 718 is also known for its easy weldability and crack resistance [12, 13]. It is, however, these very properties that result in poor machining performance for Inconel 718 and other Ni-alloys. Yin et al. [15] present a schematic illustrating the correlations between several Ni-alloy properties and their negative effects during machining in Figure 2-1.

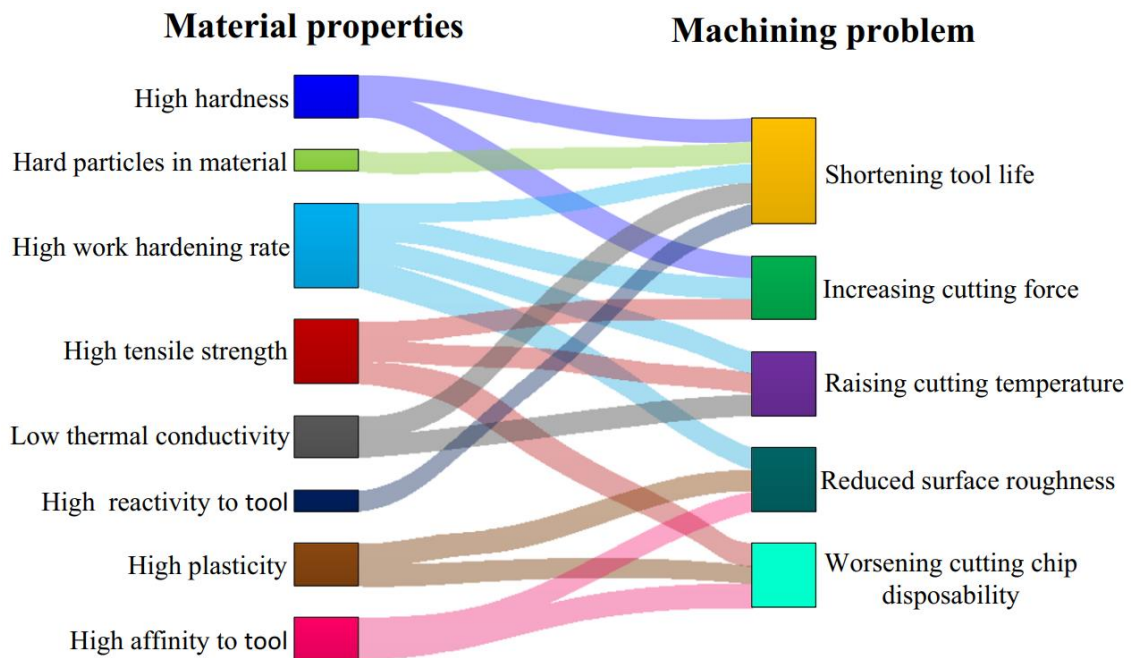


Figure 2-1. Correlation between material properties and machining defects (reproduced from [15] with permission of Springer Nature, License Number 5427931460106).

The standard metrics for measuring the ease of machining a certain material is the tool-wear or tool-life. The durable material properties of Ni-alloys like Inconel 718 from Figure 2-1 put an enormous amount of stress on the cutting tool, which results in rapid

tool-wear. The main tool-wear modes are flank-wear, notch-wear, and crater-wear. These forms of wear are caused by several different mechanisms: abrasion, adhesion, diffusion, and chemical affinity. Abrasion and adhesion are the most common mechanisms as they are present at both low and high temperatures, whereas diffusion and chemical wear arise at high temperature when the tool material reacts with the workpiece material [16]. Figure 2-2 presents some examples of these modes and mechanisms for tool-wear. Worn tools should be avoided because they typically generate a poor surface integrity, which is unacceptable for machined components (especially aerospace components), because the surface integrity drives the functional performance when the part goes into service. Machining with worn tools can cause surface defects like cracks and white layers, which have a detrimental impact on the fatigue life [17]. Worn tools also lead to tensile residual stress generation, which has a very negative effect on surface integrity for reasons such as enabling the propagation of stress corrosion cracks when the part is in contact with corrosive media [18]. Cracks are very undesirable because they act as stress concentrations—thus, tensile residual stress not only decreases the corrosion resistance, but also degrades the fatigue life. Poor surface integrity can be prevented by machining at slower feeds and speeds, but this also raises the manufacturing costs [17]. Thus, there is a balance to be struck between productivity and part quality to ensure economic stability.

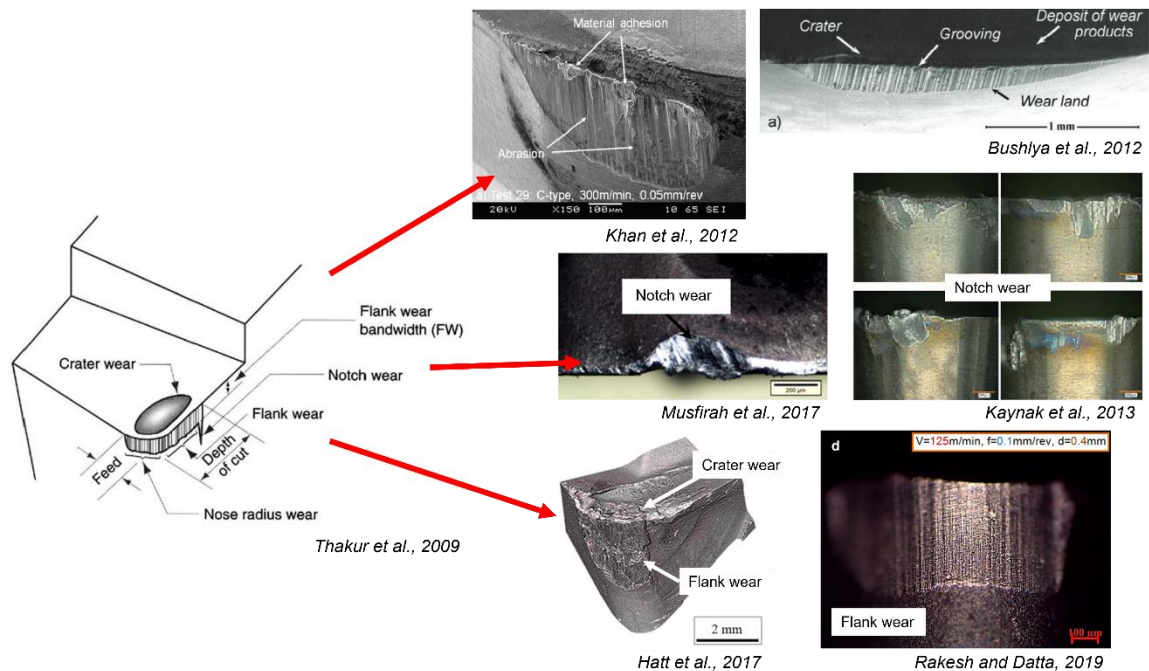


Figure 2-2. Tool-wear modes and mechanisms. Images reproduced from [19-25] with permission of Elsevier and Springer Nature, License Numbers 5440380404232, 5440381087265, 5440400334357, 5440381365393, 5440390090010, 5440390338603, 5440391308844.

Thus, to prevent rapid tool-wear and workpiece damage, machining hard-to-cut metals like Ni-alloys requires careful consideration of the process parameters. This is easier said than done, as the mechanics involved in machining are complex and require a thorough understanding of material behavior. With manufacturers looking to machine parts faster to scale up productivity, it falls on researchers to provide insight on the intricacies of the machining process to preserve surface integrity. This involves close analysis of the material behavior under the elevated machining regimes such as high feeds and speeds, variations in tool-wear, and different lubrication conditions. However, another issue is the lack of communication between industry, academia, and even governmental organizations regarding the optimization of machining processes for sustainability [6]. To achieve sustainable machining and furthermore, sustainable manufacturing, there must be collaboration between all these groups.

2.2 Effects of Cutting Conditions on Surface Integrity

Machining performance (sometimes generically referred to as ‘machinability’) is heavily driven by the selection of cutting tools, cooling/lubricating conditions, and perhaps most importantly, the cutting parameters. The latter include the cutting speed, feed rate (uncut chip thickness in orthogonal machining), and depth of cut. Cutting speed refers to how fast the workpiece (turning) or the tool (milling) are moving relative to one another. Feed rate refers to the amount by which the tool is fed into the workpiece with each cut/revolution, and depth of cut refers to how much material is taken off with each pass. Improper selection of any of these parameters can result in catastrophic damage to the workpiece and tool. The tool condition must also be maintained because excessive tool-wear or tool breakage can severely harm the machined part through chatter, burrs, and induction of tensile residual stress. Thus, many researchers have sought to understand the impact from these parameters to improve total machining performance.

Cutting forces, which are an indicator of the thermomechanical loading during the machining process, are well known to decrease with increasing cutting speed, and this was confirmed by many works [19, 24, 26, 27]. Cutting forces decrease with cutting speed because of the thermal softening effect, which creates less shear strength/resistance in the primary shear zone and subsequently reduces friction at the tool-chip interface [24, 27]. However, beyond a certain point, work hardening (the material's tendency to strengthen with prolonged plastic deformation, also referred to as strain hardening) will overcome the thermal softening effect and cutting forces will again start increasing with cutting speed [15]. This effect is depicted in Figure 2-3; it seems to occur between cutting speeds of 60-100 m/min, which is the upper regime for machining with tungsten carbide (WC) inserts.

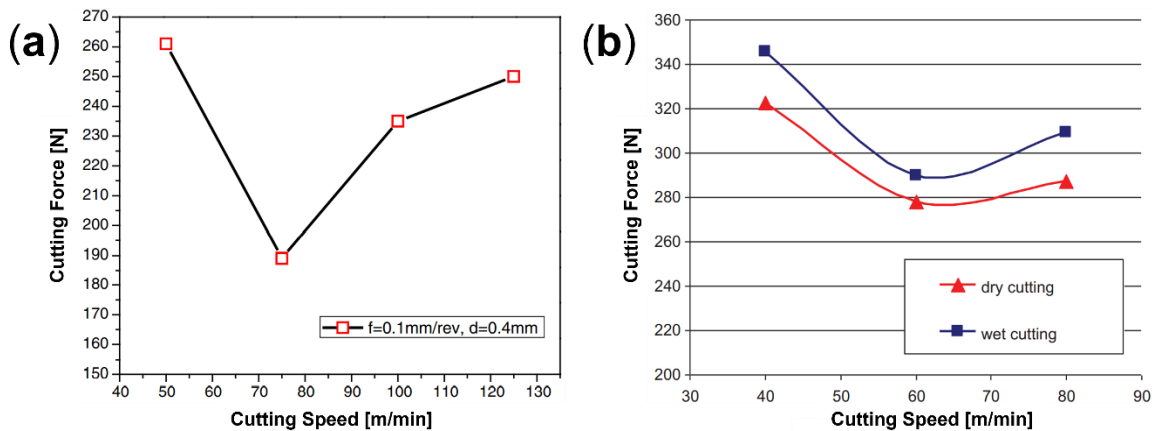


Figure 2-3. Cutting force variation with cutting speed for Inconel 718 (reproduced from [24, 28] with permission of Springer Nature and Elsevier, License Numbers 5427940633570 and 5427960339270).

Smaller cutting forces are good for prolonging tool life, as the mechanical loading on the tool is lower. However, increasing the cutting speed also raises the cutting temperature, which creates new problems. The temperature rises with increasing cutting speed for a number of reasons, such as more heat energy being generated from a higher strain rate in the shear zone [19]. The higher cutting speed also means there is less time for heat transfer, and with Ni-alloys such as Inconel 718 being relatively poor thermal conductors, this results in much of the heat being retained at the tool-workpiece interface [14, 24]. As abrasive wear rate is inversely proportional to the strength of the tool material, and hot hardness of cutting tool materials such as WC drops rapidly beyond 600 °C, higher cutting speeds will at some point result in a rapid increase in tool-wear rate. The increase

in temperature with cutting speed was observed by many authors [19, 26, 27, 29]. Thakur et al. [19] conducted dry turning experiments on Inconel 718 with WC inserts and noted a nearly linear increase in temperature with cutting speed that was consistent across multiple feed rates (see Figure 2-4).

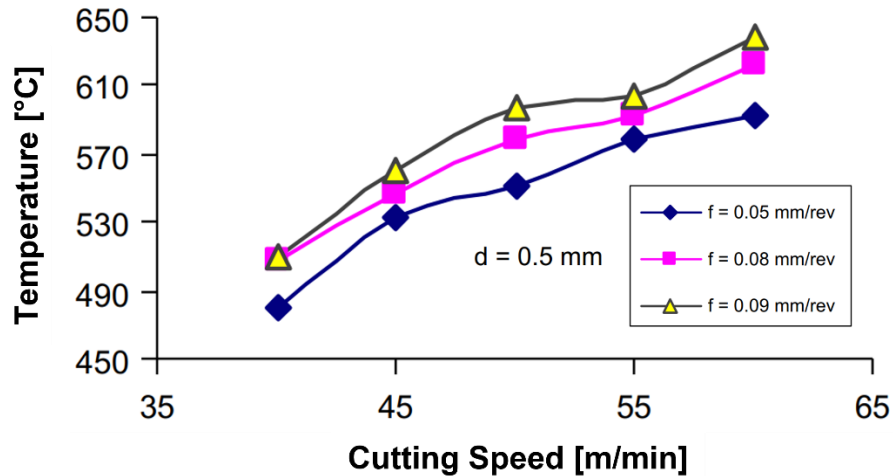


Figure. 2-4 Cutting temperature variation with cutting speed and feed rate (reproduced from [19] with permission of Elsevier, License Number 5427950598778).

Interestingly, Rakesh et al. [24] observed a rapid increase in temperature between the two cutting speeds of 50 to 100 m/min, but a slight decline when the speed was increased beyond that. They believe this was attributed to a deviation in tool geometry from massive tool-wear. High cutting temperatures are furthermore not desirable because of their implication on surface integrity of the workpiece. An increase in temperature at the cutting zone means a reduction in the shear strength of the material, making it more prone to plastic deformation, therefore increasing surface roughness and burr formation. Just as higher cutting temperatures weaken the workpiece material, it also softens the tool material, accelerating tool-wear [21].

While cutting forces tend to decrease with increasing cutting speed, the opposite is true for increasing feed rate. When feed rate is increased, the area of the uncut chip is increased accordingly, resulting in higher forces [30]. This increased mechanical loading will increase tool-wear because of greater stresses on the wedge of the cutting tool and higher cutting temperature, as was observed by Thakur et al. [19]. The effect of increasing cutting forces with feed rate was present in several works [30-32]. Thus, both cutting speed

and feed rate have significant influences on the thermomechanical effects present during machining. This section will discuss how both parameters affect the three main aspects of surface integrity: surface roughness, residual stress, and microstructure/microhardness.

2.2.1 Cutting Tool Condition

Tool selection and tool-wear management through optimal cutting parameters is paramount because of tooling's vital role in determining total machining performance, particularly workpiece quality aspects. For cutting such tough materials like Ni-alloys, tool materials are required to have good wear resistance and thermal shock properties, high strength and hot hardness, and chemical stability at elevated temperatures [33]. The standard tool material for machining Inconel 718 is cemented tungsten carbide (WC), which is chosen for its good balance of fracture toughness and thermal shock resistance [25].

WC inserts can come with chemical vapor deposition (CVD) or physical vapor deposition (PVD) coatings or be uncoated, although most modern tools now employ advanced coatings because of their substantial tool-life benefits due to the higher hardness and wear resistance [34]. Some of the most common CVD/PVD coatings are TiAlN, TiN, and CrN; TiAlN has been consistently proven to be the most effective coating because of its superior hot hardness and oxidation resistance [33]. While coatings can improve the durability of WC inserts, coated WC tools are still limited to relatively modest cutting speeds around 80 m/min [35], which is low compared to speeds routinely achieved in cutting aluminum and steel alloys.

For ultra-high-speed machining on the order of several hundreds of m/min, ceramic tools are the preferred option because of their superior hot hardness and chemical wear resistance which yields a longer tool life than WC [26]. Because of their propensity towards thermal shock, ceramic tools are often used without external cooling or lubricating media, which may result in catastrophic tool chipping and failure. While ceramic tools provide reasonable tool life at very high cutting speeds, they are generally avoided for finish machining because of their negative effect on surface integrity [36]. This is supported by Zhou et al. [37], who found that ceramic tools induced a deeper severe plastic deformation

(SPD) zone (to be discussed further in Section 2.2.4) and much higher tensile residual stress (to be discussed in Section 2.2.3) than PCBN tools. The latter finding is supported by Holmberg et al. [38], who also saw that ceramic tools induced a much higher tensile residual stress on the surface compared to WC inserts. Holmberg et al. [38] also observed that worn ceramic tools induced a lower tensile residual stress than the new tools, but at a greater depth. Although, they noted a lower surface roughness for the ceramic tools than the WC tools.

In addition to selecting the correct tool, it is also important to select the correct feeds and speeds. As stated earlier, increasing the cutting speed lowers the cutting forces. While this means a lower mechanical load on the tool, this increases the thermal load on the tool because of the increased heat generation and low thermal conductivity for many Ni-alloys [15]. Thus, increasing the cutting speed will still lead to more tool-wear because of thermal damage. Many different works noted tool-wear increasing with cutting speed [19, 24, 26, 39-41]. Figure 2-5 shows how the most common type of tool-wear, flank-wear, increases with cutting speed.

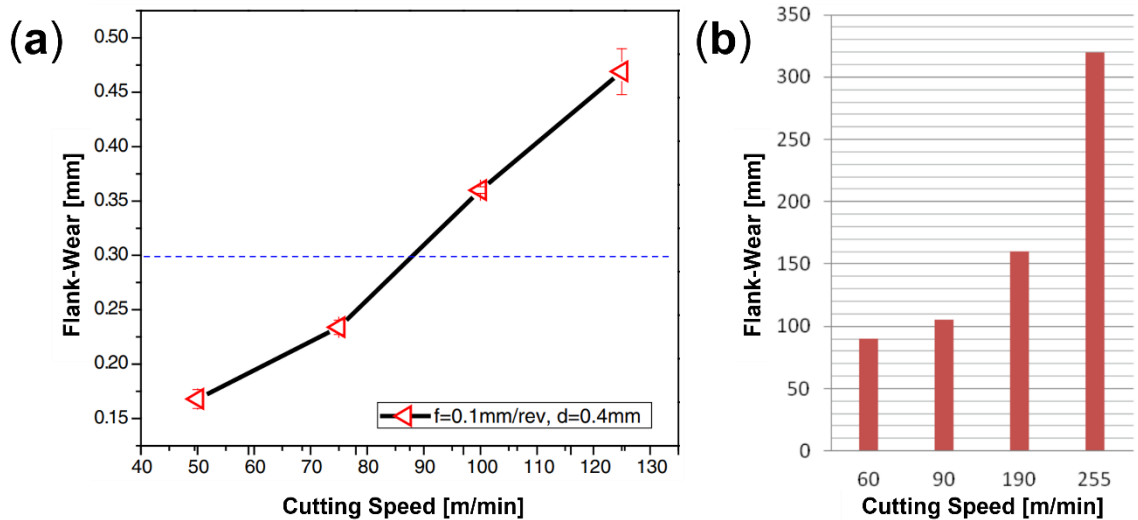


Figure 2-5. Change in flank-wear with cutting speed for Inconel 718 under (a) dry conditions (reproduced from [24] with permission of Springer Nature, License Number 5427940633570) and (b) wet conditions (reproduced from [39] under the CC-BY-NC-ND License).

Feed rate also has a detrimental impact on tool-wear. Unlike cutting speed, increasing the feed rate directly raises the cutting forces, putting more mechanical stress

on the tool. This was shown by Rahman et al. [42] in their wet turning experiments on Inconel 718 using coated WC inserts (see Figure 2-6a). Not only that, but there is more friction at the tool-workpiece interface, resulting in more heat generation, and therefore a higher cutting temperature [35]. This increased friction is not good for ceramic tools since they are prone to thermal wear, as was shown by Narutaki et al. [43]. As stated earlier, the cutting temperature should be suppressed to prevent heat from being transferred into the tool and accelerating its rate of wear.

However, it should be noted that the effect of increasing feed rate on tool-wear is minor because it mainly increases the mechanical loading and less so the thermal loading. Thus, the tool's strength will not deteriorate to the same degree as increasing the cutting speed, where the dominant thermal effects compromise the structural integrity of the tool. Still, the added mechanical loading from a higher feed rate does still have an impact on tool-wear development, as shown in Figure 2-6b. When analyzing tool-wear with respect to feed rate, data is usually normalized by using the cutting length (since a higher feed rate means a fixed distance will be traveled in less time). Li et al. [44] divided the cutting length by the feed rate to obtain the number of revolutions or "number of impacts in their milling experiments on Inconel 718 with coated WC inserts. Figure 2-6c shows their results for both up-milling and down-milling (the turning direction of milling cutters has a substantial impact on machining performance, including burr formation, to be discussed in Section 2.3.2). Furthermore, it is imperative to consider the effects of cutting parameters on tooling because worn tools can seriously compromise surface integrity, to be discussed in later sections.

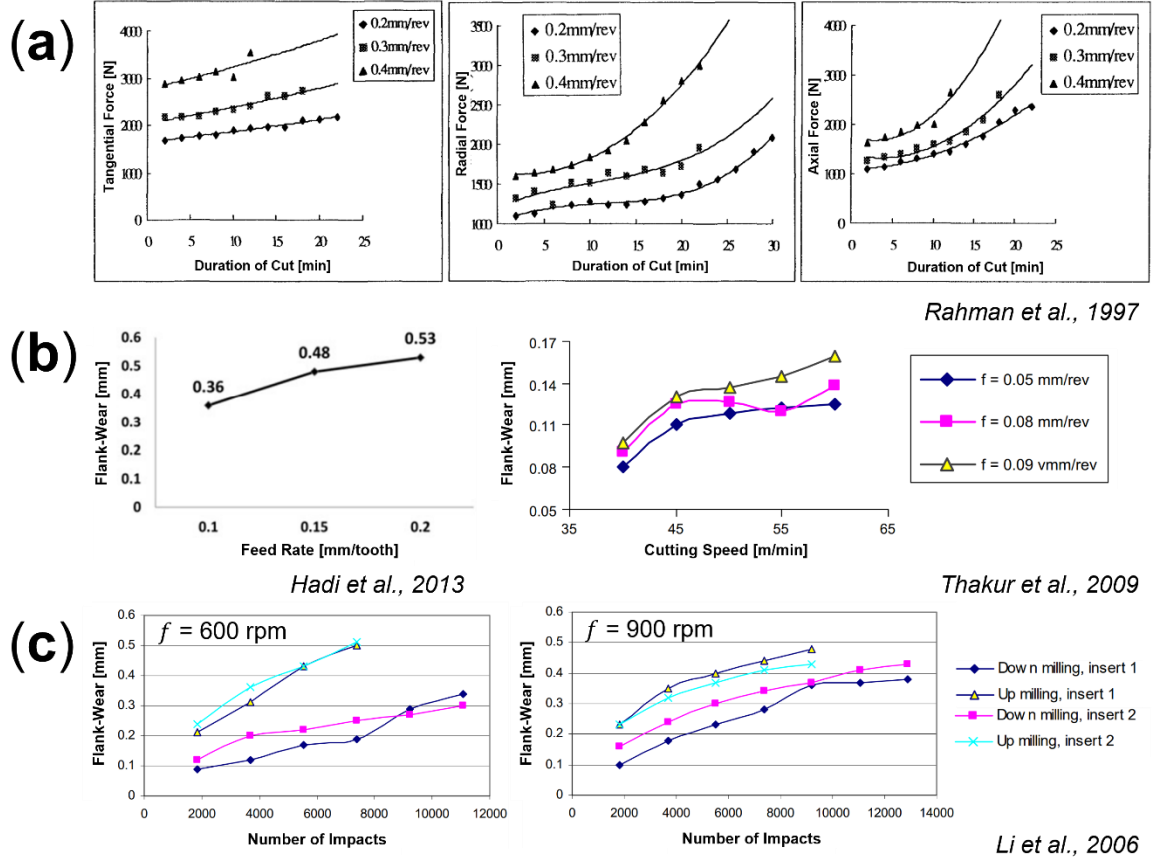


Figure 2-6. (a) Forces in relation to feed rate and duration of cut (reproduced from [42] with permission of Elsevier, License Number 5427961127336); (b) flank-wear in relation to feed rate (reproduced from [19, 45] with permission of Elsevier, License Numbers 5427960912537 and 5427950598778); (c) flank-wear with number of impacts/cutting length (reproduced from [44] with permission of Elsevier, License Number 5428000043935) for Inconel 718.

2.2.2 Surface Roughness

One of the metrics for measuring surface integrity is surface roughness. Surface roughness is defined simply as the average of the peaks and valleys of a machined part's surface finish, quantified by the value, R_a ; higher R_a values denote a higher surface roughness (i.e., worse surface finish). Thus, surface roughness should be minimized to meet the tight fitting tolerances associated with machined jet engine parts. A high surface roughness also means a higher friction coefficient, which contributes to a higher wear rate for the component. On the contrary, a low surface roughness improves part reliability by providing better fatigue strength, corrosion resistance, and wear resistance [46, 47]. Like

all surface integrity characteristics, surface roughness is controlled by the tool condition and cutting parameters.

One of the reasons tool-wear needs to be mitigated is because of its implications on surface roughness [15]. Multiple studies have shown that worn tools lead to higher surface roughness [24, 48, 49]. Rakesh and Datta [24] conducted dry turning experiments on Inconel 718 with uncoated WC inserts and noticed a nearly linear trend of surface roughness increasing with tool-wear, as shown in Figure 2-7. Nalbant et al. [48] compared the surface roughness obtained with different WC coatings in dry turning of Inconel 718—not only did the coatings have a major effect on surface roughness, but surface roughness steadily increased as the machining time progressed. These findings indicate that as the tool wears, the surface roughness deteriorates.

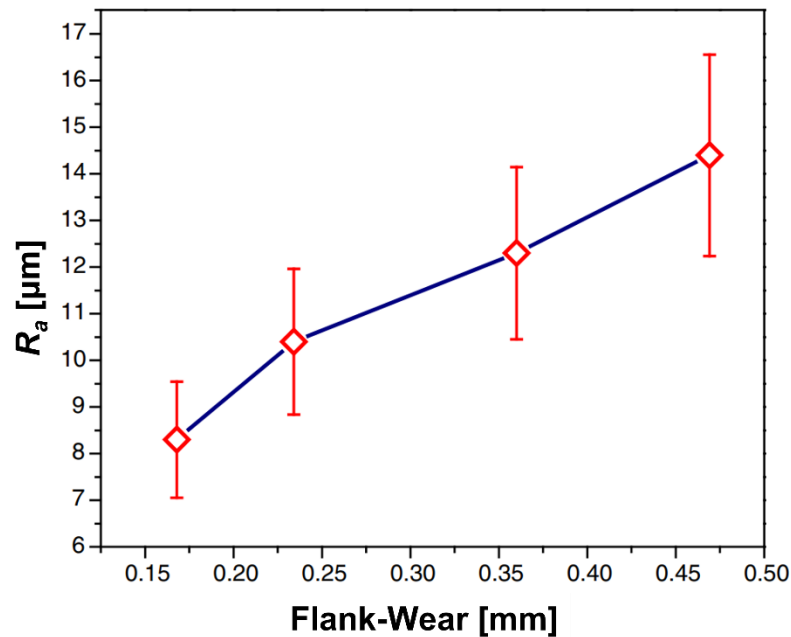


Figure 2-7. Surface roughness variation with tool-wear (reproduced from [24] with permission of Springer Nature, License Number 5427940633570).

While tool-wear is generally undesirable for controlling surface roughness, it has been reported by multiple studies that new/sharp tools may not be ideal either. In fact, it has been shown that moderate levels of wear can produce a better surface finish than new tools. Sharman et al. [41] performed dry turning experiments with coated and uncoated WC inserts and found that the worn coated tools produced a substantially lower surface roughness than new tools, especially at higher feed rate. Interestingly, this was not the case

with uncoated tools, where wear only worsened the surface roughness (although only one cutting speed was tested whereas three cutting speeds were tested for the coated tools).

Cutting parameters also play an important role in surface roughness. Most studies report that surface roughness decreases with increasing cutting speed [14, 19, 39, 50-52]. This is due to the thermal softening effect, which is attributed to the higher cutting temperature obtained when raising the cutting speed. Thermal softening lowers the yield and tensile strengths of the workpiece, which makes the material easier to deform [15]. However, some authors [39, 53, 54] noticed that as the cutting speed increased, the surface roughness decreased but began rising after a certain point, as shown in Figure 2-8. This can also be seen in the work by Thakur et al. [19], where the surface roughness ‘bottoms out’ after a speed of 55 m/min. It is likely that it would begin to rise if data was collected beyond this point. This behavior is due to work hardening overcoming the thermal softening effect, which is the second stage as explained by Yin et al. [15]. The initial decrease is because of thermal softening (as expected), but the increase is likely due tool-wear developing [35, 39]. Lu et al. [49] explain this behavior in a similar context, that being increased cutting time rather than increased cutting speed. New tools begin cutting with a higher surface roughness and overtime a mildly worn tool will yield a lower surface roughness because of decreased residue on the machined surface. However, tool-wear will eventually cross a threshold to where the residue left will be higher, and at this point surface roughness begins to increase with tool-wear. This phenomenon was previously discussed as being observed by Sharman et al. [41].

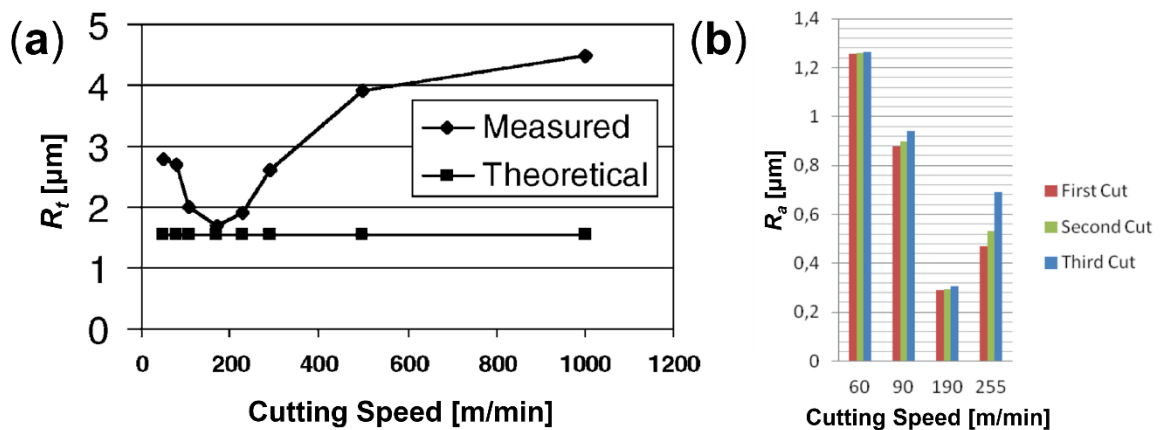


Figure 2-8. Surface roughness variation with cutting speed for (a) bainite steel (reproduced from [54] with permission of Elsevier, License Number 5427961284848) and (b) Inconel 718 (reproduced from [39] under the CC-BY-NC-ND License).

The biggest influencing factor on surface roughness, however, is feed rate [15, 55]. Surface roughness always increases with feed rate because of kinematic effects (increased ‘scallops’ left by each revolution of the tool) and increased mechanical loading. This is indicated by the higher cutting forces, which stress the tool and induce wear. When the tool becomes worn, it begins to tear material rather than cut, resulting in a poor surface finish [56]; this was confirmed by several studies [41, 49, 57]. Increasing the feed rate causes ‘feed marks’ to form, which contributes to a higher surface roughness [32, 41]. Wang et al. [53] saw an increase in surface roughness with increasing feed rate in their dry face milling experiments on Inconel 718 using coated WC inserts. Bai et al. [32] illustrated the rise in surface roughness with feed rate in their turning experiments on Inconel 625 and Inconel 718 using coated WC inserts. They compared conventional turning (CT) to ultrasonic assisted turning (UAT) and found that the latter produced a significantly better surface finish than the former for both materials, as shown in Figure 2-9; UAT is one of the many novel machining technologies that can have a major influence on surface integrity. Another noteworthy technology is cryogenic machining, which has been shown to vastly increase tool life because of its cooling efficiency (effectively preventing thermal softening) when combined with minimum quantity lubrication (MQL) [58, 59]. The enhanced tool-life has been shown to yield remarkably lower surface roughness [60].

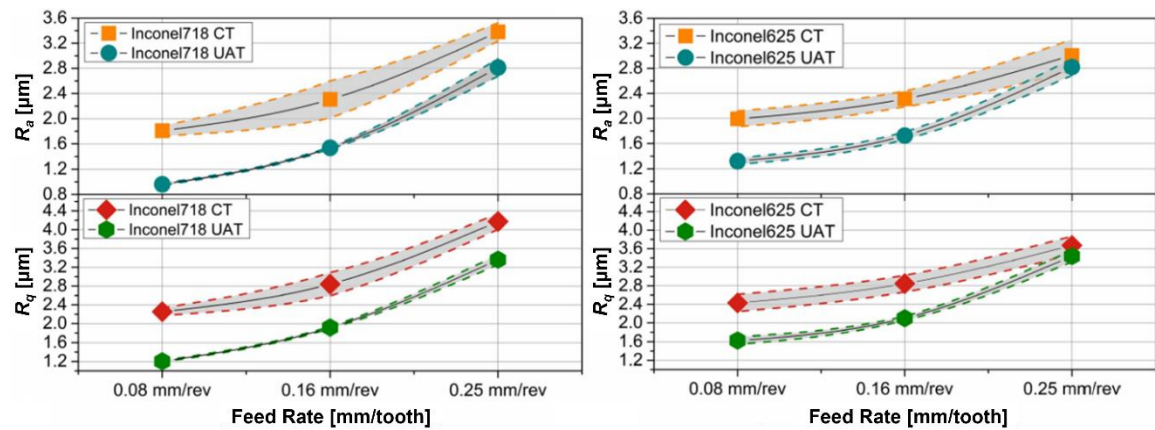


Figure 2-9. Effect of feed rate on surface roughness in CT and UAT for Inconel 718 and Inconel 625 (reproduced from [32] under the CC-BY License).

2.2.3 Machining-Induced Residual Stress

Machining-induced residual stress (RS) is an imperative surface integrity factor that has been shown to have major influence on fatigue life, a very crucial characteristic for the quality and performance of machined superalloy parts. RS is the stress that remains in the workpiece even after the machining operation is complete. RS impacts fatigue life by either decreasing it via tensile ‘pre-load’ towards crack propagation, or increasing fatigue life through compressive RS, which serves to suppress crack initiation and growth [15]. Inconel 718 for instance, is more susceptible to dimensional instability than Ti-6Al-4V or mild steel [61]. RS can be categorized as tensile or compressive. Generally speaking, tensile RS is the byproduct of thermally-dominant machining, and compressive RS is the byproduct of mechanically-dominant machining [33, 62]. At low cutting speeds where the cutting temperature is low, the deformation is mainly mechanical, resulting in more compressive subsurface RS. At higher cutting speeds where the heat generation is much higher, the formation of tensile RS is much more prevalent. Fatigue life is important for superalloy parts because they are undergo cyclical loads in service; tensile RS degrades fatigue life because it decreases the allowed alternating stress whereas compressive RS improves fatigue life because it increases the allowed alternating stress [33]. Thus, the former should be avoided, but the latter is desirable. RS is most tensile at the surface and becomes more compressive deeper in the subsurface. Typical RS profiles exhibiting the ‘hook’ shape that occurs due to combined thermomechanical loading (thermal loads dominating near the surface, mechanical load dominating in deeper subsurface layers) are shown in Figure 2-10.

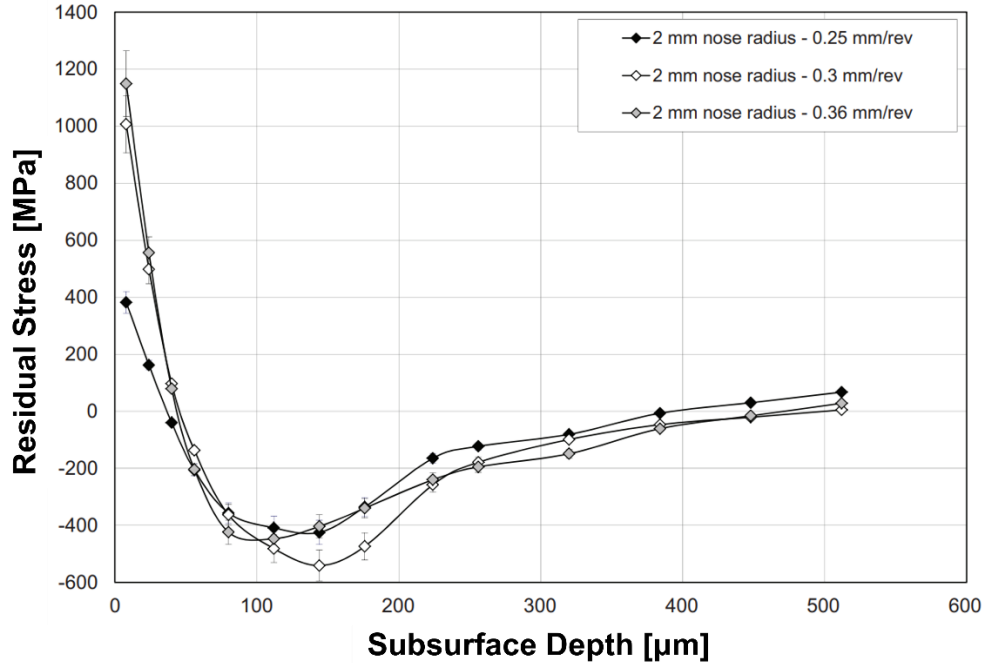


Figure 2-10. RS profile at various feed rates for Inconel 718 (reproduced from [31] with permission of Elsevier, License Number 5427970504660).

Along with cutting speed, tool-wear is one of the biggest attributors to tensile RS formation, as was proven by many researchers [31, 38, 63]. Sharman et al. [63] compared coated and uncoated WC inserts in dry turning and found that tool-wear had the biggest influence on the RS profile. In all cases, surface tensile RS increased dramatically with tool-wear—this is caused by the heightened temperatures due to the friction from ploughing/rubbing from the tool flank-wear. However, this also comes with a benefit, as the deeper plastic deformation from the rubbing/ploughing allows for deeper penetration of compressive RS beneath the thermally affected surface layer that is also larger in magnitude. In a later study, Sharman et al. [31] observed the same effect in the wet turning of Inconel 718 using coated WC inserts. Owing again to the importance of tool material selection (WC versus ceramic), Holmberg et al. [38] discovered that ceramic tools induced higher tensile RS than WC tools in wet milling. Another important aspect relating to the effect of tooling on RS is the rake angle. Studies have corroborated that a negative rake angle is preferable because it generates a more compressive RS, whereas a positive rake angle generates a more tensile RS [36, 62, 64].

In terms of feeds and speeds, both have been shown to increase tensile RS. It has been identified that tensile RS increases with increasing cutting speed [52, 54, 65]. Sadat

[52] found that the magnitude of both the tensile and compressive RS increased considerably with cutting speed, however the depth of the surface tensile RS decreased in dry turning with WC inserts. Wang et al. [66] noticed a very interesting effect regarding the correlation between RS and cutting speed: the RS first decreases (i.e., becomes more compressive) as cutting speed increases from 40 to 60 m/min, but then increases drastically (i.e., becomes more tensile) when going from 60 to 80 m/min in the ball end milling of Inconel 718 under wet conditions. They attribute this to the decrease in thermal loading at the cutting zone because of increased chip flow rate. A higher chip flow rate means more heat is transferred out of the cutting zone because it is carried away with the chip—this effect is elaborated upon by Pawade et al. [62]. However, between 60 and 80 m/min, the thermal load remains trapped in the cutting zone, which is what leads to the rapid increase in tensile RS [66]. This is likely due to the heat generated in the cutting zone exceeding the capability of heat dissipation through the chip. Interestingly, this effect of increasing cutting speed first improving surface integrity then hurting it at a higher regime was previously shown to be true for surface roughness as well (see Figure 2-8). Furthermore, each tool seems to have a critical cutting speed above which the thermal effects exceed its limits and result in poor surface integrity (i.e., higher surface roughness or tensile RS) [40, 67].

While cutting speed is the most dominant variable in milling processes, in turning processes, feed rate often has a more pronounced effect on RS than cutting speed. This difference may be explained by the different thermomechanical loads imposed by each of these processes, primarily the large degree of ‘chip thinning’ in milling processes (relatively large tool radius vs. small feed), as opposed to the relatively large uncut chip thickness values encountered in turning processes (relatively small corner radius vs. large feed). Based on literature, the rise in tensile RS in turning is larger when feed rate increases compared to when cutting speed increases [31, 62, 63, 68]. Sharman et al. [31] found that increasing the feed rate produced higher values of tensile RS and a deeper tensile layer. They explain that a higher feed rate creates larger and deeper tensile RS because of the increased forces and heat generation, which concurs with other works [19, 30-32, 35]. This was shown in Figure 2-10. Wang et al. [53] attained the same result, seeing a moderate increase in surface tensile RS. They also noted that the RS component parallel to the feed

of the tool was always higher than the component vertical to the feed. Although what makes their work unique, is that they conducted three point bending fatigue life experiments to calculate the fatigue life per feed rate: Figure 2-11 shows how the feed rate has a significant effect on decreasing the fatigue life. This is a remarkable finding, as very few works perform fatigue life testing in addition to the RS measurements.

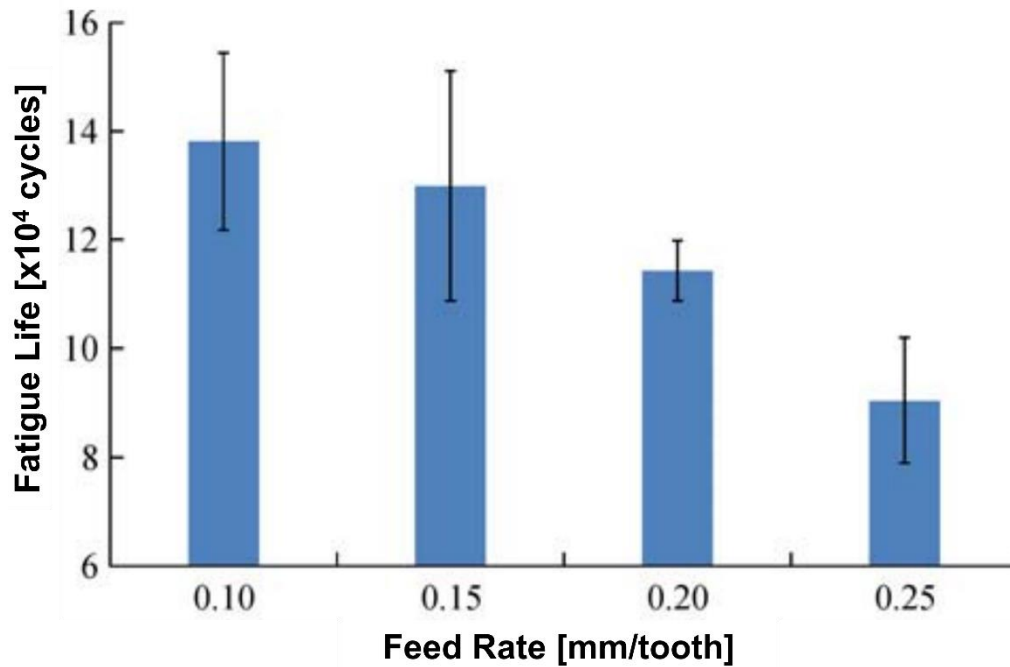


Figure 2-11. Fatigue life variation with feed rate for face milling of Inconel 718 (reproduced from [53] with permission of Springer Nature, License Number 5427970703568).

2.2.4 Microhardness and Microstructure

The microstructure of a material refers to its grain structure (i.e., how the material is composed on a fine scale). Different materials have different types of grains that vary in size, orientation, and phase. The prefix of “micro” comes from the fact that the grains are on the scale of micrometers in size [69]. Since the grains are so small, they can only be characterized with special microscopy techniques such as scanning electron microscopy (SEM) or electron back scatter diffraction (EBSD). Microhardness refers to the hardness of the grains composing the microstructure and is measured with methods like the Vickers or Knoop indenter tests. Figure 2-13 shows a typical microhardness profile.

Both chemistry and microstructure are determining factors of a material's properties; the chemistry is set early in the process (when the material is still in liquid form), but the microstructure can be altered after the material has solidified through heat and pressure. For instance, alloys are usually heat treated to obtain γ' and γ'' phase precipitates because of their effect on thermal stability [15]. Therefore, it is of great importance to pay attention to a material's microstructural state as it undergoes processing where it can experience significant changes. Machining, however, is an operation that is typically intended to attain a certain surface quality, while not altering the workpiece's microstructure. However, the microstructure in a shallow near-surface layer will often change due to the intense thermomechanical loads in machining processes. For example, severe grain deformation may lead to dynamic recrystallization, which is where the grains become more refined, thereby increasing the microhardness according to the well-known Hall-Petch effect [70].

Grain refinement at the surface may lead to the formation of a “nanocrystalline layer”, which is comprised of very fine grains typically less than 200 nm in diameter. Speaking to the importance of the lubrication and techniques, a recent study by Toker et al. [71] showed that cryogenic turning results in a considerably larger nanocrystalline layer at high cutting speed than similar conditions under flood cooling, suggesting that faster feeds and speeds can be used in cryogenic machining compared to conventional alternative cooling methods. Nanocrystalline layers are beneficial because they increase the microhardness of the surface, although a recent review by la Monaca et al. [18] showed that too much grain deformation or surface layer hardening will result in excessive brittleness, which lowers wear performance and fatigue life. Yin et al. [15] explain the three deformation zones observed by Zhou et al. [72] and Imran et al. [73], shown in Figure 2-12. Zone 1 is the uppermost part of the subsurface and is known as the SPD zone, or white layer. It is very negative for fatigue life and should therefore be minimized as much as possible [15, 74]. Zone 2 is a partial deformation layer where the grains and grain boundaries have elongated, and Zone 3 is unaffected [15].

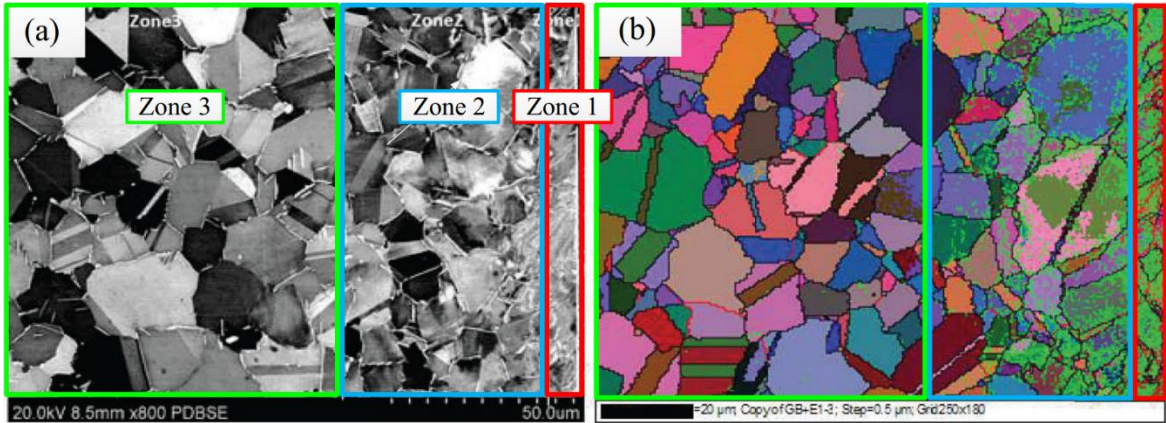


Figure 2-12. The three grain deformation zones (reproduced from [15] with permission of Springer Nature, License Number 5427971400371, originally modified from [72] with permission of Elsevier, License Number 5427971266957).

Like with the other surface integrity aspects, tooling has a major effect on microstructure development as well. Various studies observed that worn tools cause higher subsurface microstructural deformation than new tools [31, 41, 63, 72]. Sharman et al. [31] found that tool-wear had the greatest impact on microstructural alteration: higher tool-wear resulted in considerably deeper deformation layers that contained deformed grains, cracked carbides, and surface cavities. Since microstructural deformation means a higher microhardness, it would be reasonable to assume that surfaces machined with worn tools would have a higher microhardness as well. This was observed by Sharman et al. [41], who found that new tools produced a smaller increase in microhardness than worn tools. However, it should be noted that literature analyzing the effects of tool-wear on microstructure is limited.

Cutting parameters have also been proven to alter the microstructure. Studies have shown that higher cutting speed has a subtle if not negligible effect on subsurface deformation [50, 74-76]. In their dry milling experiments with coated WC inserts on Inconel 718, Cai et al. [75] saw no major difference in microstructure at 50 m/min, however they noted deformed grain boundaries at 80 m/min and 110 m/min—the deformation depth between 80 m/min and 110 m/min was similar, however. Even though the increase in subsurface alteration between these two speeds was negligible, there was a notable increase in the microhardness. Jin and Liu [74] also saw this trend in their high-speed milling experiments on Ni-alloy FGH95, as shown in Figure 2-13. Given the durability of Ni-alloys,

small changes in the cutting parameters will have little effect on the workpiece [41]. This theory is supported by Jin et al. [50], who conducted dry milling experiments on Ni-alloy FGH95 using WC inserts in the cutting regime of 20-600 m/min. They did not see a significant increase in subsurface deformation depth until 300 m/min, which is well beyond the maximum cutting speed employed by Cai et al. [75]. Interestingly, however, they observed a gradual decrease in white layer thickness with increasing cutting speed. They explain that this is because heat has less time to diffuse into the subsurface as cutting speed increases, resulting in a thinner white layer. Jin and Liu [74] continued studying this effect in a similar study with the same conditions but at much higher speeds (800-4000 m/min). They found that white layer thickness was essentially constant across the entire cutting speed regime, except for a slight increase at 2400 m/min. This also correlated to a drop in microhardness at that speed, after which it began rising again (see Figure 2-13). This is a crucial development, because it alludes to an inverse relationship between the white layer and microhardness.

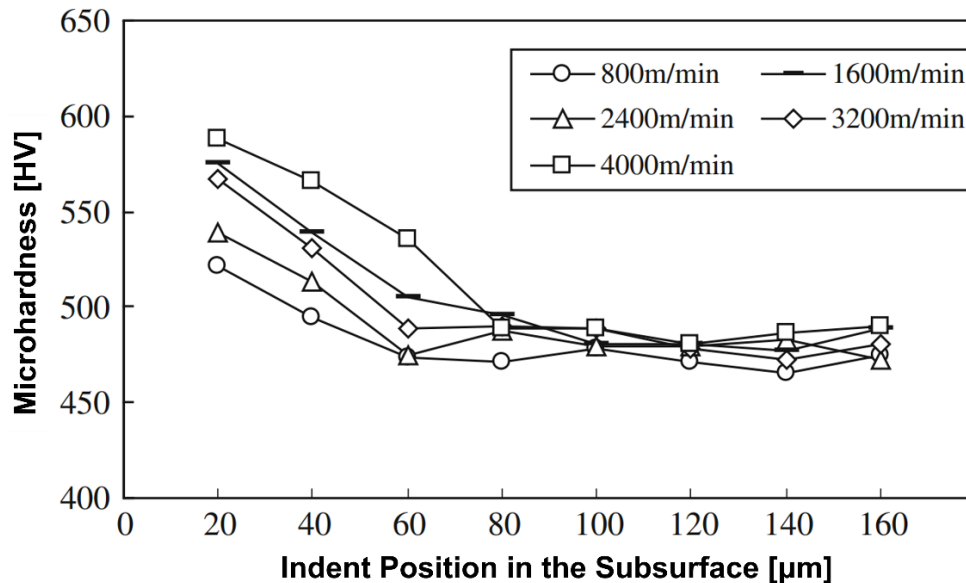


Figure 2-13. Change in microhardness with varying cutting speed for Ni-alloy FGH95 (reproduced from [74] with permission of Springer Nature, License Number 5427980085840).

While it appears that cutting speed is not a substantial factor on microstructure, the opposite is true for feed rate. Sharman et al. [41] compared new and worn WC inserts in the turning of Inconel 718, and found that for every tool and cutting speed, increasing the feed

rate produced a much deeper microstructural depth (see Figure 2-14). They also found that microhardness increased with feed rate in all cases. A higher feed rate means larger cutting forces, which induce more and deeper plastic deformation because of the increased mechanical loading in the subsurface.

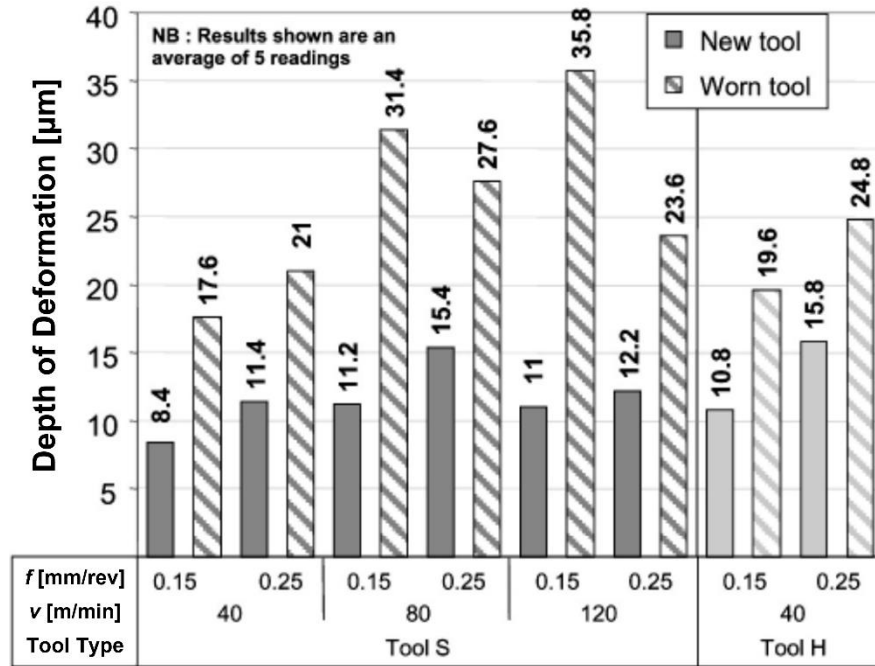


Figure 2-14. Variation in deformation depth with respect to various parameters for Inconel 718 (reproduced from [41] with permission of Taylor & Francis).

Ji et al. [76] analyzed the microstructure of Inconel 718 in selective laser melted and wrought form during dry micro-milling with coated WC inserts. For both workpieces, increasing the feed rate increased the microhardness. Further cementing the point of cutting speed not having a major effect, the authors observed virtually no change in microhardness for both cases when increasing the cutting speed. Although it is important to point out that the increase in microhardness with feed rate was noticeably larger when the cutting speed was higher. Thus, it can be inferred that a higher feed rate in combination with a higher cutting speed results in more microstructural deformation.

2.3 Burr Formation

Burr formation is a special subset of surface integrity that is not viewed in the same light as the other categories like surface roughness, RS, or microstructure. Burrs can be defined as material that plastically deforms at a part's corners or edges because of plastic flow during machining—this usually occurs at the entrance and exits of the cutting tool on the workpiece [5]. Burrs do not necessarily affect the mechanical properties of machined parts like other surface integrity characteristics do, but that does not mean they do not pose a serious issue for part quality. Jin et al. [5] provide an extensive list of all the potential problems resulting from burrs, which include creating stress concentrations (which harms fatigue life), poor dimensional accuracy, and issues during assembly like operator injury.

Thus, burrs need to be removed before a part can go into service, and this is done through deburring. However, deburring is not only unproductive and costly, but it can ruin dimensional tolerances because the process is manual and subject to human error since it is difficult to automate [5]. While deburring will always be required to some extent, it should be avoided as much as possible because it adds no value [77]. Edge finishing operations like deburring are usually neglected during the design stage, which causes them to be unsustainable because there was no planning beforehand. Selecting the appropriate deburring tools and processes requires knowledge of burr formation, namely size and location [78]. The cost of burr treatment is enormous—at one point the manufacturing sector was spending \$5 billion annually on burr removal [79].

Furthermore, understanding the formation of burrs to minimize them will have many economic benefits for the manufacturer [4]. Unfortunately, however, literature review showed that the landscape of burr formation research is still in its infancy. Most of the foundational, novel work was conducted decades ago, and recent studies focus almost exclusively on drilling and micromachining. Very few works have investigated burr formation in the conventional processes of turning and milling and even fewer address burr formation in superalloys—most of the work found involved more common materials like steel and aluminum. This section provides an overview of the work that has been conducted on burr formation.

2.3.1 Types of Burrs and Formation Mechanism

Gillespie [79] performed what is perhaps the first work focusing on burr formation in machining and would go on to be referenced often by future scholars investigating the phenomenon. He provided a thorough analysis of burr formation across turning, milling, drilling, and grinding. Through this, he became the first to lay out an interpretation for the burr formation mechanism. According to Gillespie [79], there are three different types of burr mechanisms: lateral extrusion of workpiece material, bending of the chip over the edge, and tearing of the chip from the workpiece. However, Gillespie [79] is most known for pioneering the classification of burrs, for which there is still no universal standard since companies typically have their own convention for naming burrs [5].

Gillespie [79] categorized four types of burrs: Poisson burrs, roll-over burrs, cutoff burrs, and tear burrs. Poisson burrs are due to lateral extrusion, which occurs when high localized pressures at the tool cutting-edge cause compressive plastic deformation and material bulges at the sides of the tool where it is pushed over the edge [79, 80]. However, it is well known that the Poisson effect refers to out-of-plane elastic deformation, despite side burrs being a form of plastic deformation. Nevertheless, roll-over burrs are caused by the bending of the chip at the workpiece exit, where material is ‘pushed out’ of the tool’s path and over the edge, leaving behind a ‘positive’ exit burr [79, 81]. Cutoff burrs are when material separates from the workpiece before the cut is complete, leaving behind a ‘negative’ exit burr [15]. Finally, tear burrs are as the name implies: material is ‘torn off’ rather than complete shearing [5, 79]. Poisson, roll-over, and cutoff (fracture) burrs are the most prevalent and have received the most attention in literature; they are also the focus of this work. Roll-over and cutoff burrs are similar in that they both form at the exits of a workpiece. Moreover, later authors would adopt a more simplistic nomenclature for Poisson and roll-over/cutoff burrs based on their location along the workpiece, that being side and exit burrs, respectively. The present work also uses this terminology.

Research on the exit burr formation mechanism would be continued by later researchers, namely Ko and Dornfeld [82], who built upon the work by Gillespie [79] by identifying three key stages for the formation of exit burrs: initiation, development, and final formation. These stages are visualized in Figure 2-15, which comprises of frames of

ultra-high-speed video captured on the custom-built in-situ testbed. Figures 2-15a and 2-15b are during the cut itself (loaded condition), representing initiation and development, respectively. Figure 2-15c was taken after the cut with the tool passing over the workpiece where there was no contact (unloaded condition), representing final burr formation.

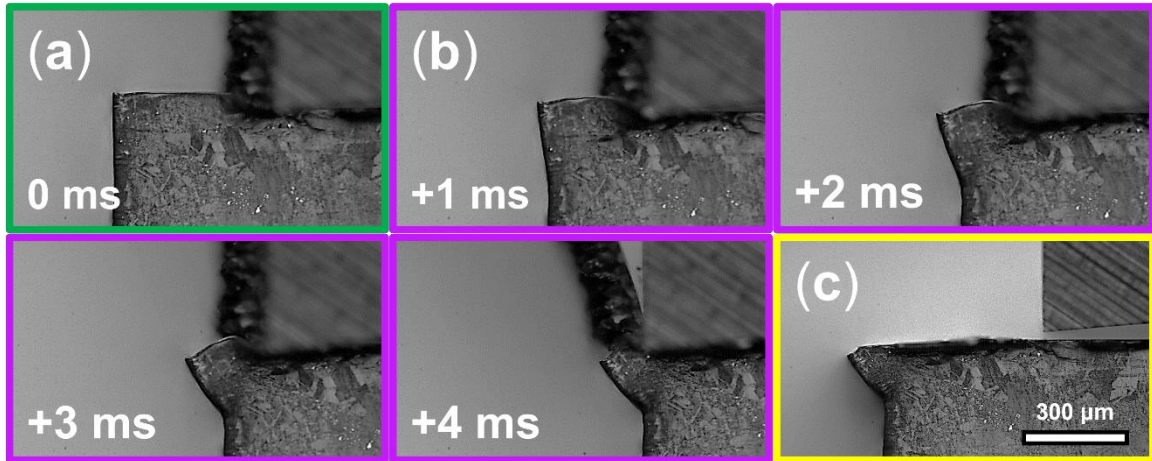


Figure 2-15. High-speed in-situ images of positive exit burr (a) initiation; (b) development; (c) final formation (after cut) at $VB = 0 \mu\text{m}$, $h = 80 \mu\text{m}$, $v_c = 6 \text{ m/min}$.

Initiation starts at a transition point as the tool approaches an exit of the workpiece where the energy for steady state chip formation is transformed completely into energy for burr formation and is indicated by the appearance of a negative shear plane first introduced by Pekelharing [83] (not to be confused with the primary shear plane in chip formation) [81, 82, 84, 85]. The initial negative shear plane (negative shear plane at initiation) is correspondingly represented by an initial negative shear angle (β_0) that runs from the tool tip to a plastic hinge, known as the burr root, where the burr pivots about during development—this burr root was identified by numerous authors [79, 82, 86]. An illustration of this process is shown in Figure 2-16. Once the tool passes over the edge, the exit burr left behind can either be ‘positive’ or ‘negative’. As described earlier, a positive burr is when the material extruded over the edge remains attached to the workpiece, forming a sharp point (this type is shown in Figure 2-15c). Furthermore, besides β_0 , Ko and Dornfeld [82] presented a number of metrics for measuring positive exit burrs first introduced by Schäfer [87]. These metrics are summarized in Table 2-1 and can be visualized in Figure 4-1 but will also be discussed in greater detail in Section 4.1.

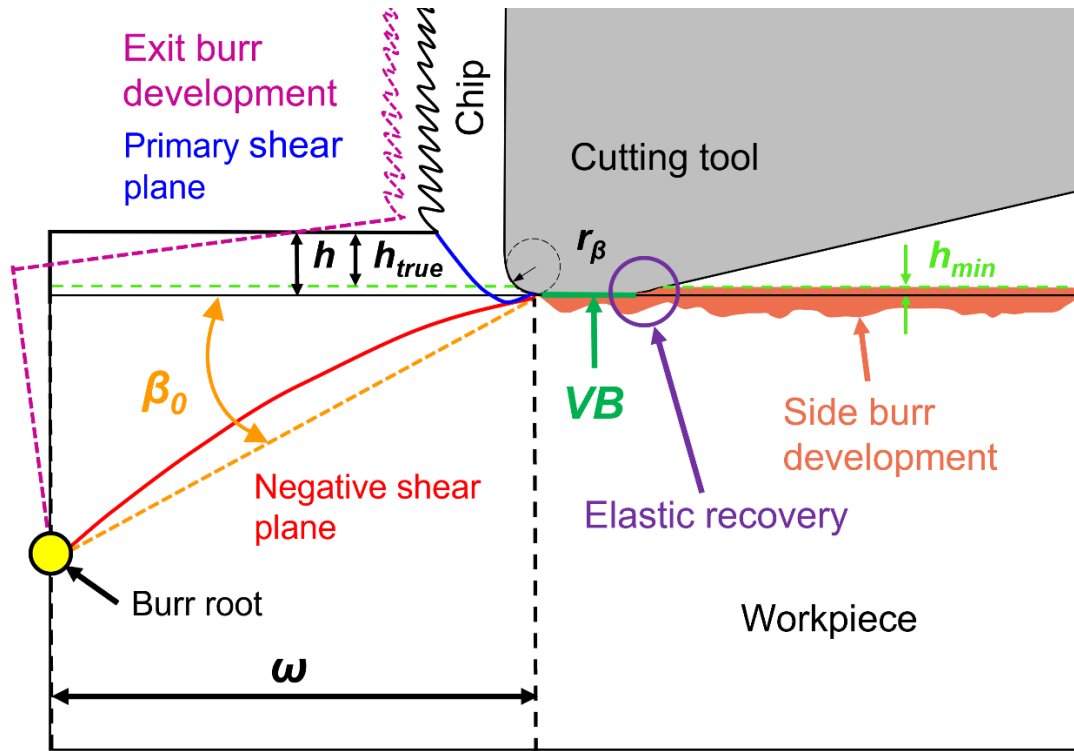


Figure 2-16. Schematic of exit burr development [82].

Table 2-1. Positive Exit Burr Metrics Proposed by Ko and Dornfeld [82].

| Metric Symbol | Definition |
|---------------|------------------------------|
| b_t | Exit burr thickness |
| b_h | Exit burr height |
| ψ | Inclination angle |
| ω | Initiation distance |
| β_0 | Initial negative shear angle |

Negative exit burrs form whenever the burr is sheared off the workpiece along with the chip, forming a chip in the shape of a ‘shoe’ or ‘foot’ [81]; the material that was fractured off leaves behind a ‘breakout’ on the workpiece. Figure 2-17 shows ultra-high-speed frames of a negative burr forming. As established previously, exit formation consists of bending of the chip and shearing in the negative shear plane. Thus, exit burr fracture is caused by plastic bending and shear deformation [81, 85]. Compared to positive burrs, negative burrs are relatively rare, as they only seem to occur under certain circumstances. Many authors have proposed different theories, such as Hashimura et al. [88], who state that it has to do with the ductility of the material—it is true that the mode of fracture behavior can either be brittle

or ductile depending on the material ductility [89, 90]. Ko and Dornfeld [85] demonstrated that negative burrs are dependent on the fracture strain of the material—in their study, it was difficult to obtain fracture in ductile materials (pure copper and aluminum) but easier in the case of more brittle materials (Al 6061-T6 and Al 2024-T4). Furthermore, material ductility has been explored to some extent by other authors, who found that ductile materials generated larger positive burrs compared to brittle materials [11, 91, 92]. However, the present work showed that positive and negative burrs are not exclusive to ductile and brittle materials but instead more tied to the cutting parameters.

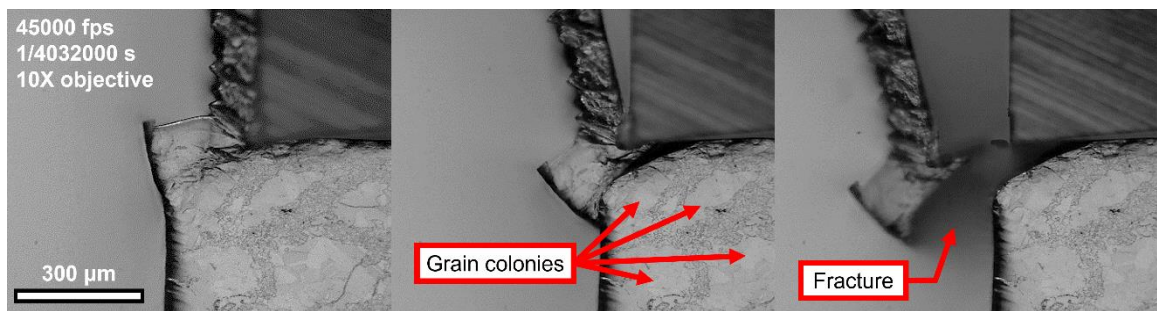


Figure 2-17. Process of fracture in negative exit burr formation ($VB = 0 \mu\text{m}$, $h = 80 \mu\text{m}$, $v_c = 60 \text{ m/min}$).

Like with all machining phenomena, the material response (in this case, the burr formation), is largely driven by the cutting parameters. In virtually all studies, it was found that the uncut chip thickness (h) had the biggest effect on burr formation in general, be it exit or side burr. Regarding negative burrs, Régnier et al. [93, 94] observed that exit burr size was proportional to h , and that negative burrs were far more likely to occur when h was large in the orthogonal machining of AlSi alloy. Nakayama and Arai [95] obtained the same result in their orthogonal machining study on 65-35 brass. Another equally important parameter is the cutting speed, as the threshold for negative burr fracture is dictated by the intensity of strain in the negative shear zone [84]. Thus, a faster cutting speed should facilitate easier negative burr formation.

However, Nakayama and Arai [95] saw the opposite effect, where a lower cutting speed favored negative burr formation. The rake angle (i.e., tool orientation) has also been shown to have a significant influence on the development of negative burrs, although findings on the effect of rake angle are contradictory: Régnier et al. [96] found that a positive rake angle could produce negative burrs, but a negative rake angle could not. On the

contrary, Nakayama and Arai [95] only saw that a smaller rake angle was desirable for negative burr formation. It should be noted that the rake angle was not a control variable in this study, as it was kept constant at zero degrees. Furthermore, the causation of rake angle, along with other machining parameters on negative burrs is not well understood—this study presents preliminary findings on the factors affecting the negative burr phenomena in Chapter 6.

2.3.2 Effects of Cutting Conditions on Burrs

It has already been made clear that tooling is heavily influential on other categories of surface integrity (surface roughness, RS, and microstructure); worn tools are generally undesirable because of their negative side effects, and this is no different for burr formation. While there is very little work on the correlation between tool-wear and burr formation, some researchers have observed that worn tools result in larger burrs [97-101]. As stated earlier, micro-machining is one of the most common operations employed in burr formation research. Burrs are especially problematic for micro-machining operations because the deburring process is more difficult than in macro-machining, where removing micro-burrs requires even higher accuracy to avoid damaging the small features of the part [102]. In their study comparing different lubrication methods in the micro-milling of Inconel 718 with coated WC inserts, Aslantas et al. [97] found that tool-wear had a significant effect on burr formation: as the end mills became more blunted because of wear, this resulted in bigger burrs because worn tools tend to plough instead of cut. This ploughing effect was also observed by Wu et al. [101] in their micro-planing experiments on copper with PCD tools. In fact, burr formation and tool-wear are so closely related that burrs are used as an indicator of tool condition (i.e., when the tool needs to be changed) [4]. This is supported by Lee and Dornfeld [100] in their micro-drilling study with WC mills on stainless steel 304. The authors found that there was a dramatic spike in burr height due to catastrophic failure in the tool after a certain number of holes were drilled (see Figure 2-18). Thus, it can be implied that less burr formation means longer tool life, and therefore, increased productivity [4].

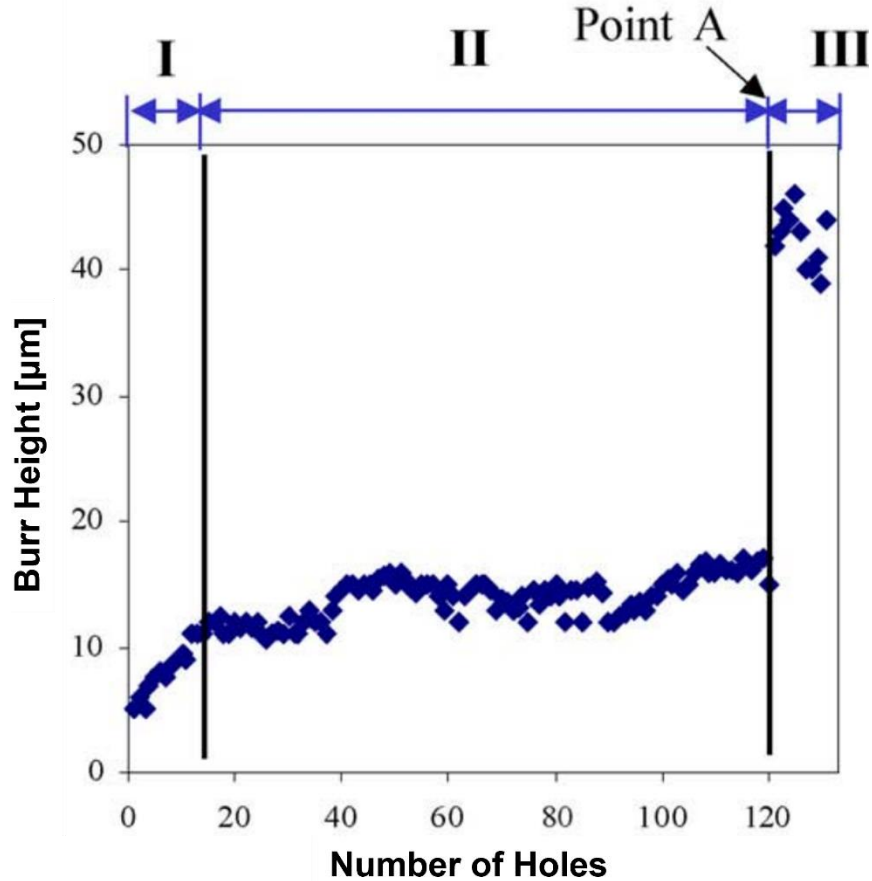


Figure 2-18. Change in burr height with number of holes drilled for stainless steel 304 (reproduced from [100] with permission of Elsevier, License Number 5427980351490).

Besides tool-wear, there are other aspects regarding tooling that have profound effects on burr formation, namely tool orientation and tool path (for milling). Multiple studies concluded that rake angle has a clear effect on exit burr formation [82, 95, 96, 98]. Ko and Dornfeld [82] and Nakayama and Arai [95] found that burr height decreases with increasing rake angle, which is because of the lower shear strain undergone by the chip [95]. A very important parameter that is pertinent to milling is tool path, which is rarely explored in literature. Dornfeld and Min [4] demonstrated this with a case study on an automotive engine block. By optimizing the tool path, the engine block went from having excessive burrs to having no burrs at all. While tool path was much longer (more than double), they were able to increase the feed rate with no consequences which resulted in the same milling time. Tool path optimization for burr minimization is a matter of avoiding geometric extremities like tool exits and maintaining a constant force on the tool [4]. István Poór et al. [77] reviewed novel drill head designs proposed by several authors that are aimed

specifically for burr control in carbon fiber reinforced polymer (CFRP) composites. One key design attribute in milling and drilling tools is the helix angle, which has been shown to influence burr formation greatly in the machining of CFRPs [103]. A larger helix angle has been shown to increase the exit burr size (both thickness and height) in the drilling of Ti-6Al-4V [104]. The drill point style and point angle also play a major role in exit burr formation—Dornfeld et al. [104] saw that helical point drills created substantially smaller burrs than split point drills and that a larger point angle results in smaller exit burr size. Thus, developing new tool designs for burr suppression in metal machining could prove promising.

The most influential cutting parameter on burr formation is the uncut chip thickness (h), as this was the most consistent relationship found among numerous researchers [82, 86, 95, 98, 102]. Generally, a higher uncut chip thickness will result in bigger burrs [82, 86, 95, 98]. Chern and Dornfeld [86] observed that exit burr height increases proportionally with uncut chip thickness in their dry orthogonal cutting experiments on copper, Al 2024-T4, and Al 6061-T6. This was validated with their burr formation model based on bending and shearing work, and results show excellent agreement. Wang and Zhang [98, 105] obtained similar results in their dry milling experiments on 6-4 brass when analyzing side burrs. On the contrary, low uncut chip thickness can still lead to large side burr formation if the uncut chip thickness to tool nose radius ratio is low, i.e., ploughing (rather than cutting) becomes dominant [98, 101, 106]. This again points back to the importance of tooling, as worn tools will exacerbate burr formation in relation to the uncut chip thickness. When the cutting-edge radius is larger than the uncut chip thickness, the maximum stress area is shifted to the bottom corner of the cutting-edge arc—this stress distribution heavily favors side burr formation [101]. Wu et al. [101] confirmed this in their micro-planing experiments on copper with diamond tools. As the uncut chip thickness approached the tool nose radius, the side burr height decreased until it reached a minimum value, after which it began steadily rising with uncut chip thickness—this concurs with the results of the previously mentioned studies.

The influence of feeds and speeds on burr formation is less conclusive than that of uncut chip thickness as there are conflicting results. Some researchers report that a higher feed rate escalates burr formation [100, 107]. Lee and Dornfeld [100] found that burr height

is linearly proportional to feed rate (see Figure 2-19), likely due to increased tool-wear, which has already been explained to have a negative effect on burr formation. Biermann and Hartmann [108] also saw a rise in burr height with increasing feed rate in their drilling experiments on steel alloy 34CrNiMo6 and aluminum alloy AlMgSi1. In addition to the depth of cut, Piquard et al. [109] state they found a strong dependency on feed per tooth for both burr height and burr thickness in the micro-milling of austenitic and martensitic NiTi. However, Kumar and Bajpai [110] state that a higher feed rate corresponded to a lower burr height in both up and down-milling. Cedergren et al. [111] analyzed the influence of feed rate with respect to grain size, which has been very scarcely explored. They performed wet turning experiments on Alloy 718 with uncoated WC inserts. Their results are quite telling, as grain size in tandem with feed rate had vastly different outcomes, as shown in Figure 2-20. With large grains ($d \sim 127 \mu\text{m}$), a lower feed rate resulted in the extreme buildup of burrs and increasing the feed rate caused the burrs to decrease heavily. With small grains ($d \sim 16 \mu\text{m}$), virtually no burrs were observed at the lower feed rate, but burrs appeared when increasing the feed rate. Other work has shown that grain orientation has a major effect on burr formation because some grains may behave in a ductile manner while others may behave in a brittle manner [112]. Hence, it is safe to assume that grain size also plays a considerable role in burr formation, which was found to be the case in the present work (to be discussed in Section 6.3). Muhammad et al. [102] deemed feed rate to be insignificant in their micro-milling experiments on Inconel 718 with coated WC inserts, as no trend could be attained. As mentioned earlier, the direction of the milling cutter has a major effect on burr development, and this has been corroborated in literature. Piquard et al. [109] showed that up-milling creates taller burrs (larger height) but down-milling creates thicker burrs (larger thickness). This was later confirmed by Kumar and Bajpai [110], who obtained a 120% increase in burr height when up-milling compared to a 50% decrease when down-milling.

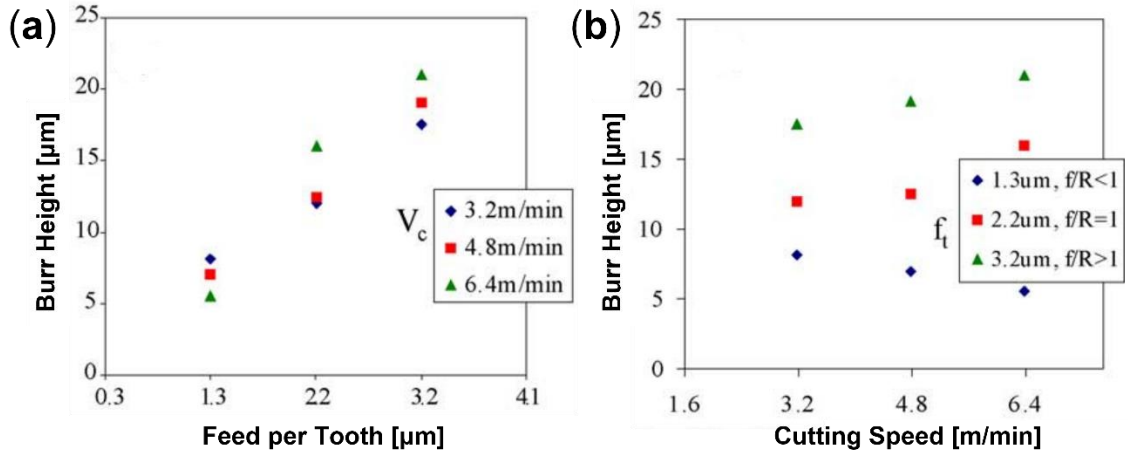


Figure 2-19. Effect of (a) feed rate and (b) cutting speed on burr height for stainless steel 304 (reproduced from [100] with permission of Elsevier, License Number 5427980351490).

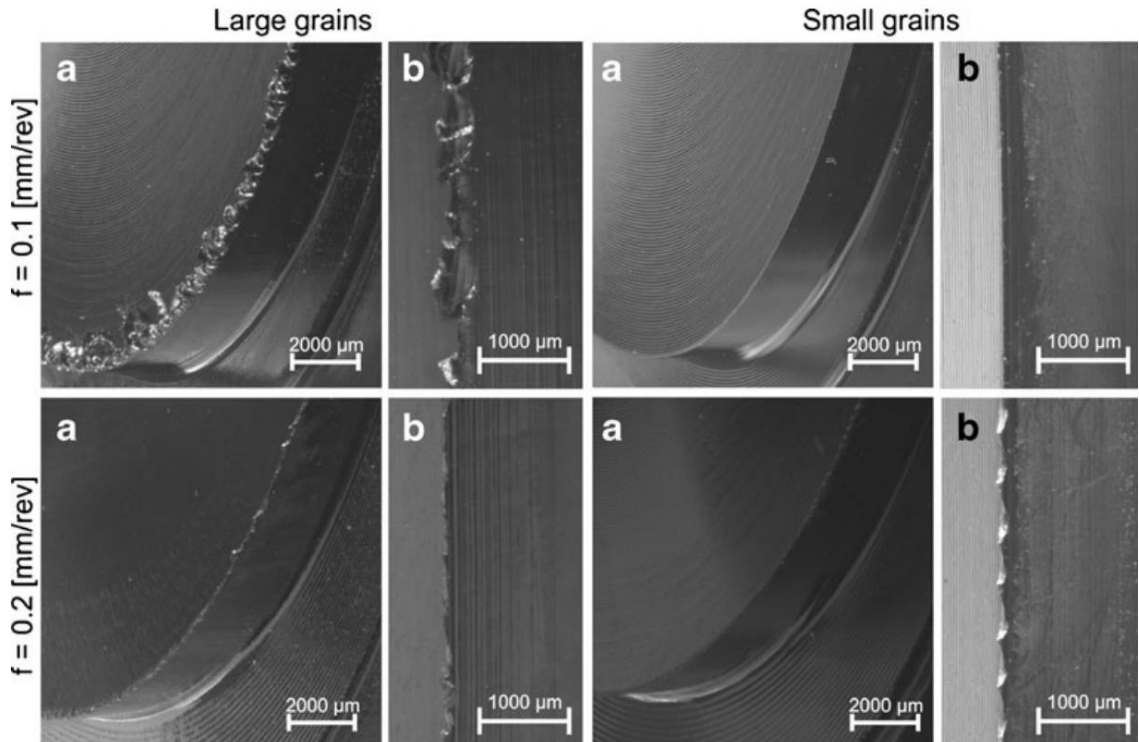


Figure 2-20. Effect of grain size and feed rate on burr formation for wrought Alloy 718 (reproduced from [111] with permission of Springer Nature, License Number 5427980508001).

Findings regarding the effect of cutting speed on burr formation are also mixed or unclear. Muhammad et al. [102] saw that increasing the cutting speed created a substantial rise in burr size, which they attribute to thermal softening causing easier plastic deformation. This is logical, as burr formation is proportional to the ductility of the material [95, 101].

On the contrary, Pilný et al. [107] saw a linear decline in exit burr height with increasing cutting speed during their drilling experiments on aluminum. Pramanik et al. [113] observed that burr height decreased with increasing cutting speed at minimum feed rate and tool point angle, but first increases then decreases with increasing cutting speed at maximum feed rate and point angle. A very similar effect was illustrated by Lee and Dornfeld [100]: they saw that burr height decreased with increasing cutting speed at a lower feed rate, but slightly increased at higher feed rates. They state that the former happens because of a combination of better tool life due to built-up edge (BUE) forming a protective layer on the tool, and laminar material flow (possibly due to thermal softening), which causes smaller burrs. Biermann and Steiner [114] tested various cutting speeds, feed rates, and lubrication conditions in the micro-milling of austenitic stainless steel X5CrNi18-10 with coated WC inserts. In most cases, they saw that top burr height increased with increasing cutting speed due to higher strain rate hardening. However, this was not the case at certain feed rates and lubrication conditions, where the burr height can be seen to increase then decrease with increasing cutting speed. The lubrication/cooling method can have a noticeable impact on burr formation, as was shown by Biermann and Hartmann [108], where they observed a slightly smaller burr height in cryogenic drilling of steel alloy 34CrNiMo6. Moreover, they stated that dry drilling resulted in significantly larger heights because of the lack of thermal softening. Additionally, whenever the burr height would increase with cutting speed, the trend was never consistent and would vary widely. Other authors, however, noticed the opposite effect. Like feed rate, there is no clear relationship between burr formation and cutting speed based on current literature.

3.1 In-Situ Testbed for High-Speed Imaging of Orthogonal Cuts

Experiments were carried out on a custom-built, state-of-the-art in-situ testbed, shown in Figure 3-1. The testbed is contained within a welded, steel frame housing and sits on a ~2-ton granite surface filled with sandbags for vibration-dampening. The testbed mechanism consists of a table capable of moving in the x and y-directions for 2D-motion, which is powered by a Yaskawa experimental series SLGFW2 linear servo motor that allows it to reach speeds of 252 m/min with 5 Gs of acceleration. The workpiece sample is secured by a 0.25-inch (6.35 mm) screw and two 0.25-inch dowel pins within a vice sitting atop the table; the vice is equipped with Kistler Type 9047C piezoelectric force sensors with a force capacity of 30 kN. The cutting tool is secured in a rigid fixture that moves vertically (z-direction) via a carriage mechanism for controlling the desired depth of cut. The tool fixture is designed to hold K68 WC inserts. Prior to each cut, the z-axis is held steady with two clamps to prevent tool displacement. A micro-mill was installed for deburring the workpiece edges following each experiment, which would be accomplished using an automatic program in the machine. Focusing on the tool-workpiece interface is an ultra-high-speed Photron FASTCAM SA-Z 2100k camera capable of capturing video up to 2.1 million fps: the camera features a microscope containing a high-intensity, co-axial 5000 lumen LED light source for illuminating the cuts. There are additional 4000 lumen LEDs delivered via a bifurcated light guide for illuminating the chip during cutting that are connected to an external HelioLux power source. A Mitutoyo M Plan APO 10X magnification objective was used as the microscope lens on the Photron camera. There was an additional Vieworks VC-25M digital camera constructed from Thorlabs components attached to the vertical z-carriage also utilizing the same Mitutoyo M Plan APO 10X objective for photographing the machined surface before and after cuts.

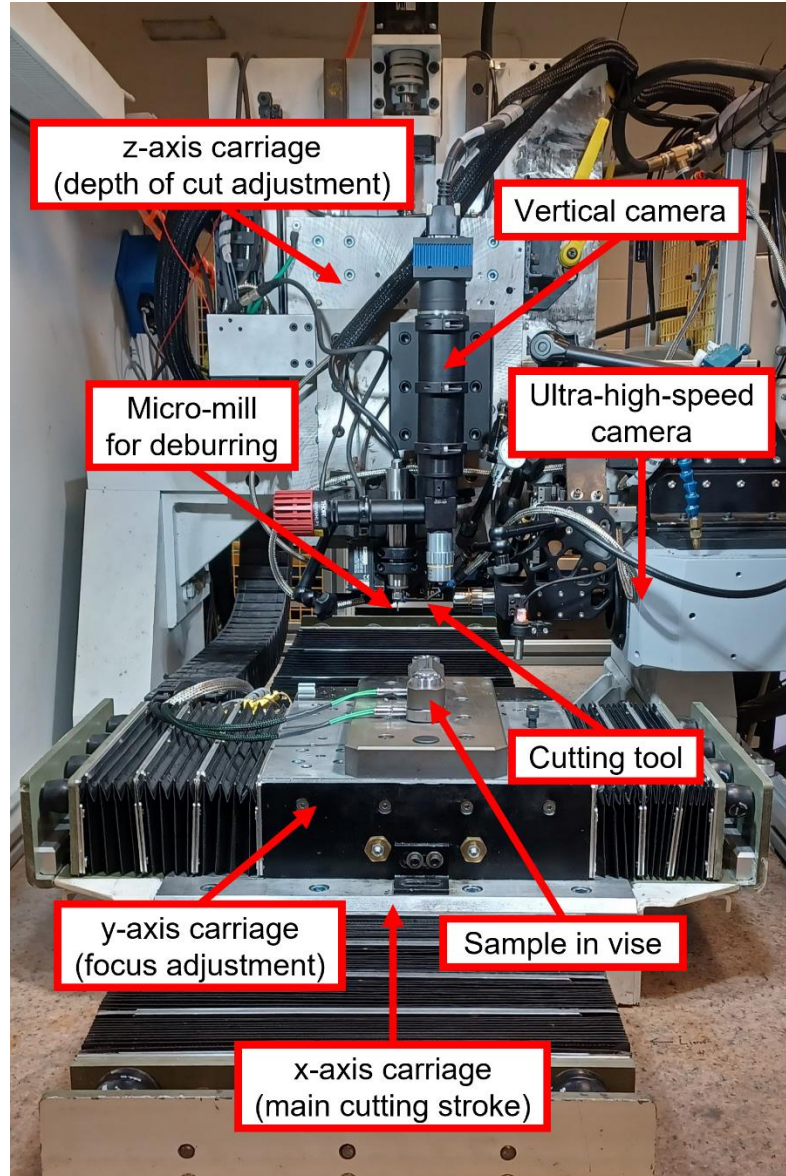


Figure 3-1. In-situ testbed used for physics-informed and data-driven characterization of machining processes.

The objective of this study was to gain a comprehensive understanding of burr initiation and formation by analyzing how these aspects differ with respect to various process parameters. The key factors of interest that were modified in the experiments are the uncut chip thickness, tool-wear, and cutting speed. Four levels of uncut chip thickness (h) were measured: 10, 20, 40, and 80 μm (increasing by factors of two). Three tool flank-wear (VB) conditions were used: 0 μm (i.e., sharp), 50 μm , and 150 μm . Finally, the cutting speed (v_c) ranged from 6 to 60 m/min. These levels were carefully chosen based on their expected influence on the burr formation and relevance in finish machining. It was highly

anticipated that the uncut chip thickness would be the driving factor, which is why it has the most settings. Additionally, 10-80 μm would cover the entire range seen in finish milling. The highest flank-wear condition was selected as 150 μm because typically the most extreme level that would be seen in practice; it was scaled down by factors of a third from there. The cutting speed was not expected to have a notable effect, which is why it was only tested at two settings. The higher speed of 60 m/min was chosen because it is the industry standard for cutting Inconel 718 with uncoated WC. Further, the two cutting speed settings differed by a factor of 10 to ensure that any significant effects of cutting speed would still be revealed. The experimental matrix for the in-situ trials is displayed in Table 3-1.

Table 3-1. Experimental matrix for in-situ trials.

| Cutting Speed (v_c) [m/min] | Flank-Wear (VB) [μm] | Uncut Chip Thickness (h) [μm] |
|---------------------------------|---------------------------------------|------------------------------------------------|
| 6 | 0 | 10 |
| | | 20 |
| | | 40 |
| | | 80 |
| | 50 | 10 |
| | | 20 |
| | | 40 |
| | | 80 |
| | 150 | 10 |
| | | 20 |
| | | 40 |
| | | 80 |
| 60 | 0 | 10 |
| | | 20 |
| | | 40 |
| | | 80 |
| | 50 | 10 |
| | | 20 |
| | | 40 |
| | | 80 |
| | 150 | 10 |
| | | 20 |
| | | 40 |
| | | 80 |

3.2 Sample and Tool Preparation

3.2.1 Sample Polishing and Etching

The Inconel 718 workpiece sample used was in the quenched and age-hardened condition of 46 \pm 2 HRC with a bimodal grain distribution ranging from average grain sizes of 3-8 μ m to 50-500 μ m. According to manufacturer data sheets, it has a yield shear stress (i.e., flow stress) of 640 MPa, an Elastic Modulus of 205 GPa, and a Poisson's ratio of 0.28. The workpiece was cut from the ingot using wire electrical discharge machining (EDM) and milled into a rectangular geometry of dimensions of about 50 mm x 40 mm x 6 mm. A step was milled on both sides to form cutting widths of 3 mm to ensure plane strain conditions. Additionally, five 'castellations' (i.e., 'edges') with spacing of 8, 7, 6, 5, and 4 mm were milled out on one side for a discontinuous cutting stroke to facilitate burr formation and to allow for five data points to be collected with each trial. The in-situ workpiece and its microstructure are shown in Figure 3-2.

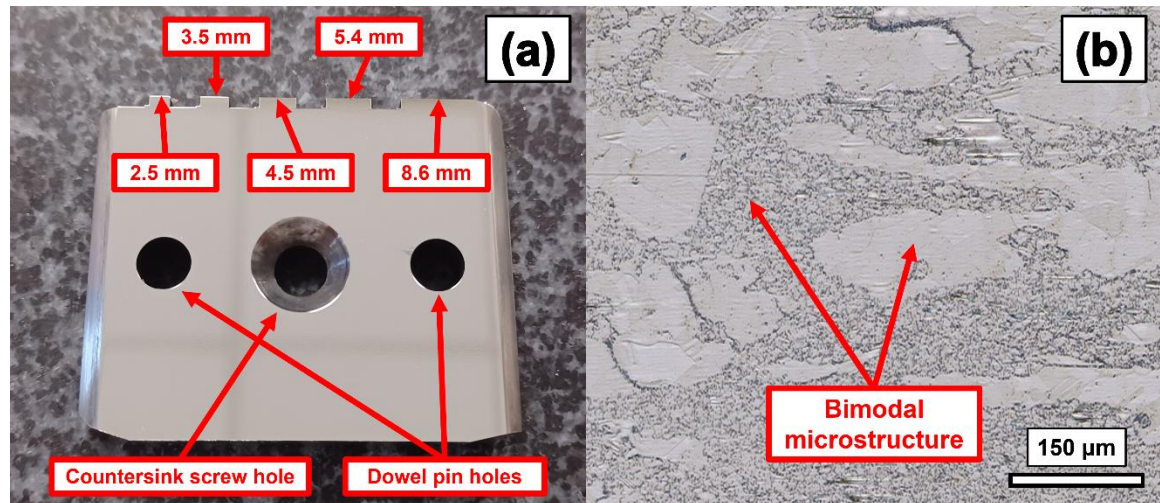


Figure 3-2. Images of (a) geometry and (b) microstructure of slotted and polished Inconel 718 in-situ workpiece sample.

To reveal the microstructure and obtain the necessary reflective finish in the high-speed video for digital image correlation (DIC) measurements, the workpiece underwent a thorough polishing and etching process. Several sandpaper and diamond pads were used for polishing—the sample was fastened to a holder and pressed down with even pressure onto the pads spinning on a Struers RotoPol-22 polishing machine. The polishing recipe

used is a modified version of the standard recipe provided by Pace Technologies and is shown in Table 3-2. After polishing, the workpiece was etched for ~1 min using a custom mixed chemical formula: 100 mL methanol, 100 mL HCl, 5 mL HNO₃, and 10 g of Cu₃Cl₂. The polishing and etch quality were checked on a Nikon Epiphot 300 microscope before experiments were run. After the exit burrs were grinded off the workpiece with the micro-mill, the sample underwent Steps 5-9 of the polishing recipe again to remove the side burrs from the previous cut—this would yield a “burr-free” workpiece for the following trial.

Table 3-2. Polishing recipe for Inconel 718 in-situ workpiece.

| Step | Abrasive Pad | Speed |
|------|-------------------------------------------------------|---------|
| 1 | 120 grit SiC paper with water | 150 rpm |
| 2 | 240 grit SiC paper with water | 150 rpm |
| 3 | 360 grit SiC paper with water | 150 rpm |
| 4 | 600 grit SiC paper with water | 150 rpm |
| 5 | 9 μm DIAMAT diamond liquid on POLYPAD polishing pad | 300 rpm |
| 6 | 9 μm DIAMAT diamond liquid on TRICOTE polishing pad | 300 rpm |
| 7 | 6 μm DIAMAT diamond liquid on TRICOTE polishing pad | 300 rpm |
| 8 | 1 μm DIAMAT diamond liquid on TRICOTE polishing pad | 300 rpm |
| 9 | 0.5 μm DIAMAT diamond liquid on TRICOTE polishing pad | 300 rpm |

3.2.2 Tool Sharpening and Imposition of Flank-Wear

The cutting tools used in all experiments were K68 uncoated WC from Kennametal, which were prepared by following a multi-step grinding recipe. First, the flank face of the as-received tool blanks was ground along the flank face at a 5° clearance angle (to match the alignment of the in-situ testbed fixture) against a ~30 μm abrasive vitrified bond diamond wheel (150 mm diameter) spinning on a Taig Tools 4019 DSLS CNC Lathe to a flank clearance facet width of about 2 mm. Next, the tool would be placed into a handheld grinding fixture (also calibrated to a 5° angle) used on precision granite surface plates to ensure flatness and repeatability, where the flank would be rubbed against various lapping film pads embedded with diamond abrasive grains from McMaster-Carr: 30, 9, and 3 μm pads were used. The flank would be lowered on the spindle of the fixture until it was just pinching the pad against the granite plate’s surface, then it would be ground in a back and forth, linear motion until a uniform finish was achieved, after which it would proceed to the next diamond abrasive pad. For sharp tools, the flank would first be polished on the 30

μm pad, followed by the 9 μm , and finally the 3 μm until a ‘shiny’ finish was achieved. Lastly, the sharpness of the tool would be checked on the Nikon Epiphot 300 microscope. This same procedure was done manually by hand for the rake face as well and for both sides of every tool.

A more complicated process was required for worn tools: one side would be ground sharp as described above, but the other side would be made worn. For the worn side, following the initial grinding on the lathe, the tool was first polished on the 30 μm abrasive pad in the 5° holder on the handheld fixture, but would then be switched over to a special flank-wear holder that is at an angle of 0° to induce a controlled wear flat/facet on the flank face, parallel to the workpiece surface. Once the tool was in the flank-wear holder, it would be pressed down until it was barely making contact on the 3 μm abrasive pad. Then, the fixture would be stroked backwards and carefully abraded to impose the flank-wear. Assuming the stroke was uniform and straight, a thin strip of flank-wear should have been added. The accuracy of the flank-wear would be verified by placing the tool under the Nikon Epiphot 300 microscope. The wear was then measured at three different points along the flank face to ensure that it was within tolerance. If the flank-wear contour was not adequate, the tool would be placed back into the 5° holder, polished on the 30 μm abrasive pad until the wear from the 3 μm was removed, then returned to the wear holder and the process would repeat until the wear was within a sufficient tolerance of the target value (50 or 150 μm). After adding the flank-wear, the tool would be honed to a certain radius by grinding the cutting edge (i.e., where the flank and rake faces meet) on a 150 mm diameter buffing wheel charged with 1 μm diamond abrasive, spinning on a DeWALT DW758 bench grinder. The hone, verified using a Zygo NewView 7300 scanning white light interferometer, was a uniform radius of 20 μm for tools with 50 μm of flank-wear and a radius of 30 μm for tools with 150 μm of flank-wear. These hone values were established based on previous measurements of the relationship between edge radius increase with progressive flank wear in turning and milling of Inconel 718 (unpublished data, Schoop Research Group). The flank-wear can be seen in Figure 3-3.

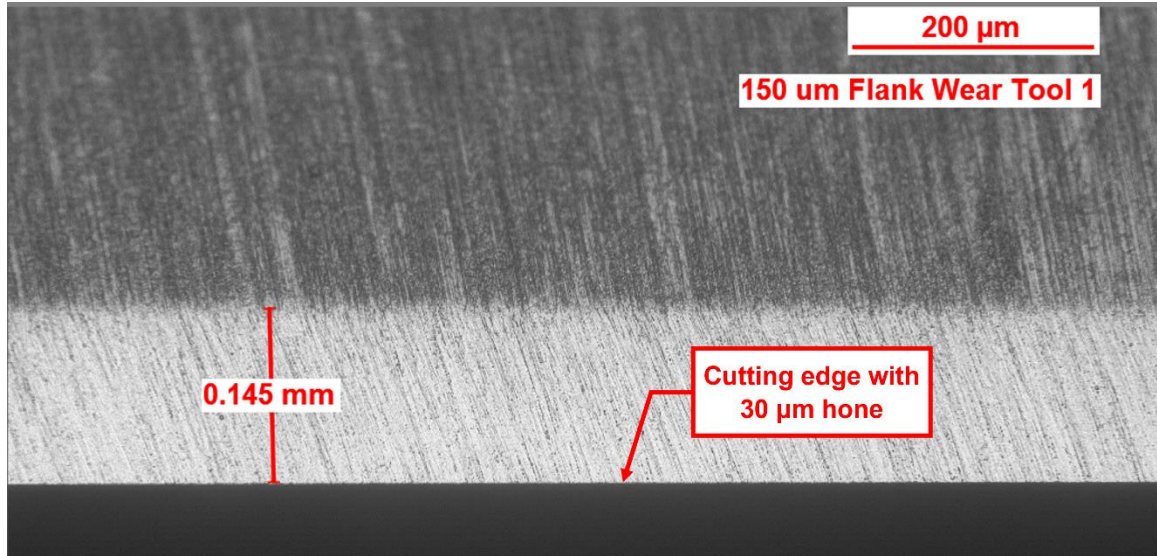


Figure 3-3. Flank-wear ($VB = 150 \mu\text{m}$) and hone ($r_\beta \sim 30 \mu\text{m}$) for a worn tool.

3.3 Force Measurement

Force data was captured using the Kistler Type 9047C piezoelectric sensors encased in the vice holding the workpiece on the in-situ testbed. There were two sensors (one for each force component in the cutting and feed directions), each wired to a Kistler Type 5010 dual-mode amplifier that output the forces as voltages on separate channels. The voltage readings were displayed and captured using MATLAB's Analog Input Recorder at a rate of 333,333 scans/second. The duration of the recording would be set to 30 seconds for the slow-speed (6 m/min) cuts and 10 seconds for the high-speed (60 m/min) cuts to give ample time to capture the entire length of the sample.

Since force data was captured in volts, a conversion factor was necessary. The conversion factor of force units per volt was determined based on the NIST-traceable laboratory calibration certificates for the Kistler triaxial load cells. These conversion factors were 2999 N/volt and 2996 N/volt for the cutting and feed forces, respectively. The voltage readings were then analyzed using a MATLAB script (shown in Figure A1 of the Appendix) to calculate the average cutting and feed forces. The script searched for the number of 'change points' (ten total, two per castellation), which is essentially whenever cutting was taking place, as the plot would jump up during contact with the tool then drop down when the tool left the workpiece. There were ten total change points per data set (two

per each of the five castellations), that would each be averaged. The script would then calculate the mean of those five averages and would furthermore yield the forces of the cut. This process is illustrated in Figure 3-4.

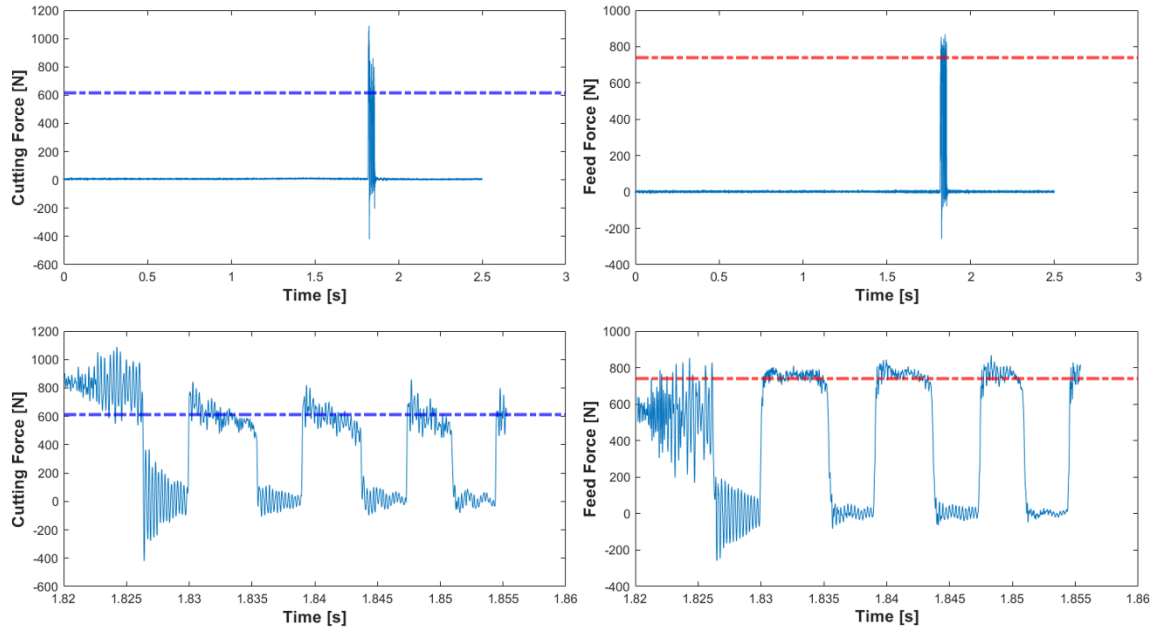


Figure 3-4. Calculation of force averages in MATLAB.

3.4 Displacement Measurement

The subsurface displacement fields (i.e., strain fields) were characterized using the non-contact DIC technique, which requires ‘reference’ and ‘current’ frames to generate the degree of displacement for the grains. To do this, the sample was recorded twice: once before the cut and once during the cut. The recording before is simply a ‘fly-over’—the sample is being moved in front of the camera where there is a gap between the top surface and the tool, so no cutting is taking place. The images captured here served as the reference frames for the DIC analysis. Then, there was of course recordings during the cut itself, which served as the current frames for the DIC analysis. Finally, the two frames could be fed into open-source DIC software, Ncorr, which would generate the displacement field by finding the relative displacement between the pixels. This procedure is illustrated in Figure 3-5.

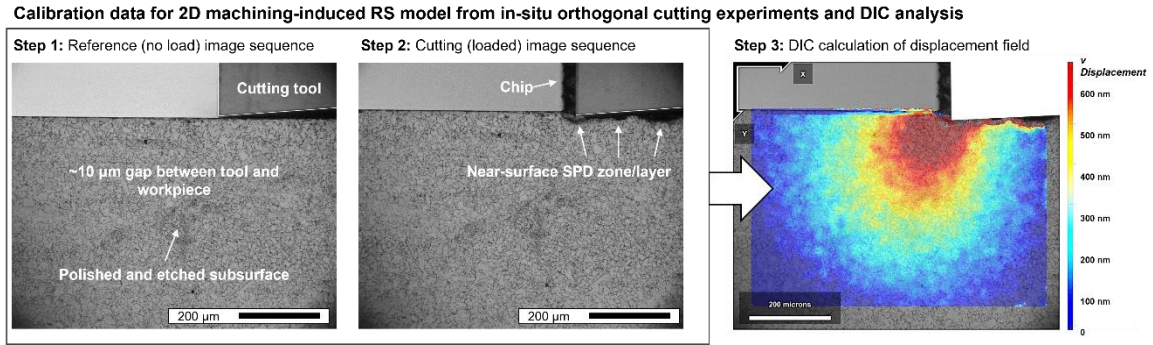


Figure 3-5. In-situ imaging procedure for conducting subsurface analysis with DIC (reproduced from [115] with permission of Springer Nature, License Number 5427980654590).

Once the cutting tool was resting in the fixture, the camera would be moved to bring the tool tip into view. Once the tool was positioned in the upper right-hand corner of the frame, the camera would be adjusted to focus on the cutting tool. Next, the table would jogged over in front of the camera and the tool would be lowered carefully until the workpiece came into frame. Once the tool and workpiece subsurface were clearly visible in view of the camera, the sample would be jogged in the y-direction until it was also in focus—this was an indicator that the tool and workpiece were in the sample plane. Finally, the workpiece would be moved back in the positive y-direction by 30 μm to create a sufficient overhang of the tool to prevent side flow around the tool (as well as allow for side burrs to emerge). The camera would then be adjusted one more time to focus on the sample (of which the tool would go out of focus, as expected).

The FASTCAM SA-Z camera settings had to be adjusted properly before each recording, which was done using the Photron FASTCAM Viewer (PFV) Version 3.6.9.1 software. The resolution was set to 640 x 640 pixels and the frame rate was set to 4,500 and 45,000 for the 6 and 60 m/min cuts, respectively—the exposure was constant at 1/4032000 s throughout to eliminate motion blur during high-speed cuts and maintain constant image brightness across all conditions. These settings were developed internally at the Integrated Computational & Experimental Manufacturing Engineering (ICEME) Laboratory at the University of Kentucky to balance maximum field of view with sufficiently high frame rate to observe dynamic events such as chip serrations and burr formation. A shading correction was applied periodically to eliminate noise.

After each experiment, individual frames for the fly over and cut had to be selected from the ~1,800 frames captured per pass. This required close attention to select the most optimal frames to yield the best results for DIC. Ideal frames were first and foremost perfectly in focus, contained few surface defects like scratches, and had the correct level of contrast. Improper selection of the reference and current frames results in poor displacement fields after DIC analysis. Thus, the three best pairs were identified for each experimental condition—that is, three different groups of frames (each containing one fly over and one cut frame) were chosen and ranked in order of preference. Once the best frames were chosen, they were analyzed via open-source DIC software, Ncorr, for comparison.

Ncorr was run via MATLAB Version R2021b. The first step to performing the DIC analysis was to draw the region of interest which was as a rectangle over the workpiece subsurface. For the DIC parameters under the “Analysis” tab, the subset radius was set to 10 with subset spacing of 1. The iterative solver options were kept at the default settings of 1×10^{-6} for the diff. norm C/O and 50 for the iteration # C/O. Single threading was used. Step analysis was enabled with auto seed propagation at a step # of 5. Subset truncation was enabled for discontinuous analysis. After the analysis was complete, the displacements were formatted by applying a unit conversion (calibration factor) of 2 microns/pixel and the maximum correlation-coefficient cutoff was used. These various settings were iteratively determined to yield the optimum signal to noise ratio in the calculated displacement plots, without requiring excessive computational time. The plots of interest were the v-displacement plots, which were always viewed using the Eulerian description. To form the final plot, the upper and lower bounds were adjusted to yield the most refined displacement field with distinct transitions between regions by fixing the upper bound (typically red/maroon color in MATLAB ‘jet’ color scale) approximately equal to the region of plastic deformation.

3.5 Optical Microscopy for Capturing Burrs

A Keyence VHX-7000 digital microscope (shown in Figure 3-6) was used for analyzing burr geometry. The machined workpiece would be placed under the microscope and scanned at each castellation after each trial. First, high definition 2D images of each of the five exit burrs were taken using the ‘z-depth up’ feature; the ‘remove reflection’ option was enabled to eliminate glare. Objectives ranged from 400X to 1500X depending on the size of the burr. The exit burrs were then scanned from a vertical top view using the ‘3D image-stitching’ feature at 400X magnification (the sample was propped up vertically under the microscope for this procedure). Finally, the side burrs were also captured using the 3D image-stitching feature at 200X magnification—2D and 3D images of the image-stitch were saved for each castellation. The sample was propped at an upward angle so that the side burrs would be visible under the microscope lens. Additionally, the vertical microscope installed on the in-situ testbed was used for capturing images of the side burrs from above (images were automatically taken by the camera using a MATLAB script, shown as Figure A2 of the Appendix). All images were saved as TIFF (tag image file format) files for maximum quality.



Figure 3-6. Keyence VHX-7000 digital microscope used for scanning and measuring burrs.

4.1 Exit Burr Development

This section presents the in-situ profiles for positive exit burrs and discusses the significance of the three cutting parameters on a variety of different exit burr metrics (negative exit burrs will be discussed in Chapter 6). Following the discussion of the exit burr formation mechanism in Section 2.3.1, once the tool passes over the edge, if no fracture occurred, then a ‘positive’ exit burr is left. This is given by a sharp, pointy shape of material that has extruded outward—the process of positive exit burr development was shown in Figure 2-15. Furthermore, for the purpose of characterizing the burr, there are several metrics that were first introduced by Schäfer [87] and later expanded upon by Ko and Dornfeld [82]. A schematic of these parameters is shown in Figure 4-1.

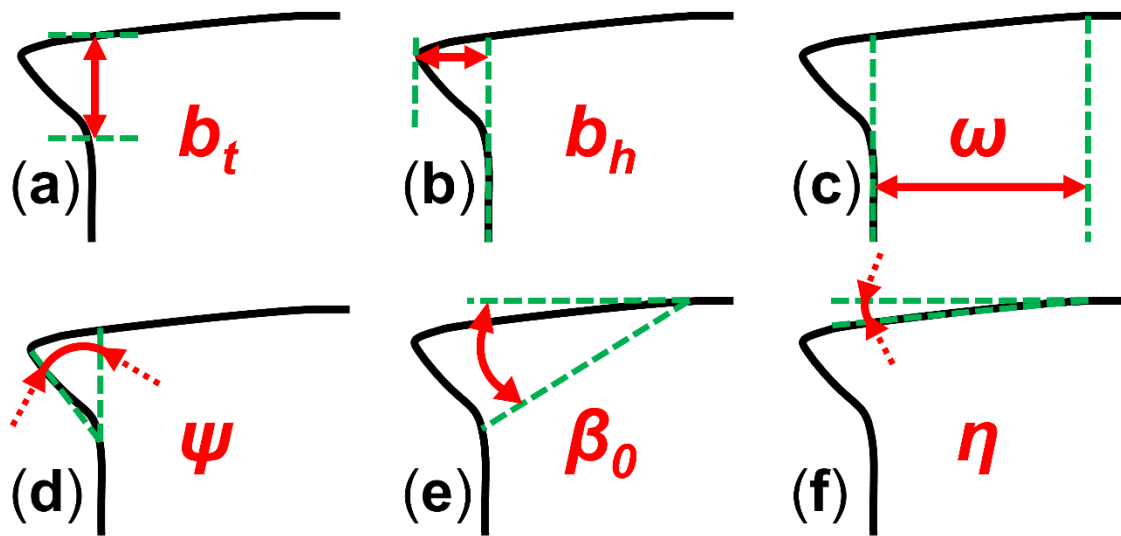


Figure 4-1. Schematic representation of exit burr parameters: (a) thickness (b_t); (b) height (b_h); (c) initiation distance (ω); (d) inclination angle (ψ); (e) initial negative shear angle (β_0); (f) initiation angle (η).

The two most pertinent metrics are the exit burr thickness (b_t) and exit burr height (b_h), as they are the most indicative of the overall size. As can be seen in Figure 4-1a, b_t is the depth from the top of the exit burr down to the burr root (i.e., from Figure 2-16). From Figure 4-1b, b_h is the distance that the exit burr extrudes outward from the vertical edge of the workpiece. Figure 4-1d shows the inclination angle (ψ), which is a measure of

the acuteness of the exit burr. Figure 4-1f shows a previously unidentified angle that is coined as the initiation angle (η) in the present work. This angle was observed on the workpiece after each machining trial as a shallow, acute angle beginning from the top of the machined surface and leading down to the tip of the exit burr. Previous studies, like that of Ko and Dornfeld [82], never noted this angle, as they depicted the top of the workpiece as being flat. The present work found this not to be the case, and that η is actually a very important parameter for distinguishing the burr initiation point, which is what allowed for the initial negative shear angle (β_0) and initiation distance (ω) to be measured optically. Besides η , there are no other visual indicators for when exit burr formation starts relative to the vertical edge of the workpiece. Further, the initiation point (beginning of η) clearly shows the transition between steady state chip formation and exit burr formation when viewing the sample from above, as shown in Figure 4-2.

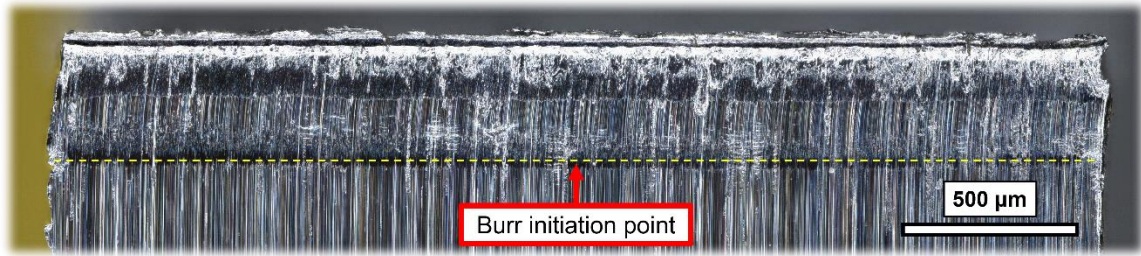


Figure 4-2. Visual of burr initiation point from a vertical view of the machined surface.

Figures 4-3-4-8 display the measured profiles for the metrics from Figure 4-2. Their variation with respect to the cutting parameters of true uncut chip thickness (h_{true}), tool-wear (VB), and cutting speed (v_c) are discussed in the subsequent sections (4.1.1-4.1.3). All data was analyzed with respect to h_{true} instead of the programmed uncut chip thickness (h) because of the well-known minimum uncut chip thickness or ploughing effect, as well as the finite stiffness of the machine, which resulted in the cutting tool being ‘pushed out’ of the cut. Values for h_{true} were measured optically via the high-speed video by calculating the difference in height between the machined and pre-machined surfaces.

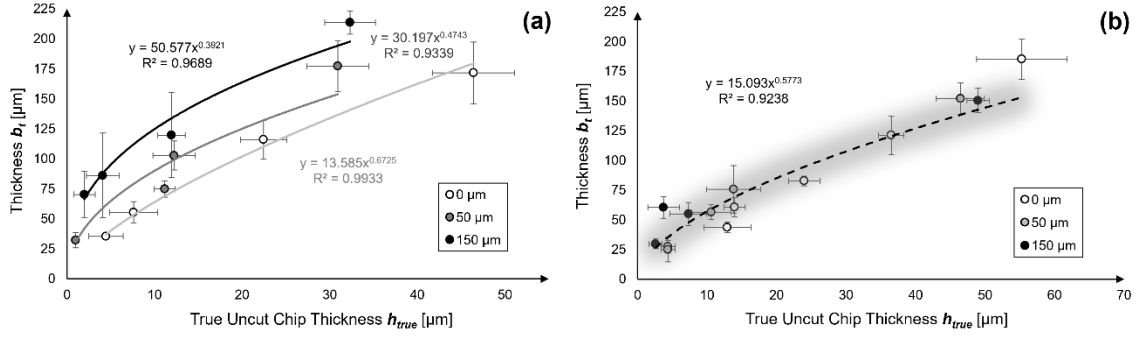


Figure 4-3. Average profiles for exit burr thickness (b_t) at (a) $v_c = 6$ m/min (significant effect of tool-wear) and (b) $v_c = 60$ m/min (no significant effect of tool-wear).

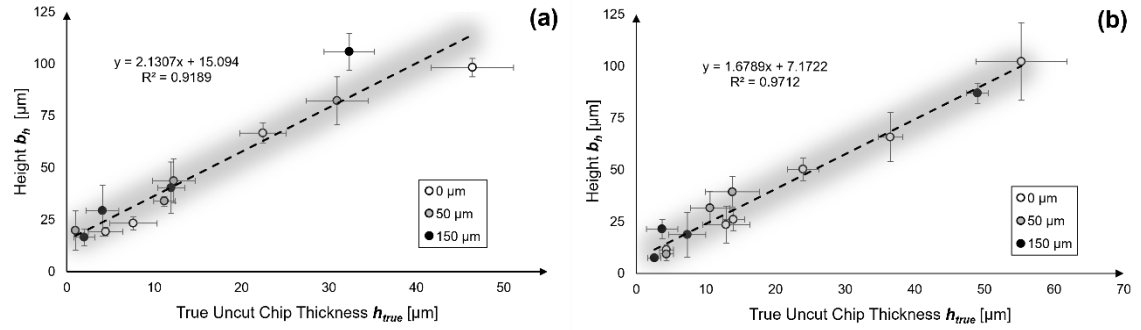


Figure 4-4. Average profiles for exit burr height (b_h) at (a) $v_c = 6$ m/min and (b) $v_c = 60$ m/min. No significant effect of tool-wear.

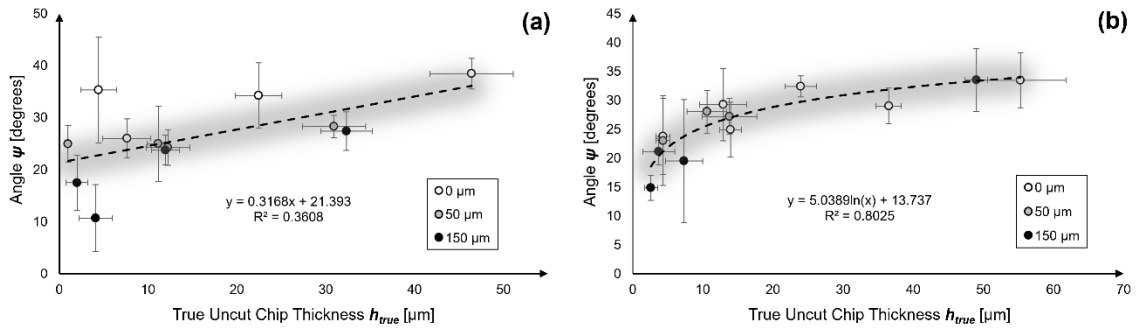


Figure 4-5. Average profiles for inclination angle (ψ) at (a) $v_c = 6$ m/min and (b) $v_c = 60$ m/min. No significant effect of tool-wear.

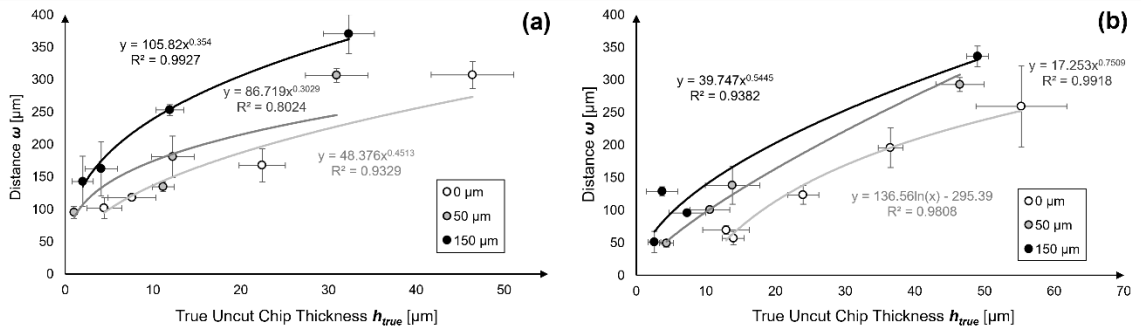


Figure 4-6. Average profiles for initiation distance (ω) at (a) $v_c = 6$ m/min and (b) $v_c = 60$ m/min. Significant effect of tool-wear.

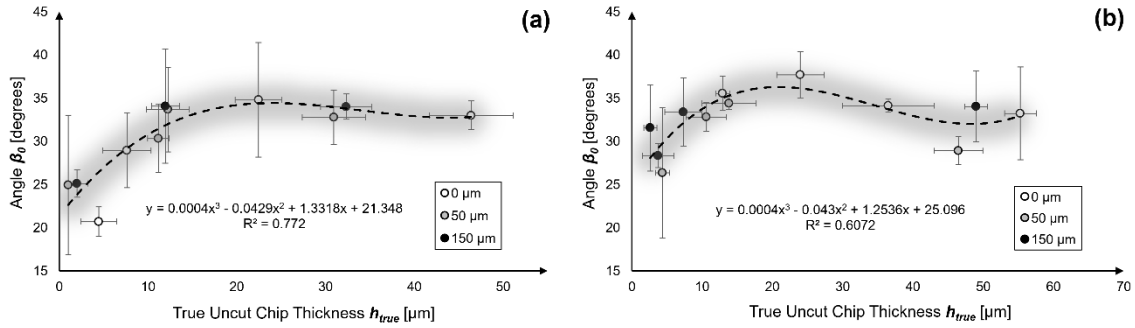


Figure 4-7. Average profiles for initial negative shear angle (β_0) at (a) $v_c = 6$ m/min and (b) $v_c = 60$ m/min. No significant effect of tool-wear.

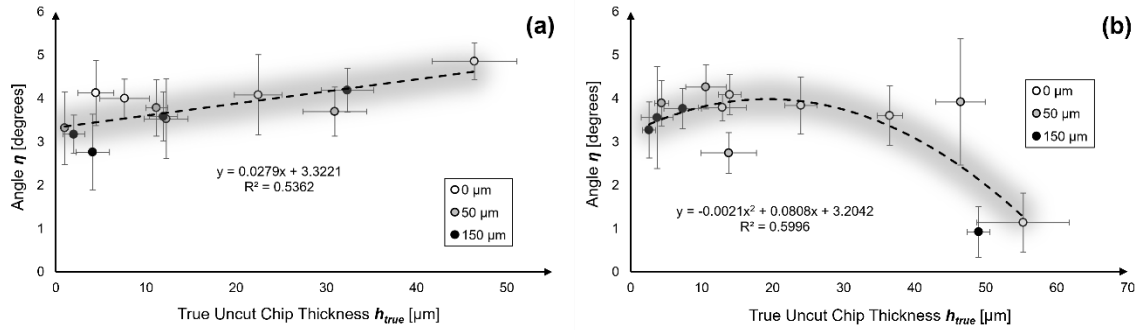


Figure 4-8. Average profiles for initiation angle (η) at (a) $v_c = 6$ m/min and (b) $v_c = 60$ m/min. No significant effect of tool-wear.

4.1.1 Effects of Uncut Chip Thickness on Exit Burrs

The true uncut chip thickness (h_{true}) was the single most influential parameter having a statistical significance on the 95% confidence interval for nearly all the profiles. All trends showed an increase as h_{true} increased. Regarding the overall burr size, which as stated previously, is indicated by exit burr thickness (b_t) and exit burr height (b_h), all curves always increased considerably with h_{true} . This is to be expected, as it is reasonable to assume that larger cuts will result in larger burrs. This was also the conclusion of numerous authors [82, 86, 95, 98, 102]. Moreover, the inclination angle (ψ) increased slightly with h_{true} .

The exit burr initiation distance (ω) exhibited a major increase with h_{true} , which is in line with the theory that larger cuts will result in larger burrs and thus initiation will

start sooner; this is supported by other works [82, 96]. As a side note, despite not being a variable of interest in this study, Régnier et al. [96] found that a positive rake angle resulted in a higher ω , whereas a negative rake angle resulted in a lower ω . This is an interesting observation that could be undertaken with another in-situ study in the future. Interestingly, the initial negative shear angle (β_0) was almost constant with h_{true} , increasing at very low h_{true} to a steady state between 30-35°, where the regression exhibited a cubic trend. This average is considerably different than in the work of Ko and Dornfeld [85], who saw that β_0 was constant at 20° for both copper and aluminum. As stated earlier, the newly identified initiation angle (η) is a very shallow angle, and the regression analysis revealed it to range between 2-5°. There was no statistical significance of h_{true} on η , however at the highest programmed uncut chip thickness ($h = 80 \mu\text{m}$) and highest cutting speed ($v_c = 60 \text{ m/min}$), η would decrease to as little as $< 1^\circ$ because of a cavity that formed (see Figure 4-9). Régnier et al. [93] also saw this cavity and attributed it to the stress triaxiality, which could be used for modeling efforts in burr formation as it characterizes the strain at fracture [116].

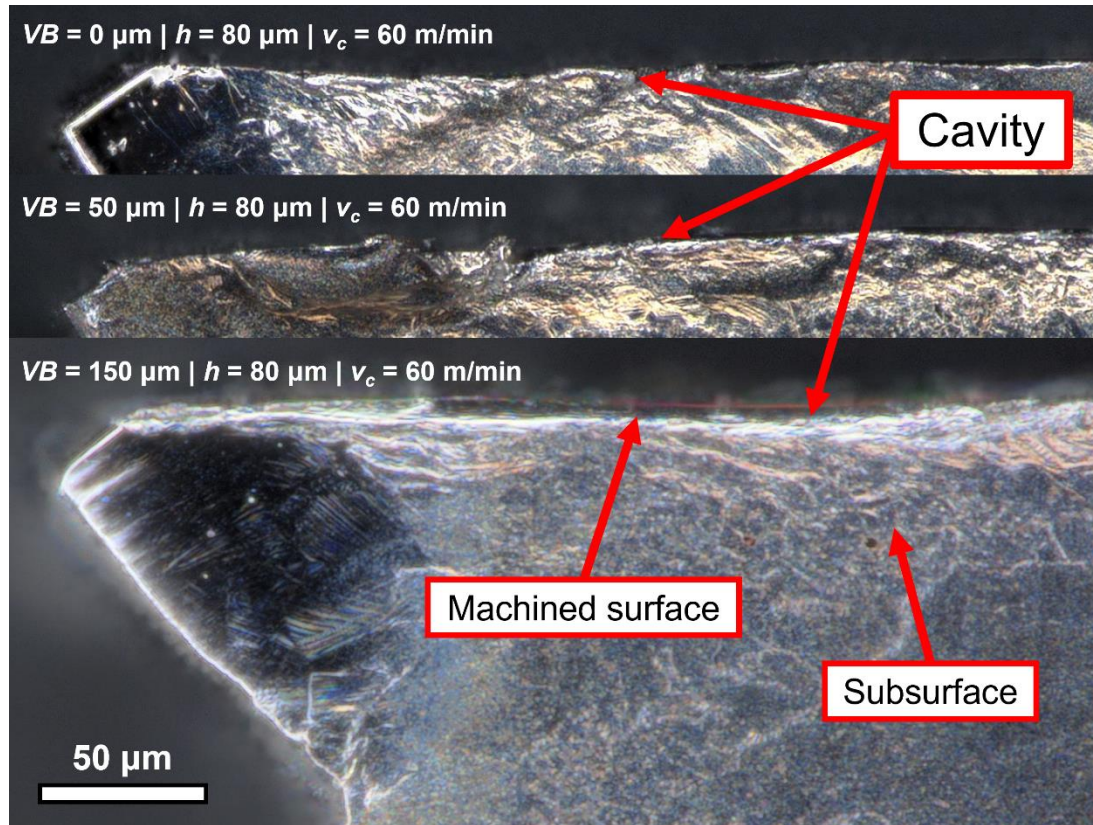


Figure 4-9. Side view of cavity at the top of exit burrs observed at high uncut chip thickness ($h = 80 \mu\text{m}$) and high cutting speed ($v_c = 60 \text{ m/min}$).

4.1.2 Effects of Tool-Wear on Exit Burrs

Interestingly, tool-wear did not have a major effect on the exit burr formation for most of the metrics. For the exit burr thickness (b_t) and exit burr height (b_h), tool-wear only had a statistical significance on b_t at the low cutting speed (Figure 4-3a). This is likely due to the lack of thermal softening, and therefore excessive amount of cold work and strain hardening associated with cutting at low speeds with worn tools. It is believed that the thermal softening at high cutting speed counteracts these effects, and therefore mitigates heightened plastic deformation in the subsurface of the workpiece, which would control the exit burr thickness. However, b_t at high cutting speed, b_h , the initial negative shear angle (β_0) and the inclination angle (ψ) were all insensitive to tool-wear. While there is no literature investigating the influence of VB specifically, there have been studies that have attempted to define the correlation between tool-wear and burr formation. Lee and Dornfeld [100] showed that b_h only increased dramatically when there was catastrophic tool-wear in micro-drilling (Figure 2-18). Several authors observed that a higher tool nose radius results in a higher b_h because of material side-flow due to ploughing [98, 99, 117]. Wang and Zhang [105] showed that b_t also increases with nose radius in face milling.

While the exit burr geometry appeared to be independent of tool-wear, the initiation distance (ω), was not. As can be observed in Figure 4-6, there was statistical significance at both cutting speeds, which means that exit burr initiation started sooner for increasing levels of wear. There seems to be a connection between b_t at low cutting speed and ω regarding tool-wear, as both increased for higher values of VB . This can be explained by the fact that worn tools create a larger mechanical stress field in the workpiece subsurface in front of the tool [118]—this is a direct result of the increased contact area between tool and workpiece due to the added flank-wear. A larger stress field in turn means deeper deformation, thus resulting in a larger b_t at the exit because the burr root would be shifted downward. A much more detailed analysis of the subsurface displacement and stress was undertaken using DIC, and the results will be discussed in Chapter 5.

4.1.3 Effects of Cutting Speed on Exit Burrs

An illuminating result of the present work is that the cutting speed did exhibit a considerable effect on exit burr development, as its influence was found to be unclear based on other studies [100, 102, 107, 114]. For instance, from Figure 4-3, the exit burr thickness (b_t) was on average 30% higher at the low cutting speed compared to the high cutting speed. Also, as stated earlier, the effect of tool-wear on b_t became prevalent at low cutting speed because of increased cold work and strain hardening, which causes deeper subsurface deformation (and therefore a lower burr root). However, the thermal softening at high cutting speed counteracted this, and rendered VB insignificant. Again, speaking to the effect of cold working, the low cutting speed produced 36% higher values of initiation distance (ω), indicating that exit burr formation starts sooner under low cutting speed conditions. Exit burr height (b_h) was deemed constant across cutting speeds in the present work, but again, literature results are inconclusive. Lee and Dornfeld [100] and Nakayama and Arai [95] saw that b_h decreased with increasing cutting speed when the uncut chip thickness was small, but it began increasing with increasing cutting speed after a certain point. On the contrary, Pilný et al. [107] only observed a decreasing trend as the cutting speed was increased. Moreover, inclination angle (ψ), initial negative shear angle (β_0), and initiation angle (η) were all independent of cutting speed. The consistency of β_0 across all conditions indicates that it behaves very much like the primary shear angle, which is also generally independent from the same cutting parameters. As was stated earlier, the rake angle has been shown to have a heavy influence on burr formation; it is well known to directly affect the primary shear angle, so an investigation on its effect for β_0 may be of interest in a future study.

4.2 Side Burr Development

This section presents the in-situ profiles for side burrs and discusses the significance of the three cutting parameters on the side burr thickness (sb_t) and side burr height (sb_h). The profiles for sb_t are shown in Figure 4-10; they are complemented with high-resolution digital microscope images in Figure 4-11. While sb_t could easily be measured with optical microscopy, sb_h was much more difficult due to the

intermittent/inconsistent morphology of the serrations, so a trend could not be formulated. Still, sb_h is shown qualitatively via high-resolution vertical microscopic images in Figure 4-12.

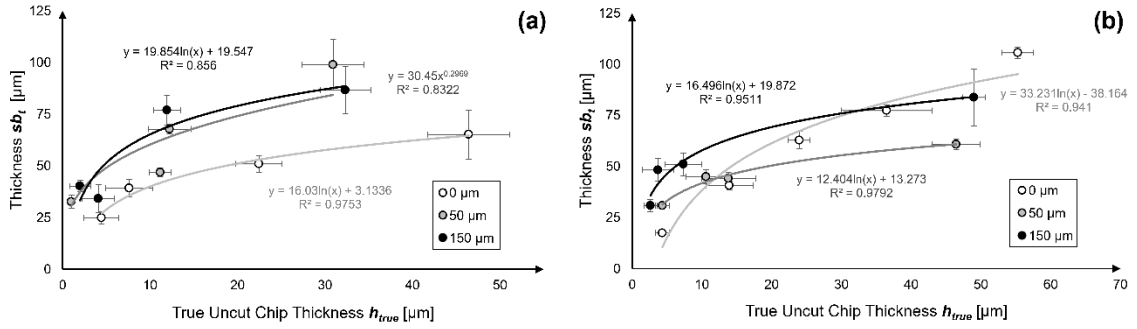


Figure 4-10. Average profiles for side burr thickness (sb_t) at (a) $v_c = 6$ m/min and (b) $v_c = 60$ m/min. Significant effect of tool-wear.

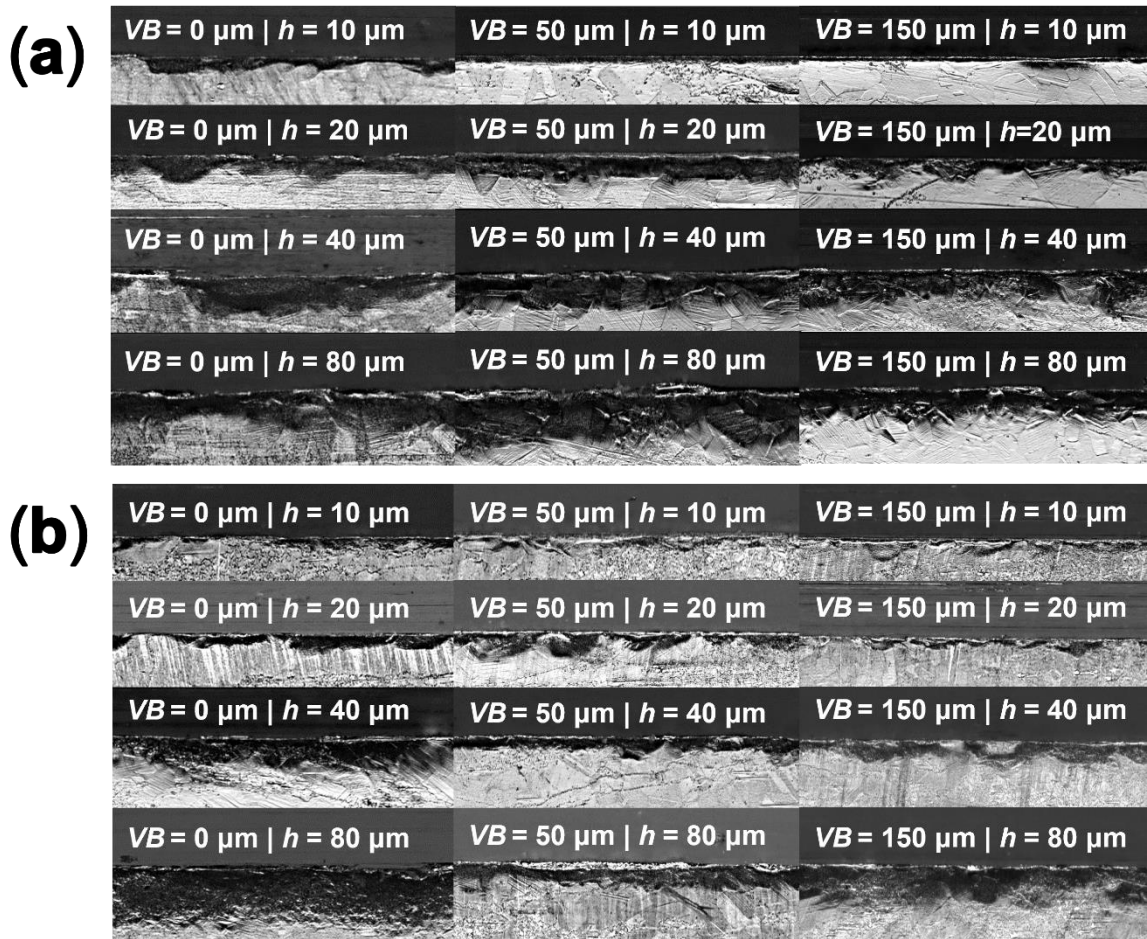


Figure 4-11. Overview of side burr thickness (sb_t) images at (a) $v_c = 6$ m/min and (b) $v_c = 60$ m/min.



Figure 4-12. Overview of side burr height (sb_h) images at (a) $v_c = 6$ m/min and (b) $v_c = 60$ m/min.

4.2.1 Effects of Uncut Chip Thickness on Side Burrs

As expected, like with exit burrs, the true uncut chip thickness (h_{true}) was the most influential factor on side burr size. From the profiles in Figure 4-10, side burr thickness (sb_t) increased with h_{true} at both cutting speeds. However, the rise was not as substantial as with exit burr thickness (b_t), so it appears that b_t may be more sensitive to h_{true} than sb_t . Moreover, the worn tools produced higher values of sb_t at low h_{true} , which is likely because of the higher compressive stress caused by the flank-wear—it has been reported that low uncut chip thickness leads to more compressive stress at the cutting area, which further causes material to bulge (and subsequently leads to more side burr formation) [109, 110]. As stated previously, sb_h could not be quantified, but from observing the vertical microscope images in Figure 4-12, sb_h does indeed seem to increase with h_{true} . Moreover, it was found that the serration frequency increased with uncut chip thickness for all the

cuts, although it was noticeably more pronounced with sharp tools. The side burr serration frequency is hypothesized to be the result of a combination of anisotropic microstructural effects (varying grains/phases) and cyclical process effects (serrated chip formation). Indeed, in-situ video of cuts with sharp tools clearly show a wavy/serrated side burr being formed due to both the cyclical chip formation mechanism, as well as the anisotropic response of differently oriented grains and other phases within the microstructure of Inconel 718 (γ' and γ'' precipitates and δ -phase particles/carbide).

4.2.2 Effects of Tool-Wear on Side Burrs

The most striking distinction between exit and side burr development is the sensitivity to tool-wear. As was seen in Figures 4-3-4-8, tool-wear had a statistically insignificant influence on exit burr parameters in most cases, but this was not the case for the side burrs. For the side burr thickness (sb_t) in Figure 4-10, the tool-wear was found to generally increase the thickness, which implies deeper plastic deformation. However, the trend was not consistent between cutting speeds. At low cutting speed, sb_t was considerably higher for the worn tools, although it was statistically identical between the two flank-wear levels. This makes sense considering VB is a measure of wear on the flank face, which lies behind the cutting-edge, so it should not have an impact on the severity of ploughing ahead of the tool (the lateral extrusion of material will be the same). Instead, it is the cutting-edge radius (r_β) that is the driving factor of the ploughing effect, of which it was comparable for the two worn tools ($r_\beta \approx 20 \mu\text{m}$ and $30 \mu\text{m}$ for $VB = 50 \mu\text{m}$ and $150 \mu\text{m}$, respectively); it was discussed previously that ploughing is the main contributor to side burr formation [97, 101]. There was a considerable difference in the tool-wear effect at high cutting speed, however. For one, the worn tools only produced a higher sb_t at low true uncut chip thickness (h_{true}), after which the sharp tool became dominant. This is likely due to the heightened stress localization and thermal softening at high uncut chip thicknesses and cutting speeds, respectively—the combination of these two effects has been shown to increase plastic deformation in the subsurface [17]. It is the opposite effect with worn tools, where thermal softening at high h_{true} decreases the ploughing effect. Additionally, the peak hydrostatic stress is larger when cutting with sharp tools because of

the localized cutting effect at the tool edge. Regardless, the high values of sb_t with worn tools at low h_{true} is due to the low uncut chip thickness to cutting-edge radius ratio, because it shifts the maximum stress distribution to the bottom of the cutting edge arc, further exacerbating lateral extrusion [98, 101, 106]. Moreover, there was statistical significance between $VB = 50 \mu\text{m}$ and $VB = 150 \mu\text{m}$ at high cutting speed, which was not the case at low cutting speed.

The side burr height (sb_h) for the worn tools at low uncut chip thickness ($h = 10 \mu\text{m}$ and $20 \mu\text{m}$) appears to be negligible if not zero—this contrasts with sb_t , which was still considerable even at low uncut chip thickness, as was shown in Figures 4-10 and 4-11. Clearly, the relative stress intensity of the hydrostatic (into the plane) stress during orthogonal cutting varies significantly with process parameters. While sb_h appeared relatively equivalent at the high cutting speed between tool conditions, the sharp tools induced taller side burrs than the worn tools at low cutting speed. This contradicts the findings of Wu et al. [101], who saw a steady rise in sb_h when increasing r_β from $5 \mu\text{m}$ to $20 \mu\text{m}$ during cutting of copper. The present work found that sb_h only decreased when going from $r_\beta \approx 5 \mu\text{m}$ to $30 \mu\text{m}$ (i.e., from a flank-wear of $0 \mu\text{m}$ to $150 \mu\text{m}$). However, important to note is that Wu et al. [101] conducted their experiments at a constant cutting speed of 300 m/min , whereas the present work saw sb_h decrease with increasing r_β at a much lower cutting speed of 6 m/min . Moreover, the difference in sb_h between cutting-edge radii dissipated at $v_c = 60 \text{ m/min}$. Thus, the observation by Wu et al. [101] may be valid for very high speeds.

4.2.3 Effects of Cutting Speed on Side Burrs

Like the exit burr thickness (b_t), the side burr thickness (sb_t) also yielded higher values at low cutting speed because of increased strain hardening due to lack of thermal softening. However, according to Muhammad et al. [102] another perspective is that higher cutting speeds will produce larger side burrs because the thermal softening facilitates easier plastic deformation. Perhaps this is the case in 3D machining, since Muhammad et al. [102] performed micro-milling on Inconel 718, whereas the present work is under 2D conditions. Additionally, they used coated WC inserts whereas this study used uncoated WC—coated

tools typically have a higher friction coefficient than uncoated tools, which means more heat is generated at the cutting interface, amplifying the thermal softening and assisting in side burr formation [102, 119]. Furthermore, future work will have to further investigate the effect of cutting speed on side burr development. The present work only employed two cutting speed settings, so testing more cutting speeds may reveal the true correlation between v_c and sb_t . It may also be helpful to study the side burr formation mechanism on less microstructurally anisotropic materials such as steel or aluminum alloys, as opposed to very anisotropic Ni-alloys like Inconel 718.

A significant difference for the side burr height (sb_h) is that the low cutting speed produced consistently larger burrs. This is not unexpected, as it is commonly known that cutting tools have more difficulty removing material at low speeds than high speeds, primarily due to a lack of thermal softening effects. For many of the low-speed cuts, especially those at high uncut chip thickness, the machined surface was found to be noticeably wavy. This effect was determined to be caused by a lack of stabilizing inertial forces at low speeds, i.e., the cutting forces were not smoothly delivered by the inertia of a fast-moving carriage accelerated prior to tool-workpiece contact (see in-situ testbed in Figure 3-1) but instead had to be delivered directly by the servo motors during the entire low speed cut without any smoothing effects of prior acceleration and associated stored kinetic energy.

5.1 Subsurface Displacement at Exit Burr Root

Using the frames of the ultra-high-speed video of the sample before and during the cut, the non-contact DIC method was used to calculate the strain in the subsurface. The steady-state vertical (v) displacement field was generated following the procedure outlined in Section 3.4 for the 24 experimental trials. The objective of this approach was to use DIC to find the subsurface displacement field at exit burr initiation, which would be when the stress/strain field is at steady state. It would be problematic to compute the displacement field during exit burr development because of the severe plastic strain occurring as the exit burr pivots about the plastic hinge. Additionally, it would be impossible to acquire a suitable reference frame from before the cut. Instead, with the initiation distance (ω) and exit burr thickness (b_t) known from Figures 4-3 and 4-6, the displacement at the burr root could easily be determined by measuring relative to the tool tip on the DIC-generated steady state displacement field. The end goal was to calculate the stress at the burr root, which is discussed in Section 5.2. Nevertheless, the vertical displacement results are plotted in Figure 5-1. As can be observed, there is much scatter, likely due to the significant uncertainty in the reference/zero displacement value within the field of view of each trial. Since the depth of the stress, and corresponding displacement field, increases with higher uncut chip thickness and tool-wear, it is expected that no true ‘zero displacement’ condition could be observed for many conditions. Thus, the large scatter in the worn tool data, as well as with increasing uncut chip thickness (h), is a direct result of the experimental limitations with respect to field of view, which had to be balanced against the frame rate based on available high-speed camera performance.

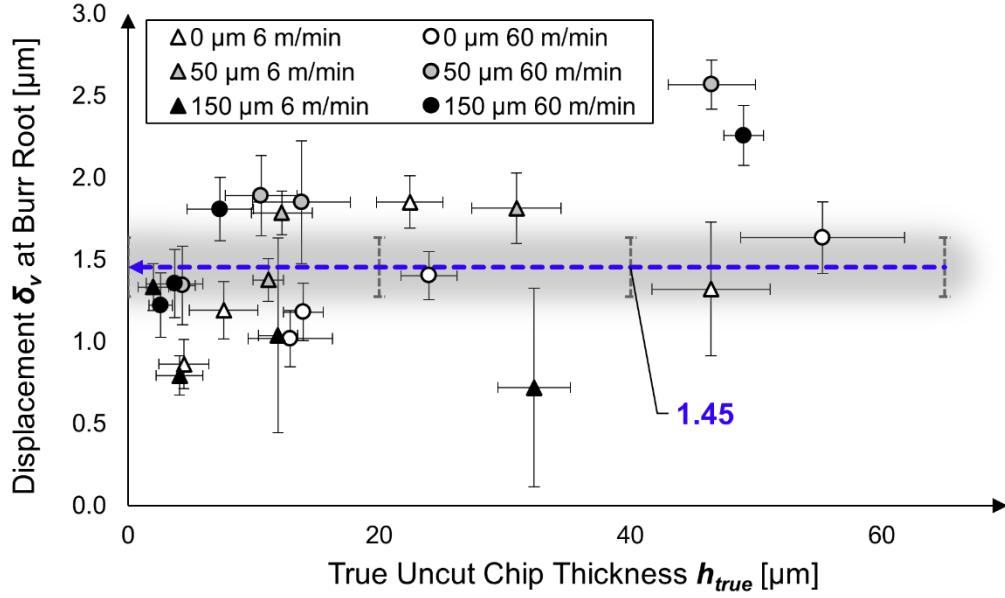


Figure 5-1. Vertical displacement (δ_v) calculated at exit burr root from DIC displacement fields.

The only other work to use DIC for modeling burr formation is Régnier et al. [96], who studied cast aluminum alloy ENAC-AlSi₇Mg0.3 with 0.5% Cu. As opposed to measuring ω , b_t , and β_0 first empirically then using those values to find the displacement at the burr root after the DIC analysis, they instead found ω and β_0 directly via DIC. Using the horizontal (u) DIC displacement field, they observed the appearance of an intense compression zone at the workpiece exit, which was characterized by a distinct contour that resembles the negative shear plane. Régnier et al. [96] believed this to be the initial negative shear angle (β_0), but this was likely one of the many variable negative shear angles (β) that are present during exit burr development, which is after initiation.

5.2 Subsurface Stress at Exit Burr Root

Following the displacement analysis in Section 5.1, further investigation was necessary for determining the state of stress at the exit burr root. The stress could not be extracted directly from the DIC displacement fields because strain is only proportional to stress within the elastic limit (i.e., Hooke's law is valid), and it is well known that both elastic and plastic strains are present during machining; modeling the loading in the plastic regime is difficult because of the nonlinearity. Thus, a semi-analytical approach utilizing

the tractional Hertzian contact model by Johnson and co-workers [120, 121] was used for calculating the stress. This approach was first invented by Platt et al. [119] for predicting machining-induced RS, and later modified by Schoop et al. [115] for use with in-situ-characterized subsurface analysis. The semi-analytical model by Schoop et al. [115] consists of using the DIC displacement fields to calibrate the contact width ($2a$) and correspondingly the half-width of contact (a) through pattern-matching with the model-generated von Mises plots. This procedure is shown in Figure 5-2.

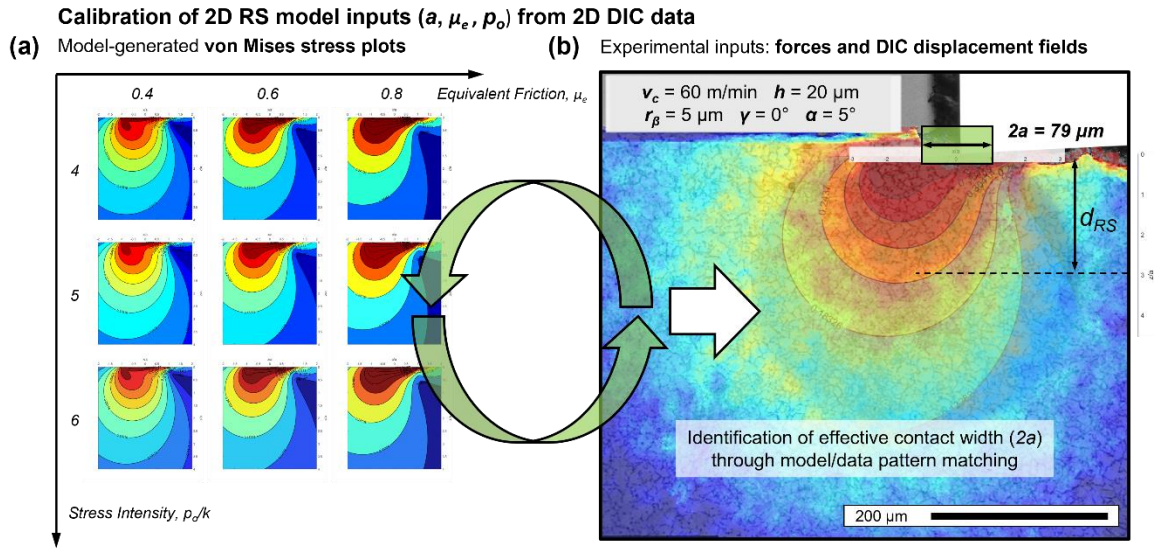


Figure 5-2. Schematic illustration of the process for calibrating contact width ($2a$): (a) modeling results of von Mises stress; (b) DIC displacement field (reproduced from [115] with permission of Springer Nature, License Number 5427980654590).

Once $2a$ and a are known, the peak normal contact pressure was calculated by Equation 1. This equation is a modified version of the default Hertzian peak contact stress (p_0) equation for a cylinder-on-plane because the latter assumes perfectly elastic and non-adhesive contact conditions, which is not realistic for machining processes. Thus, modifications were necessary to determine the ‘effective/equivalent peak Hertzian contact pressure in machining’, namely with the addition of a calibration factor, b .

$$p_0 = \frac{F_f}{wab} \quad [1]$$

where F_f is the measured feed force, w is the sample width (in this case, 3 mm), and b is the calibration factor based on experimental residual stress data determined empirically to

be 1.88 (+/- 20%, based on subsurface residual stress data). Furthermore, the normalized contact pressure ($\frac{p_0}{k}$) can be calculated by simply dividing p_0 by the flow stress of the material (k), which was given earlier as 640 MPa. Next, the model-generated von Mises stress plots were overlaid and aligned with the DIC displacement fields to find which contour intersected with the burr root, as shown in Figure 5-3. As can be seen, the burr root location changes considerably between the low and high cutting speed, but the initial negative shear angle (β_0) appears constant, as expected.

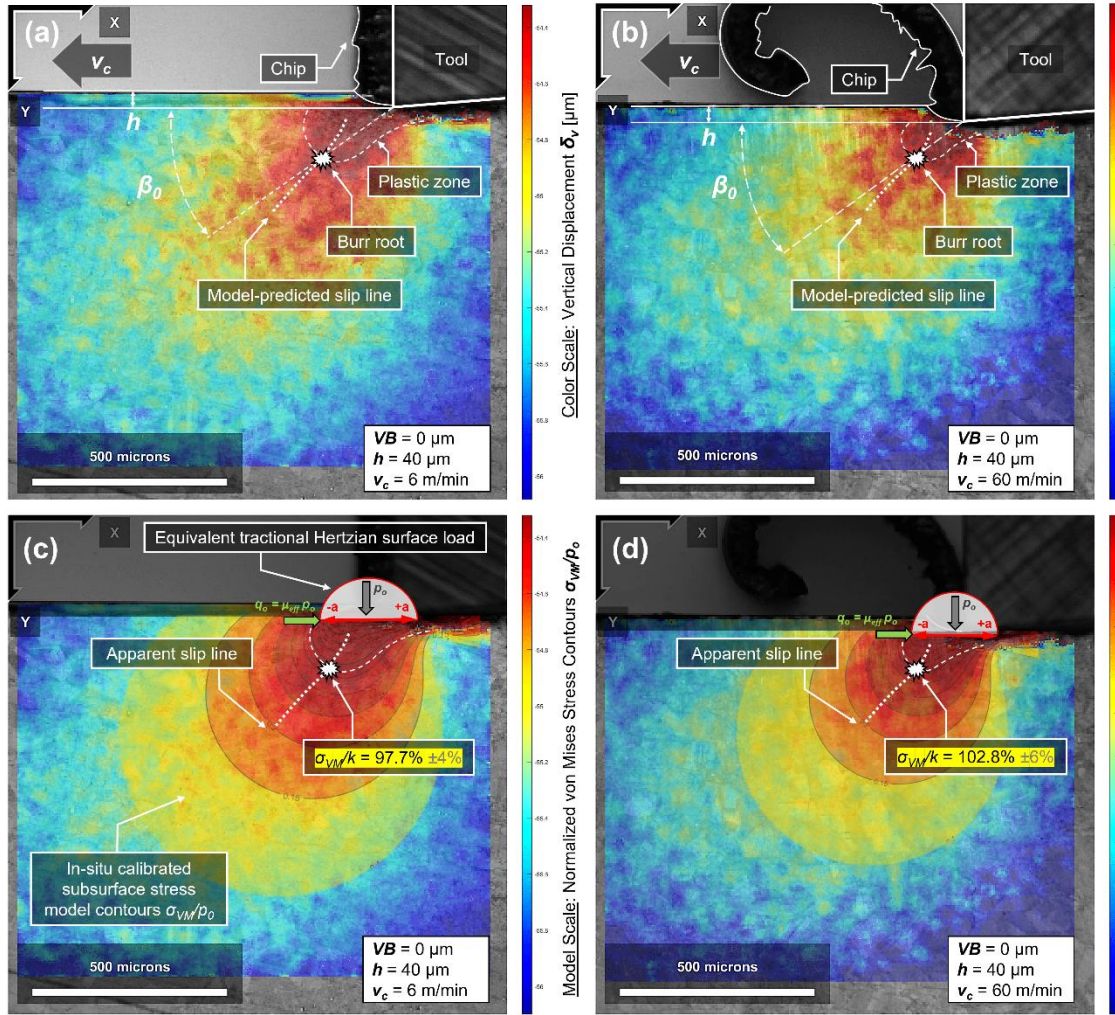


Figure 5-3. Vertical displacement field from DIC analysis overlaid on in-situ optical micrographs for (a) $v_c = 6$ m/min and (b) $v_c = 60$ m/min; Model-generated von Mises (σ_{VM}) stress fields overlaid on DIC vertical displacement fields for (c) $v_c = 6$ m/min and (d) $v_c = 60$ m/min.

The von Mises stress contours in Figures 5-3c and 5-3d signify the percentage of the flow stress at that location. Once the contour of the burr root was found, the effective normalized stress ($\frac{\sigma_{VM}}{k}$) could easily be calculated by multiplying the contour decimal with $\frac{p_0}{k}$. This process was completed for nine conditions (DIC plots of sufficient quality were required, as well as accurate force data) at the high cutting speed.

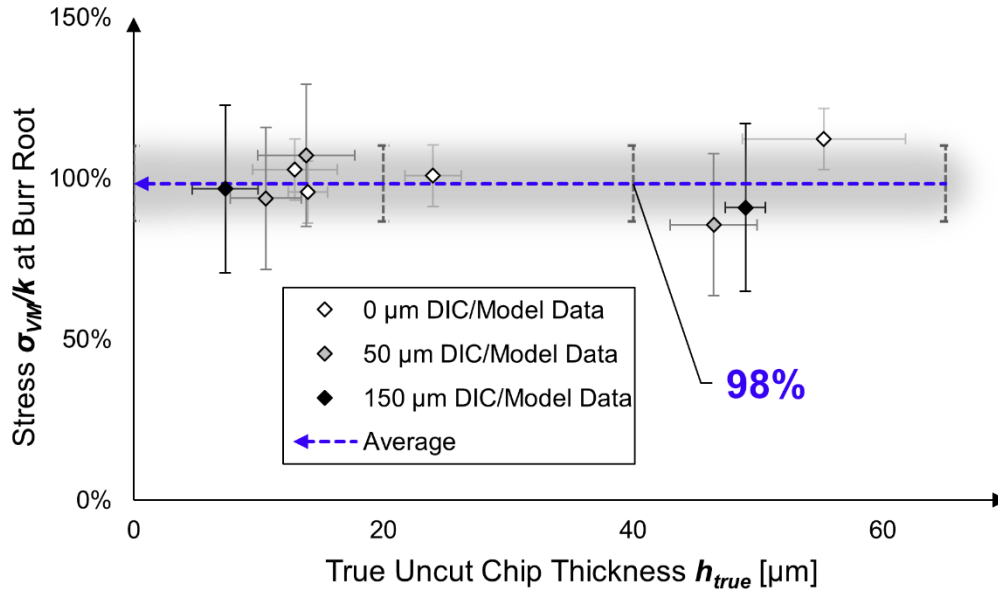


Figure 5-4. Model-analyzed normalized stress at exit burr root.

As can be observed in Figure 5-4, the average normalized stress at the exit burr root is $98\% \pm 12\%$ of the flow stress once again based on a 95% confidence interval. This finding reveals that exit burr initiation begins when the stress field contour corresponding to 100% of the flow stress intersects the vertical exit edge of the workpiece (the intersection point is the burr root). Considering that the exit burr formation process is the workpiece material undergoing SPD, it is plausible to conclude that the exit burr development begins with plastic deformation at the burr root. From this successful modeling result, it is believed that more burr parameters could be predicted by matching the measured DIC displacement fields with the analytical von Mises stress contour plots. By finding the outermost point of the stress field where the minimum stress is the flow stress, the region encapsulating plastic deformation can be determined.

Regarding the negative shear plane, it has long been thought to be straight by many researchers [79, 82, 86, 95, 122]. However, later works found that it is slightly curved with a radius R , and that negative burr fracture occurs along this convex profile, even being referred to as a ‘slip-line’, not unlike the primary shear plane and slip-line involved in chip formation [84, 93, 123, 124]. This was confirmed to be the case in the negative exit burr analysis of the present work (to be discussed in Chapter 6), where exit burr fracture always exhibited a defined curvature, as shown in Figures 6-2 and 6-4. Furthermore, it was hypothesized that the negative shear plane corresponded to the contours of the von Mises stress field. As can be seen in Figure 5-3, the burr root falls on this negative shear slip-line, which intersects the stress contours at a 90° angle. The complete shape of the slip-line could not be drawn because Saint-Venant’s principle dictates that models such as the Hertzian contact model are only valid below a depth of 20% of the half-width of contact (a). Thus, the model-predicted slip lines in Figure 5-3 do not go up to the tool tip because the profile is unknown in that domain.

One of the core objectives of the present work was to investigate the previously discussed ‘negative exit burrs’ from Section 2.3.1. As was made clear from literature review, the negative burr fracture mechanism is not yet fully understood, with authors arriving at conflicting results regarding the effects of various cutting parameters. However, this study presents strong evidence that negative burrs are a function of three different factors: (i) strain rate, (ii) the uncut chip thickness size effect, and (iii) a microstructural effect due to intergranular fracture.

6.1 Effects of Cutting Parameters on Exit Burr Fracture

The two studied cutting parameters were the cutting speed (v_c) and uncut chip thickness (h), both of which were crucial to determining the onset of negative burr fracture. The cutting speed was defined as the controlling parameter because no negative burrs were obtained at the low cutting speed with all under conditions remaining the same (same h , same VB). Thus, this solidified the strain rate being a dominant factor. Evidence also pointed to a geometric size effect because complete fracture would only occur above a certain value for true uncut chip thickness (h_{true}), indicating the existence of a critical uncut chip thickness (h_{crit}). This theory is supported by the literature, as a higher uncut chip thickness corresponds to a more tensile stress in the shear zone ahead of the tool, which facilitates fracture (i.e., less strain) much easier than the compressive stress obtained at low uncut chip thickness [93, 125]. Furthermore, negative burrs only formed at the high cutting speed of $v_c = 60$ m/min with the highest programmed uncut chip thickness of $h = 80$ μm , so the mechanism is a combination of both these factors.

However, even at the condition of $v_c = 60$ m/min and $h = 80$ μm , complete fracture did not occur at all exits: the first exit would have complete fracture (full negative burr) followed by partial fracture (mix between positive and negative burrs) on the four subsequent exits. This sequence for the sharp tool condition is illustrated in Figures 6-1 and 6-2a. Even for the first exit, where there was a full negative burr, there was still a minor positive burr at the burr root, which was also identified by Chern [81]. The h_{true} values

measured from the videos of the cuts is also displayed in the figures. As discussed before, the cutting tool would be increasingly ‘pushed out’ of the cut with each interruption, which resulted in a further reduction in h_{true} from the programmed uncut chip thickness (h). h_{true} was accurately determined based on in-situ images obtained during each cut, effectively eliminating the typically uncertain effect of compliance/deflection due to cutting forces on h_{true} .

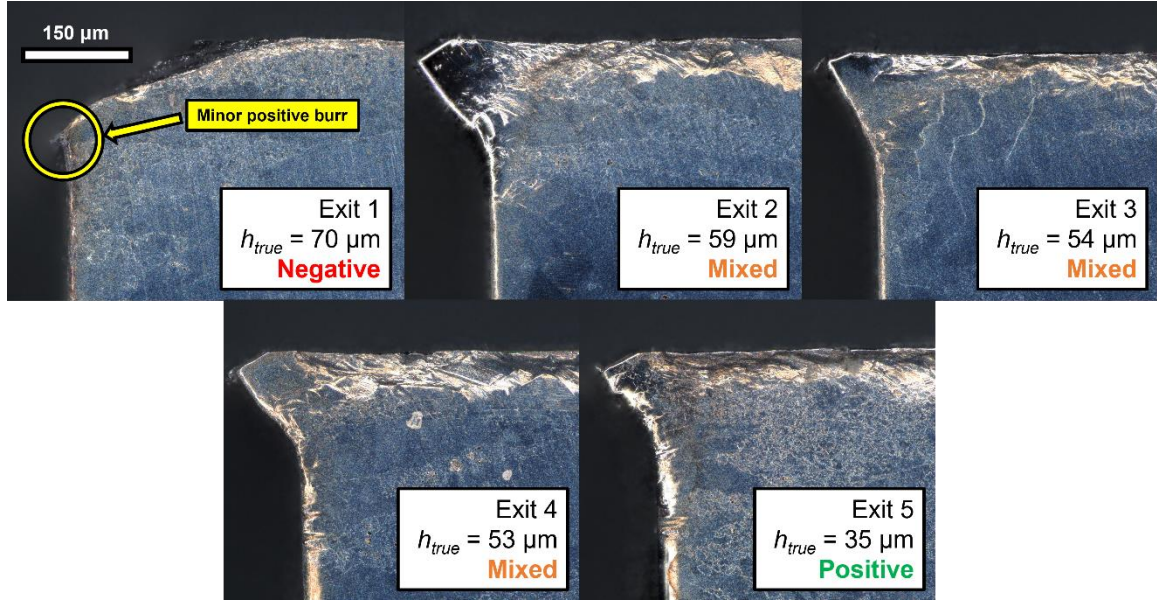


Figure 6-1. Positive to negative exit burr transition for $VB = 0 \mu\text{m}$, $h = 80 \mu\text{m}$, $v_c = 60 \text{ m/min}$.

The fact that there was not complete fracture across all exits is a particularly notable development—at $h_{true} = 70 \mu\text{m}$ (Exit 1) there was complete fracture, and the burr was fully negative, but at $h_{true} = 53\text{--}59 \mu\text{m}$ (Exits 2-4) there was only partial fracture. Finally, at $h_{true} = 35 \mu\text{m}$ (Exit 5), there was zero fracture, and the exit burr was fully positive. This can be observed from the vertical images of the exits in Figure 6-2a. Thus, it is evident that there exists a critical value between $59 \mu\text{m}$ and $70 \mu\text{m}$ for h_{true} where complete fracture occurs. The conditions for this experiment ($VB = 0 \mu\text{m}$, $h = 80 \mu\text{m}$, $v_c = 60 \text{ m/min}$) were repeated and the same pattern was observed in Figure 6-2b. As can be seen, h_{true} was considerably smaller for Exits 2-4 than Trial 1, and the transition likewise shifted to the right, resulting in a smaller partial negative burr. Additionally, there is a distinct morphology on the fractured surfaces: Chern [81] saw these same ‘elongated dimples’ in

the orthogonal machining of aluminum and copper, which he states is evidence of shear rupture.

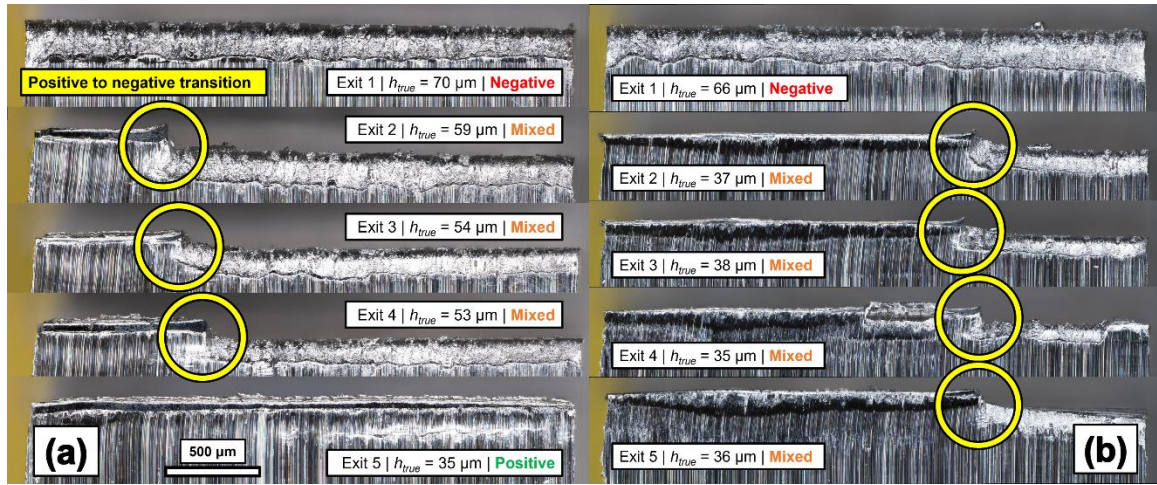


Figure 6-2. Vertical view of positive to negative exit burr transition at $VB = 0 \mu\text{m}$, $h = 80 \mu\text{m}$, $v_c = 60 \text{ m/min}$ for (a) Trial 1 and (b) Trial 2.

Additionally, Figure 6-2 shows that the point of transition along the width of the workpiece was very similar across both trials—this indicates a definite relationship between h_{true} and the fraction of positive/negative burr formation. This result was also obtained by Régnier et al. [94], which they cite as being due to microstructural effects. They also support the finding that the percentage of negative burr fracture is controlled by the uncut chip thickness. Nevertheless, the percentage of negative burr formation for each edge across both trials was calculated by measuring the corresponding fraction of the workpiece width and the results are plotted in Figure 6-3 with respect to h_{true} and exit burr thickness (b_t). As can be observed, the degree of negative burr formation with respect to both parameters exhibits a linear relationship. The regression indicates that partial fracture will occur at $h_{true} = 21 \mu\text{m}$ (x-intercept of the trend line in Figure 6-3a). After reviewing the results at the lower programmed uncut chip thicknesses (10, 20, 40 μm), this indeed seems to be the case, as none of the values for h_{true} at the lower settings were above 21 μm (apart from $h_{true} = 23.96 \mu\text{m}$ when $h = 40 \mu\text{m}$), but this is likely within the margin of error. Correspondingly, partial fracture begins when $b_t = 80 \mu\text{m}$.

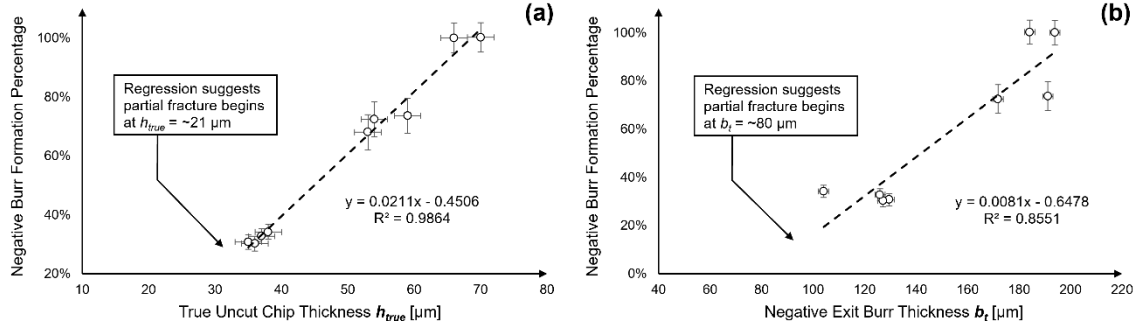


Figure 6-3. Negative burr formation development at $VB = 0$ μm, $h = 80$ μm, $v_c = 60$ m/min with (a) true uncut chip thickness (h_{true}) and (b) exit burr thickness (b_t).

6.2 Effects of Tool-Wear on Exit Burr Fracture

In addition to the strain rate (v_c) and geometric size effect (h_{true}), results showed that exit burr fracture was also a function of tool-wear (VB). The high-resolution vertical images from the digital microscope for the worn tool conditions are shown in Figure 6-4, and there is a clear distinction between the h_{crit} threshold compared to the sharp tool condition. Namely, for $VB = 50$ μm in Figure 6-4a, complete fracture occurred when h_{true} was as low as 46 μm, which is much lower than the range of complete fracture $VB = 0$ μm (66-70 μm). Partial fracture was observed for $h_{true} = 36$ μm and complete fracture was observed for $h_{true} = 44$ μm, meaning that h_{crit} is between 36-44 μm. From this observation alone, one would be inclined to think that higher tool-wear would result in a lower h_{crit} , however this outcome did not occur for $VB = 150$ μm in Figure 6-4b, where there was little to no fracture for higher values of h_{true} .

The fracture behavior for $VB = 150$ μm was very inconsistent, where there was minimal fracture for $h_{true} = 44$ μm and 50 μm on Exits 1 and 3, but zero fracture for $h_{true} = 48$ μm and 50 μm on Exits 2, 4, and 5. Additionally, the highest tool-wear setting exhibited fracture at both ends of the workpiece on Exit 1 (Figure 6-4b), as opposed to being restricted to the right side like in all other cases. Regardless, given the negligible fracture, it is evident that h_{crit} is much higher for $VB = 150$ μm than $VB = 50$ μm. This suggests that the relationship between negative burr formation and tool-wear is nonlinear, since the threshold seemed to decrease when going from $VB = 0$ μm to $VB = 50$ μm, but then increase significantly when going from $VB = 50$ μm to $VB = 150$ μm. Conducting an

in-depth analysis of the effect of tool-wear on the exit burr fracture mechanism was beyond the scope of this study, but will be of great interest in future work.

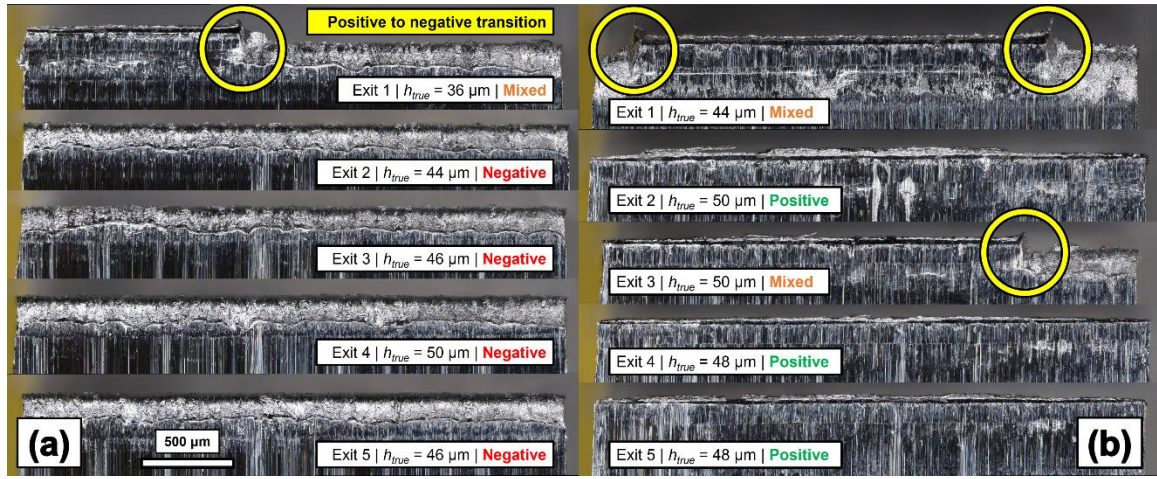


Figure 6-4. Vertical view of positive to negative exit burr transition at $h = 80 \mu\text{m}$, $v_c = 60 \text{ m/min}$ for (a) $VB = 50 \mu\text{m}$ and (b) $VB = 150 \mu\text{m}$.

6.3 Effects of Microstructure on Exit Burr Fracture

In addition to the geometric size effect of uncut chip thickness from Section 6.2, it was hypothesized that there is also a microstructural size effect. That is, exit burr fracture is due to intergranular cracking along the boundaries of the grain colonies. Complete fracture would occur whenever the exit burr thickness (b_t), which represents the depth of plastic deformation in the subsurface, is equal to the grain colony size. As was seen in Figure 3-2b, the Inconel 718 workpiece used in this study bimodal, containing both fine grains and grain colonies (i.e., clusters of larger grains). Thus, intergranular cracking was heavily anticipated to be the mode of failure because it requires much less energy to yield at the brittle grain boundaries compared to transgranular fracture, which involves penetrating the grain matrix itself. Literature has shown that crack propagation occurs along coarse slip bands for single crystals of polycrystalline materials during tensile testing, with no holes or micro-cracks [89]. Furthermore, it was first hypothesized and subsequently observed that the negative burr size (b_t) was proportional to the grain colony size (i.e., for fracture to occur, the burr would have to be equal to or larger than the grain colonies). To confirm this hypothesis, the grain colony sizes were measured across the workpiece subsurface, and the statistical distribution was calculated. Next, the cumulative

distribution was plotted alongside the negative exit burr thickness data from Figure 6-3b, as shown in in Figure 6-5.

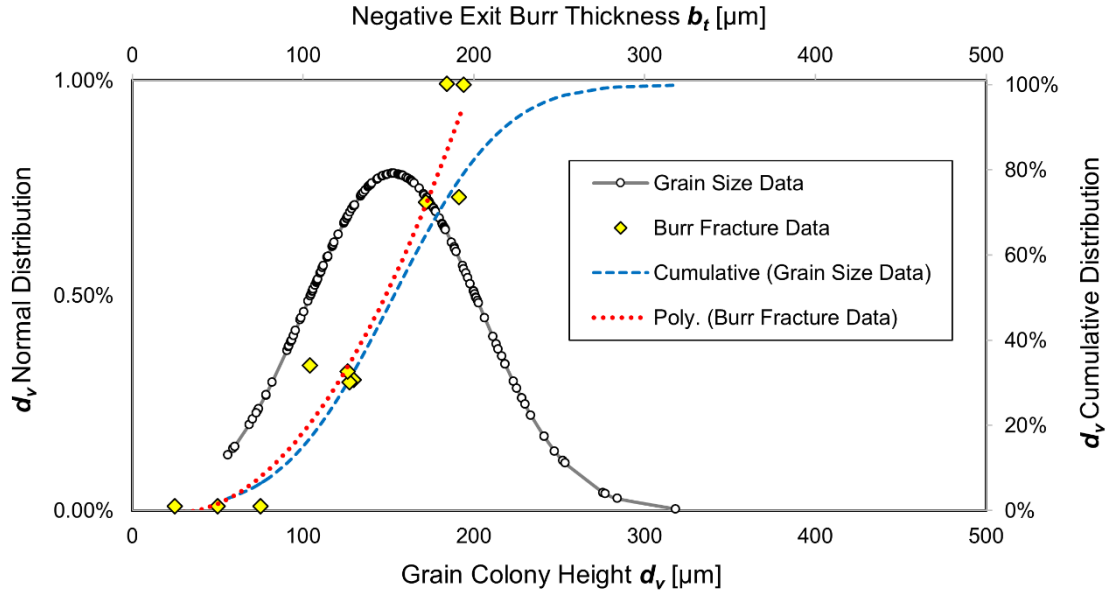


Figure 6-5. Relationship between and grain size (d_v) and negative exit burr size (b_t).

As can be observed, the cumulative fracture percentages for the exit burr thickness (b_t) and the grain colony height (d_v) closely match, so the hypothesis of a microstructural size effect between these two variables is confirmed. Moreover, this result further validates the observation by Cedergren et al. [111] that grain size affects burr formation. This correlation between the burr fracture mechanism and microstructural features of the workpiece implies that for an identical material with a different microstructure condition (e.g., an Inconel 718 sample with different grain size distribution due to differing heat treatment), there would be a different threshold for fracture to occur. A potential avenue for future work would be analyzing how the onset of negative burr fracture changes with the microstructure.

7.1 Summary of Findings

Improving the fundamental understanding and model-based approaches towards the longstanding issue of burr formation is essential for achieving more sustainable machining processes. Burrs are very harmful to many aspects of the TBL because of their implications on surface integrity and personnel health, as well as the life-cycle performance of machined products. Thus, the aim of this study was to provide physics-informed and data-driven insights on how burrs develop under different conditions with the hopes that the results will help in burr mitigation strategies. Utilizing a novel in-situ approach, the burr formation in Inconel 718 superalloy was studied at the fundamental level and several notable results were observed.

Firstly, the variation in burr geometry with respect to the cutting parameters (tool-wear, uncut chip thickness, and cutting speed) was analyzed via optical microscopy following each experiment. After performing a statistical analysis of the measured burr dimensions, the following conclusions were drawn:

- As expected, the true uncut chip thickness (h_{true}) had the largest effect on exit and side burr development. The metrics pertaining to the overall burr size, exit burr thickness and exit burr height (b_t and b_h , respectively), as well as side burr thickness and side burr height (sb_t and sb_h , respectively) all increased considerably with h_{true} . Another metric that increased with h_{true} is the exit burr initiation distance (ω), indicating that a bigger depth of cut means exit burr formation begins earlier. h_{true} had a very minor effect on the inclination angle (ψ), but the initial negative shear angle (β_0) and initiation angle (η) were independent of h_{true} .
- Tool-wear was found to have no influence on exit burr formation in most cases but a strong influence on side burr formation. For the exit burrs, tool-wear only had a significant effect on b_t at the low cutting speed, and this is hypothesized to be because of cold work and strain hardening, which are expected when machining at low speeds, and especially for worn tools. For the side burrs, tool-wear had a

significant effect on sb_t at both cutting speeds, but the difference between the flank-wear (VB) conditions varied considerably between the speeds. It is unknown why sb_t is identical between $VB = 50\text{ }\mu\text{m}$ and $150\text{ }\mu\text{m}$ at low cutting speed, but worn tools likely produce a noticeably higher sb_t because of the low uncut chip thickness to cutting-edge ratio effect. Additionally, it is hypothesized that sharp tools generate higher values of sb_t at high cutting speed because of the larger peak hydrostatic stress at the cutting-edge.

- A significant observation was made for the previously inconclusive relationship (based on comparison of the literature) between exit burr geometry and cutting speed. It was found that b_t and ω were 30% and 36% higher, respectively, at the low cutting speed, which is due to the cold work and strain hardening effects. However, the remaining metrics were all observed to be insensitive of cutting speed.

The second stage of this work involved studying the subsurface strain and stress using DIC analysis, specifically at the exit burr root location. This involved a semi-analytical approach, combining experimental DIC data with a physics-based model, and the results are as follows:

- After analyzing the DIC vertical displacement fields at the exit burr root location (using the values of b_t and ω), the average displacement was found to be $1.45\text{ }\mu\text{m} \pm 0.18\text{ }\mu\text{m}$. No trend for the displacement with respect to the cutting parameters could be extracted due to the high variability in the data.
- After finding the flow stress contour that intersects the exit burr root at initiation, a modified Hertzian contact model was used to calculate the average normalized stress at the exit burr location, which was found to be $98\% \pm 12\%$ of the flow stress of the material. Thus, exit burr development is initiated when the vertical edge of the workpiece intersects the flow stress contour.

Finally, the present work addressed the phenomenon of negative exit burrs. It was theorized that fracture was due to intergranular cracking—after analysis of the cutting conditions during fracture and the grain colony size, the following observations were made:

- Analysis of the cutting parameters supported the prior findings by other researchers that fracture is contingent upon a strain rate (cutting speed) and geometric size effect (uncut chip thickness). Strain rate was determined to be the controlling factor since no negative burrs were obtained at the low cutting speed. The geometric size effect was evident because in the case of sharp tools, fracture would only occur above a certain threshold, revealing the presence of a critical uncut chip thickness (h_{crit}) for a given cutting speed. This was revealed to be $h_{crit} = \sim 21 \text{ } \mu\text{m}$ (or $b_t = \sim 80 \text{ } \mu\text{m}$) for the sharp tool condition. Given the limitations of the study, a detailed analysis of the effects of tool-wear on negative burr development could not be conducted, but it was revealed that there was a substantial difference in the onset of fracture compared to sharp tools.
- A previously unreported condition for exit burr fracture is the microstructural size effect, which refers to intergranular cracking along the boundaries of grain colonies. The heights of the grain colonies (d_v) in the bimodal workpiece were measured and analyzed alongside the exit burr thickness (b_t) fracture data. It was shown that the trend of d_v closely matched b_t , confirming the hypothesis.

7.2 Future Work

Given that the state of academic work on burr formation is still in its infancy, there are many possible avenues for future work. Most importantly, future work should consider expanding the proposed model-based analysis and prediction of burr parameters based on DIC analysis of in-situ optical data and semi-analytical modeling. This physics-informed and data-driven approach may enable rapid prediction of relationships between process parameters and burr parameters without the need for extensive experimental testing, which could be particularly relevant in novel metallic alloys (e.g., high entropy alloys or next-generation nickel or cobalt-based turbine superalloys).

Moreover, there are many cutting parameters that were not a part of this study. Namely, the rake angle, which has been shown in prior works to have a major impact on burr formation, should be explored further. Other characteristics of the tool condition, such as the material and coatings could also be considered. The lubrication condition, cutting-

edge radius, and cutting length are all other examples of factors that could potentially have a significant effect on burr development. Moreover, determining the exact onset of exit burr fracture for different settings of strain rate, feed, microstructure, and tool-wear will be necessary for future studies on burr formation will be of great interest moving forward.

Finally, the present work studied burr formation mechanisms under 2D (orthogonal) conditions. Industrial applications of machining are typically 3D operations, meaning that for integrated computational and experimental materials engineering (ICME), future modeling efforts to translate the 2D results into 3D will be necessary. Based on recent advances in leveraging 2D in-situ data for accurate prediction of residual stresses in the 3D process of turning with nose radius tools, similar kinematic/geometric approaches are envisioned to enable translation of the present thesis work to a wide variety of different 3D machining processes.

APPENDIX

Figure A1. MATLAB script for force average calculation.

```
%% Clear Workspace
clear all
clc

%% Read Data from Folder
DIR = 'D:\Desktop\In Situ Video\Inconel 718'; % Change this for a fresh and different start
cd (DIR);
Data = load("Test10_CUT_"); %Change This
fn = fieldnames(Data);
%% Convert Timetable to Table
y = Data.Dev2_Test10_CUT; %Change this
g = timetable2table(y);

%% Conv factors
Cut_conv=2999;
Feed_conv=2996;

%% Find the two Changepoints
change_index = findchangepts(g.Dev2_ai5, 'MaxNumChanges', 10);
change_index2 = findchangepts(g.Dev2_ai4, 'MaxNumChanges', 10);

change_index(1:2:end,:)=change_index(1:2:end,:)+300;
change_index2(1:2:end,:)=change_index2(1:2:end,:)+300;
change_index(2:2:end,:)=change_index(2:2:end,:)-1000;
change_index2(2:2:end,:)=change_index2(2:2:end,:)-1000;

plot(g.Dev2_ai5);
mean(g.Dev2_ai5(change_index(end):end))
mean(g.Dev2_ai5(1:change_index(1)))

add = 1750;

%% Find the Average for Cutting Force and Feed Force Voltage Data
for i=1:9
    Cutting_Force_Avg(i) = mean(g.Dev2_ai5(change_index(i):change_index(i+1)+add));
    Friction_Force_Avg(i) = mean(g.Dev2_ai4(change_index2(i):change_index2(i+1)+add));
    Cutting_Force_Mean = mean(Cutting_Force_Avg(i));
    Friction_Force_Mean = mean(Friction_Force_Avg(i));
end

Initial_AverageC1 = mean(g.Dev2_ai5(1:change_index(1)));
Initial_AverageF1 = mean(g.Dev2_ai4(1:change_index2(1)));

Initial_AverageC2 = mean(g.Dev2_ai5(change_index(end):end));
Initial_AverageF2 = mean(g.Dev2_ai4(change_index2(end):end));

Initial_AverageC = (Initial_AverageC2-Initial_AverageC1)/2;
Initial_AverageF = (Initial_AverageF2-Initial_AverageF1)/2;
```

```

plot(g.Dev2_ai5(change_index(4):(change_index(4+1))))
plot(g.Dev2_ai5(1:change_index(2+1)+add));

for i=1:9
    %% low point and avg force for cutting force
    Avg_Force(i) = mean(g.Dev2_ai5(change_index(i):(change_index(i+1))));
    Low_Point(i) = g.Dev2_ai5(change_index(i+1)+add);

    %% low point and avg force for feed force
    FAvg_Force(i) = mean(g.Dev2_ai4(change_index(i):(change_index(i+1))));
    FLow_Point(i) = g.Dev2_ai4(change_index(i+1)+add);
end

for j=1:2:6
    %%final forces for cutting and feed force
    CA_force(j) = (Avg_Force(j)-Low_Point(j))*Cut_conv;
    FA_force(j) = (FAvg_Force(j)-FLow_Point(j))*Feed_conv;
end

%% Remove the zeros in the array
CA_force = nonzeros(CA_force);
FA_force=nonzeros(FA_force);

%% Convert Time duartion to a Double for Plot purposes
timeList = y.(y.Properties.DimensionNames{1}); % or you can simpley use TT.(name of your
time column)
% variables = y.(y.Properties.DimensionNames{2}); % or you can simpley use TT.(name of
your time column)
timsInSeconds = seconds(timeList - timeList(1));

%% Coersion form Voltage to Forces
Cutting_ForceConv = (g.Dev2_ai5*Cut_conv)-(Cut_conv*Initial_AverageC);
Friction_ForceConv = (g.Dev2_ai4*Feed_conv)-(Feed_conv*Initial_AverageF);

slot_cuttingforces=(Cutting_Force_Avg)*Cut_conv;
slot_frictionforces=(Friction_Force_Avg)*Feed_conv;

Yline_C = (mean(CA_force));
Yline_F = (mean(FA_force));
%% Data Plot Section
figure;
subplot(2,2,1)
plot(timsInSeconds, Cutting_ForceConv)
yline(Yline_C, '-.b', 'LineWidth', 3);
xlabel('Time (sec)')
ylabel('Cutting Force (N)')

subplot(2,2,2)

```

```

plot(timsInSeconds, Friction_ForceConv)
yline(Yline_F, '-.b', 'LineWidth', 3);
xlabel('Time (sec)')
ylabel('Feed Force (N)')

subplot(2,2,3)
plot(timsInSeconds(change_index(1):change_index(9)), Cutting_ForceConv(change_index(1):↙
change_index(9)))
yline(Yline_C, '-.b', 'LineWidth', 3);
xlabel('Time (sec)')
ylabel('Cutting Force (N)')

subplot(2,2,4)
plot(timsInSeconds(change_index2(1):change_index2(9)), Friction_ForceConv(change_index2↙
(1):change_index2(9)))
yline(Yline_F, '-.r', 'LineWidth', 3);
xlabel('Time (sec)')
ylabel('Feed Force (N)')

figure;
subplot(2,2,1)
plot(timsInSeconds, Cutting_ForceConv)
yline(Yline_C, '-.b', 'LineWidth', 3);
xlabel('Time (sec)')
ylabel('Cutting Force (N)')

subplot(2,2,2)
plot(timsInSeconds, Friction_ForceConv)
yline(Yline_F, '-.b', 'LineWidth', 3);
xlabel('Time (sec)')
ylabel('Feed Force (N)')

subplot(2,2,3)
plot(timsInSeconds(change_index(1):change_index(9)), Cutting_ForceConv(change_index(1):↙
change_index(9)))
yline(Yline_C, '-.b', 'LineWidth', 3);
xlabel('Time (sec)')
ylabel('Cutting Force (N)')

subplot(2,2,4)
plot(timsInSeconds(change_index2(1):change_index2(9)), Friction_ForceConv(change_index2↙
(1):change_index2(9)))
yline(Yline_F, '-.r', 'LineWidth', 3);
xlabel('Time (sec)')
ylabel('Feed Force (N)')

```

Figure A2. MATLAB script for automatic image capture using in-situ testbed vertical microscope.

```

delete(imaqfind)
% Other troubleshooting: unplugging and plugging back the top-down image acquisition tool
%   opening the image acquisition app and verifying a preview image
%   closing and opening matlab

% Verify Z-axis Focus
% Verify other image acquisitions are turned off
% tic/toc command used for verifying timing
pyenv('Version','2.7')

vid = videoinput('bitflow', 1, 'Vieworks-VC-l2MC65-E10-Freerun.r64');
src = getselectedsource(vid);

vid.FramesPerTrigger = 1;      % One image per trigger
triggerconfig(vid, 'manual');  % Not using a hardware trigger
vid.TriggerRepeat=Inf;         %continuously grab images, only save one when triggered

rosshutdown;                  % robotic system can't be initialized if it is already initialize✓
                                from a previous session
rosinit;                       % initialize robotic system to use rate-controlled for loop
r=rotrate(5.0);                % set the rate in Hz, or acquisitions / second

reset(r);                      % reset r prior to loop execution
start(vid);

pause(1);                      % Pausing in case triggering too fast after starting causes errors

display("Starting");
% You may need to increase the number of captures to a larger value (the number, and
% then delete excess ones - edit the for loop parameters

for i = 1:85
    trigger(vid);
    fname = sprintf("D:\\Desktop\\In Situ Video\\Inconel 718\\image_%d.tiff", i);
    m = getdata(vid); %acquire image
    imwrite(m, fname); %write file
    fprintf("Capture %d\\n", i);
    waitfor(r); % wait until the loop time to
end
stop(vid);

delete(imaqfind)
delete(vid)
clear
close(gcf)
display("Completed")

```

REFERENCES

- [1] Jayal, A.D., Badurdeen, F., Dillon Jr., O.W., Jawahir, I.S. (2010) Sustainable manufacturing: Modeling and optimization challenges at the product, process and system levels. *CIRP Journal of Manufacturing Science and Technology*, 2(3), pp. 144-152.
- [2] De Bartolomeis, A., Newman, S.T., Jawahir, I.S., Biermann, D., Shokrani, A. (2021) Future research directions in the machining of Inconel 718. *Journal of Materials Processing Technology*, 297, pp. 117260.
- [3] Gillespie, L.K. (1999) *Deburring and Edge Finishing Handbook*, Society of Manufacturing Engineers, Dearborn, Michigan.
- [4] Dornfeld, D., Min, S. (2009) A Review of Burr Formation in Machining. In: Aurich, J.C., Dornfeld, D. (Eds.) *Burrs - Analysis, Control and Removal*, Proceedings of the CIRP International Conference on Burrs, Kaiserslautern, Germany, pp. 3-11.
- [5] Jin, S.Y., Pramanik, A., Basak, A.K., Prakash, C., Shankar, S., Debnath, S. (2020) Burr formation and its treatments—a review. *The International Journal of Advanced Manufacturing Technology*, 107(5), pp. 2189-2210.
- [6] Jawahir, I.S., Schoop, J., Kaynak, Y., Balaji, A.K., Ghosh, R., Lu, T. (2020) Progress Toward Modeling and Optimization of Sustainable Machining Processes. *Journal of Manufacturing Science and Engineering*, 142(11).
- [7] Wanigarathne, P.C., Liew, J., Wang, X., Dillon Jr., O.W., Jawahir, I.S. (2004) Assessment of Process Sustainability for Product Manufacture in Machining Operations. In: Proceedings of the 2nd Global Conference on Sustainable Product Development and Life Cycle Engineering, Berlin, Germany, pp. 305-312.
- [8] Niknam, S.A., Zedan, Y., Songmene, V. (2014) Machining Burrs Formation & Deburring of Aluminium Alloys. In: Monteiro, W.A. (Eds.) *Light Metal Alloys Applications*. InTech, Rijeka, Croatia, pp. 99-122.
- [9] Biermann, D., Heilmann, M. (2009) Burr Minimization Strategies in Machining Operations. In: Aurich, J.C., Dornfeld, D. (Eds.) *Burrs - Analysis, Control and Removal*, Proceedings of the CIRP International Conference on Burrs, Kaiserslautern, Germany, pp. 13-20.

- [10] Kim, J., Min, S., Dornfeld, D.A. (2001) Optimization and control of drilling burr formation of AISI 304L and AISI 4118 based on drilling burr control charts. *International Journal of Machine Tools and Manufacture*, 41(7), pp. 923-936.
- [11] Aurich, J.C., Dornfeld, D., Arrazola, P.J., Franke, V., Leitz, L., Min, S. (2009) Burrs—Analysis, control and removal. *CIRP Annals*, 58(2), pp. 519-542.
- [12] Thomas, A., El-Wahabi, M., Cabrera, J.M., Prado, J.M. (2006) High temperature deformation of Inconel 718. *Journal of Materials Processing Technology*, 177(1-3), pp. 469-472.
- [13] Knorovsky, G.A., Cieslak, M.J., Headley, T.J., Romig, A.D., Hammetter, W.F. (1989) INCONEL 718: A Solidification Diagram. *Metallurgical Transactions A*, 20(10), pp. 2149-2158.
- [14] Umbrello, D. (2013) Investigation of surface integrity in dry machining of Inconel 718. *The International Journal of Advanced Manufacturing Technology*, 69(9), pp. 2183-2190.
- [15] Yin, Q., Liu, Z., Wang, B., Song, Q., Cai, Y. (2020) Recent progress of machinability and surface integrity for mechanical machining Inconel 718: a review. *The International Journal of Advanced Manufacturing Technology*, 109, pp. 215-245.
- [16] Akhtar, W., Sun, J., Sun, P., Chen, W., Saleem, Z. (2014) Tool wear mechanisms in the machining of Nickel based super-alloys: A review. *Frontiers of Mechanical Engineering*, 9(2), pp. 106-119.
- [17] Liao, Z., la Monaca, A., Murray, J., Speidel, A., Ushmaev, D., Clare, A., Axinte, D., M'Saoubi, R. (2021) Surface integrity in metal machining - Part I: Fundamentals of surface characteristics and formation mechanisms. *International Journal of Machine Tools and Manufacture*, 162, pp. 103687.
- [18] la Monaca, A., Murray, J.W., Liao, Z., Speidel, A., Robles-Linares, J.A., Axinte, D.A., Hardy, M.C., Clare, A.T. (2021) Surface integrity in metal machining - Part II: Functional performance. *International Journal of Machine Tools and Manufacture*, 164, pp. 103718.
- [19] Thakur, D.G., Ramamoorthy, B., Vijayaraghavan, L. (2009) Study on the machinability characteristics of superalloy Inconel 718 during high speed turning. *Materials & Design*, 30(5), pp. 1718-1725.

- [20] Bushlya, V., Zhou, J., Ståhl, J.-E. (2012) Effect of Cutting Conditions on Machinability of Superalloy Inconel 718 During High Speed Turning with Coated and Uncoated PCBN Tools. *Procedia CIRP*, 3, pp. 370-375.
- [21] Musfirah, A.H., Ghani, J.A., Haron, C.H.C. (2017) Tool wear and surface integrity of inconel 718 in dry and cryogenic coolant at high cutting speed. *Wear*, 376-377, Part A, pp. 125-133.
- [22] Kaynak, Y., Karaca, H.E., Noebe, R.D., Jawahir, I.S. (2013) Analysis of Tool-wear and Cutting Force Components in Dry, Preheated, and Cryogenic Machining of *NiTi* Shape Memory Alloys. *Procedia CIRP*, 8, pp. 498-503.
- [23] Hatt, O., Crawforth, P., Jackson, M. (2017) On the mechanism of tool crater wear during titanium alloy machining. *Wear*, 374, pp. 15-20.
- [24] Rakesh, M., Datta, S. (2019) Effects of Cutting Speed on Chip Characteristics and Tool Wear Mechanisms During Dry Machining of Inconel 718 Using Uncoated WC Tool. *Arabian Journal for Science and Engineering*, 44(9), pp. 7423-7440.
- [25] Khan, S.A., Soo, S.L., Aspinwall, D.K., Sage, C., Harden, P., Fleming, M., White, A., M'Saoubi, R. (2012) Tool wear/life evaluation when finish turning Inconel 718 using PCBN tooling. *Procedia CIRP*, 1, pp. 283-288.
- [26] Hao, Z., Fan, Y., Lin, J., Ji, F., Liu, X. (2017) New observations on wear mechanism of self-reinforced SiAlON ceramic tool in milling of Inconel 718. *Archives of Civil and Mechanical Engineering*, 17(3), pp. 467-474.
- [27] Parida, A.K., Maity, K. (2017) Effect of nose radius on forces, and process parameters in hot machining of Inconel 718 using finite element analysis. *Engineering Science and Technology, an International Journal*, 20(2), pp. 687-693.
- [28] Devillez, A., Le Coz, G., Dominiak, S., Dudzinski, D. (2011) Dry machining of Inconel 718, workpiece surface integrity. *Journal of Materials Processing Technology*, 211(10), pp. 1590-1598.
- [29] Parida, A.K. (2019) Analysis of Chip Geometry in Hot Machining of Inconel 718 Alloy. *Iranian Journal of Science and Technology, Transactions of Mechanical Engineering*, 43(1), pp. 155-164.
- [30] Gupta, M.K., Mia, M., Pruncu, C.I., Kapłonek, W., Nadolny, K., Patra, K., Mikolajczyk, T., Pimenov, D.Y., Sarikaya, M., Sharma, V.S. (2019) Parametric optimization and process capability analysis for machining of nickel-based

superalloy. The International Journal of Advanced Manufacturing Technology, 102(9), pp. 3995-4009.

- [31] Sharman, A.R.C., Hughes, J.I., Ridgway, K. (2015) The effect of tool nose radius on surface integrity and residual stresses when turning Inconel 718™. Journal of Materials Processing Technology, 216, pp. 123-132.
- [32] Bai, W., Bisht, A., Roy, A., Suwas, S., Sun, R., Silberschmidt, V.V. (2019) Improvements of machinability of aerospace-grade Inconel alloys with ultrasonically assisted hybrid machining. The International Journal of Advanced Manufacturing Technology, 101(5), pp. 1143-1156.
- [33] Dudzinski, D., Devillez, A., Moufki, A., Larrouquère, D., Zerrouki, V., Vigneau, J. (2004) A review of developments towards dry and high speed machining of Inconel 718 alloy. International Journal of Machine Tools and Manufacture, 44(4), pp. 439-456.
- [34] Prengel, H.G., Jindal, P.C., Wendt, K.H., Santhanam, A.T., Hegde, P.L., Penich, R.M. (2001) A new class of high performance PVD coatings for carbide cutting tools. Surface and Coatings Technology, 139(1), pp. 25-34.
- [35] Jeyapandiarajan, P., Xavier, M.A. (2019) Influence of cutting condition on machinability aspects of Inconel 718. Journal of Engineering Research, 7(2).
- [36] Arunachalam, R., Mannan, M., Spowage, A. (2004) Surface integrity when machining age hardened Inconel 718 with coated carbide cutting tools. International Journal of Machine Tools and Manufacture, 44(14), pp. 1481-1491.
- [37] Zhou, J., Bushlya, V., Peng, R.L., Chen, Z., Johansson, S., Stahl, J.E. (2014) Analysis of Subsurface Microstructure and Residual Stresses in Machined Inconel 718 with PCBN and Al₂O₃-SiCw Tools. Procedia CIRP, 13, pp. 150-155.
- [38] Holmberg, J., Wretland, A., Berglund, J., Beno, T. (2020) A detailed investigation of residual stresses after milling Inconel 718 using typical production parameters for assessment of affected depth. Materials Today Communications, 24, pp. 100958.
- [39] D'addona, D., Raykar, S.J., Narke, M. (2017) High speed machining of Inconel 718: tool wear and surface roughness analysis. Procedia CIRP, 62, pp. 269-274.
- [40] Altin, A., Nalbant, M., Taskesen, A. (2007) The effects of cutting speed on tool wear and tool life when machining Inconel 718 with ceramic tools. Materials & Design, 28(9), pp. 2518-2522.

- [41] Sharman, A.R.C., Hughes, J.I., Ridgway, K. (2004) Workpiece Surface Integrity and Tool Life Issues When Turning Inconel 718™ Nickel Based Superalloy. *Machining Science and Technology*, 8(3), pp. 399-414.
- [42] Rahman, M., Seah, W.K.H., Teo, T.T. (1997) The machinability of inconel 718. *Journal of Materials Processing Technology*, 63(1-3), pp. 199-204.
- [43] Narutaki, N., Yamane, Y., Hayashi, K., Kitagawa, T., Uehara, K. (1993) High-Speed Machining of Inconel 718 with Ceramic Tools. *CIRP Annals*, 42(1), pp. 103-106.
- [44] Li, H.Z., Zeng, H., Chen, X.Q. (2006) An experimental study of tool wear and cutting force variation in the end milling of Inconel 718 with coated carbide inserts. *Journal of Materials Processing Technology*, 180(1-3), pp. 296-304.
- [45] Hadi, M.A., Ghani, J.A., Haron, C.H.C., Kasim, M.S. (2013) Comparison between Up-milling and down-milling operations on tool wear in milling Inconel 718. *Procedia Engineering*, 68, pp. 647-653.
- [46] Jiwang, Y. (2009) Applications of Nano and Micromachining in Industry. In: Paulo Davim, J., Jackson, M.J. (Eds.) *Nano and Micromachining*. ISTE Ltd., London, United Kingdom, pp. 175-207.
- [47] Çelik, Y.H., Kilickap, E., Güney, M. (2017) Investigation of cutting parameters affecting on tool wear and surface roughness in dry turning of Ti-6Al-4V using CVD and PVD coated tools. *Journal of the Brazilian Society of Mechanical Sciences and Engineering*, 39(6), pp. 2085-2093.
- [48] Nalbant, M., Altın, A., Gökkaya, H. (2007) The effect of coating material and geometry of cutting tool and cutting speed on machinability properties of Inconel 718 super alloys. *Materials & Design*, 28(5), pp. 1719-1724.
- [49] Lu, X., Jia, Z., Wang, H., Si, L., Wang, X. (2016) Surface roughness prediction model of micro-milling Inconel 718 with consideration of tool wear. *International Journal of Nanomanufacturing*, 12(1), pp. 93-108.
- [50] Jin, D., Liu, Z., Yi, W., Su, G. (2011) Influence of cutting speed on surface integrity for powder metallurgy nickel-based superalloy FGH95. *The International Journal of Advanced Manufacturing Technology*, 56(5-8), pp. 553-559.
- [51] Pawade, R.S., Joshi, S.S., Brahmankar, P.K., Rahman, M. (2007) An investigation of cutting forces and surface damage in high-speed turning of Inconel 718. *Journal of Materials Processing Technology*, 192-193, pp. 139-146.

- [52] Sadat, A.B. (1987) Surface region damage of machined inconel-718 nickel-base superalloy using natural and controlled contact length tools. *Wear*, 119(2), pp. 225-235.
- [53] Wang, X., Huang, C., Zou, B., Liu, G., Zhu, H., Wang, J. (2018) Experimental study of surface integrity and fatigue life in the face milling of Inconel 718. *Frontiers of Mechanical Engineering*, 13(2), pp. 243-250.
- [54] Jacobson, M., Dahlman, P., Gunnberg, F. (2002) Cutting speed influence on surface integrity of hard turned bainite steel. *Journal of Materials Processing Technology*, 128(1-3), pp. 318-323.
- [55] Baek, D.K., Ko, T.J., Kim, H.S. (2001) Optimization of feedrate in a face milling operation using a surface roughness model. *International Journal of Machine Tools and Manufacture*, 41(3), pp. 451-462.
- [56] Gürgen, S., Tali, D., Kushan, M.C. (2019) An Investigation on Surface Roughness and Tool Wear in Turning Operation of Inconel 718. *Journal of Aerospace Technology and Management*, 11.
- [57] Xuan-Truong, D., Minh-Duc, T. (2013) EFFECT OF CUTTING CONDITION ON TOOL WEAR AND SURFACE ROUGHNESS DURING MACHINING OF INCONEL 718. *International Journal of Advanced Engineering Technology*, 108, pp. 112.
- [58] Schoop, J., Sales, W.F., Jawahir, I.S. (2017) High speed cryogenic finish machining of Ti-6Al4V with polycrystalline diamond tools. *Journal of Materials Processing Technology*, 250, pp. 1-8.
- [59] Damir, A., Shi, B., Attia, M.H. (2019) Flow characteristics of optimized hybrid cryogenic-minimum quantity lubrication cooling in machining of aerospace materials. *CIRP Annals*, 68(1), pp. 77-80.
- [60] Bagherzadeh, A., Budak, E. (2018) Investigation of machinability in turning of difficult-to-cut materials using a new cryogenic cooling approach. *Tribology International*, 119, pp. 510-520.
- [61] Subhas, B.K., Bhat, R., Ramachandra, K., Balakrishna, H.K. (2000) Simultaneous Optimization of Machining Parameters for Dimensional Instability Control in Aero Gas Turbine Components Made of Inconel 718 Alloy. *Journal of Manufacturing Science and Engineering*, 122(3), pp. 586-590.

- [62] Pawade, R.S., Joshi, S.S., Brahmkar, P.K. (2008) Effect of machining parameters and cutting edge geometry on surface integrity of high-speed turned Inconel 718. *International Journal of Machine Tools and Manufacture*, 48(1), pp. 15-28.
- [63] Sharman, A.R.C., Hughes, J.I., Ridgway, K. (2006) An analysis of the residual stresses generated in Inconel 718™ when turning. *Journal of Materials Processing Technology*, 173(3), pp. 359-367.
- [64] Pusavec, F., Hamdi, H., Kopac, J., Jawahir, I.S. (2011) Surface integrity in cryogenic machining of nickel based alloy—Inconel 718. *Journal of Materials Processing Technology*, 211(4), pp. 773-783.
- [65] Schlauer, C., Peng, R.L., Odén, M. (2002) Residual Stresses in a Nickel-based Superalloy Introduced by Turning. *Materials Science Forum*, 404-407, pp. 173-178.
- [66] Wang, J., Zhang, D., Wu, B., Luo, M. (2017) Residual Stresses Analysis in Ball end Milling of Nickel-Based Superalloy Inconel 718. *Materials Research*, 20(6), pp. 1681-1689.
- [67] Sharman, A., Dewes, R.C., Aspinwall, D.K. (2001) Tool life when high speed ball nose end milling Inconel 718™. *Journal of Materials Processing Technology*, 118(1-3), pp. 29-35.
- [68] Hua, Y., Liu, Z. (2018) Experimental Investigation of Principal Residual Stress and Fatigue Performance for Turned Nickel-Based Superalloy Inconel 718. *Materials*, 11(6), pp. 879.
- [69] Spanos, G., Reynolds, W.T. (2014) Microstructure of Metals and Alloys. In: Laughlin, D.E., Hono, K. (Eds.) *Physical Metallurgy*. Elsevier, pp. 1073-1112.
- [70] Ren, X.-p., Liu, Z.-q. (2018) Microstructure refinement and work hardening in a machined surface layer induced by turning Inconel 718 super alloy. *International Journal of Minerals, Metallurgy, and Materials*, 25(8), pp. 937-949.
- [71] Toker, G.P., Schoop, J., Karaca, H. (2022) Machining-induced surface integrity and nanocrystalline surface layers in cryogenic finishing turning of Inconel 718. *Machining Science and Technology*, pp. 1-25.
- [72] Zhou, J.M., Bushlya, V., Peng, R.L., Johansson, S., Avdovic, P., Stahl, J.-E. (2011) Effects of Tool Wear on Subsurface Deformation of Nickel-Based Superalloy. *Procedia Engineering*, 19, pp. 407-413.

- [73] Imran, M., Mativenga, P.T., Gholinia, A., Withers, P.J. (2015) Assessment of surface integrity of Ni superalloy after electrical-discharge, laser and mechanical micro-drilling processes. *The International Journal of Advanced Manufacturing Technology*, 79(5), pp. 1303-1311.
- [74] Jin, D., Liu, Z. (2012) Effect of cutting speed on surface integrity and chip morphology in high-speed machining of PM nickel-based superalloy FGH95. *The International Journal of Advanced Manufacturing Technology*, 60(9-12), pp. 893-899.
- [75] Cai, X., Qin, S., Li, J., An, Q., Chen, M. (2014) EXPERIMENTAL INVESTIGATION ON SURFACE INTEGRITY OF END MILLING NICKEL-BASED ALLOY—*INCONEL 718*. *Machining Science and Technology*, 18(1), pp. 31-46.
- [76] Ji, H., Gupta, M.K., Song, Q., Cai, W., Zheng, T., Zhao, Y., Liu, Z., Pimenov, D.Y. (2021) Microstructure and machinability evaluation in micro milling of selective laser melted Inconel 718 alloy. *Journal of Materials Research and Technology*, 14, pp. 348-362.
- [77] Poór, D.I., Geier, N., Pereszlai, C., Xu, J. (2021) A critical review of the drilling of CFRP composites: Burr formation, characterisation and challenges. *Composites Part B: Engineering*, 223, pp. 109155.
- [78] Leopold, J., Wohlgemuth, R. (2009) Modeling and Simulation of Burr Formation: State-of-the-Art and Future Trends. In: Aurich, J.C., Dornfeld, D. (Eds.) *Burrs - Analysis, Control and Removal*, Proceedings of the CIRP International Conference on Burrs, Kaiserslautern, Germany, pp. 79-86.
- [79] Gillespie, L.K. (1973) *The Formation and Properties of Machining Burrs*. MS Thesis, Utah State University.
- [80] Nisbet, T.S., Mullett, G.W. (1978) *Rolling Bearings in Service ; Interpretation of Types of Damage*, Hutchinson.
- [81] Chern, G.-L. (2006) Study on mechanisms of burr formation and edge breakout near the exit of orthogonal cutting. *Journal of Materials Processing Technology*, 176(1-3), pp. 152-157.
- [82] Ko, S.-L., Dornfeld, D.A. (1991) A Study on Burr Formation Mechanism. *Journal of Engineering Materials and Technology*, 113(1), pp. 75-87.
- [83] Pekelharing, A.J. (1983) The exit failure in interrupted cutting. *CIRP Annals*, 27(1).

- [84] Iwata, K., Ueda, K., Okuda, K. (1982) Study of Mechanism of Burrs Formation in Cutting Based on Direct SEM Observation. *Journal of the Japan Society for Precision Engineering*, 48(4), pp. 510-515.
- [85] Sung-Lim, K., Dornfeld, D.A. (1996) Analysis of fracture in burr formation at the exit stage of metal cutting. *Journal of Materials Processing Technology*, 58(2-3), pp. 189-200.
- [86] Chern, G.-L., Dornfeld, D.A. (1996) Burr/Breakout Model Development and Experimental Verification. *Journal of Engineering Materials and Technology*, 118(2), pp. 201-206.
- [87] Schäfer, F., Breuninger, F., Sauer, H., Schuh, B., Seyderhelm, W., Winter, H.J., Warnecke, H.J., Brauner, H.U. (1975) Deburring: theory, processes, systems. Krausskopf,
- [88] Hashimura, M., Chang, Y.P., Dornfeld, D. (1999) Analysis of Burr Formation Mechanism in Orthogonal Cutting. *Journal of Manufacturing Science and Engineering*, 121(1), pp. 1-7.
- [89] Beevers, C.J., Honeycombe, R.W.K. (1962) The initiation of ductile fracture in pure metals. *Philosophical Magazine*, 7(77), pp. 763-773.
- [90] Puttick, K.E. (1959) Ductile fracture in metals. *Philosophical Magazine*, 4(44), pp. 964-969.
- [91] Kim, J., Dornfeld, D.A. (2002) Development of an Analytical Model for Drilling Burr Formation in Ductile Materials. *Journal of Engineering Materials and Technology*, 124(2), pp. 192-198.
- [92] Ahn, J., Lim, H. (1997) Side Burr Generation Model in Micro-Grooving. In: *Proceedings of the 12th Annual Meeting of the American Society for Precision Engineering*, Raleigh, NC, pp. 215-219.
- [93] Régnier, T., Fromentin, G., Marcon, B., Outeiro, J., D'Acunto, A., Crolet, A., Grunder, T. (2018) Fundamental study of exit burr formation mechanisms during orthogonal cutting of AlSi aluminium alloy. *Journal of Materials Processing Technology*, 257, pp. 112-122.
- [94] Régnier, T., Fromentin, G., D'Acunto, A., Outeiro, J., Marcon, B., Crolet, A. (2018) Phenomenological Study of Multivariable Effects on Exit Burr Criteria During Orthogonal Cutting of AlSi Alloys Using Principal Components Analysis. *Journal of Manufacturing Science and Engineering*, 140(10), pp. 101006.

- [95] Nakayama, K., Arai, M. (1987) Burr Formation in Metal Cutting. *CIRP Annals*, 36(1), pp. 33-36.
- [96] Régnier, T., Marcon, B., Outeiro, J., Fromentin, G., D'Acunto, A., Crolet, A. (2019) Investigations on exit burr formation mechanisms based on digital image correlation and numerical modeling. *Machining Science and Technology*, 23(6), pp. 925-950.
- [97] Aslantas, K., Çiçek, A. (2018) The effects of cooling/lubrication techniques on cutting performance in micro-milling of Inconel 718 superalloy. *Procedia CIRP*, 77, pp. 70-73.
- [98] Wang, G.C., Zhang, C.Y. (2004) Study on the Forming Mechanism of the Cutting-direction Burr in Metal Cutting. *Key Engineering Materials*, 259-260, pp. 868.
- [99] Avila, M.C., Dornfeld, D.A. (2004) On the face milling burr formation mechanisms and minimization strategies at high tool engagement. University of California, Berkeley.
- [100] Lee, K., Dornfeld, D.A. (2005) Micro-burr formation and minimization through process control. *Precision Engineering*, 29(2), pp. 246-252.
- [101] Wu, X., Li, L., He, N. (2017) Investigation on the burr formation mechanism in micro cutting. *Precision Engineering*, 47, pp. 191-196.
- [102] Muhammad, A., Gupta, M.K., Mikołajczyk, T., Pimenov, D.Y., Giasin, K. (2021) Effect of Tool Coating and Cutting Parameters on Surface Roughness and Burr Formation during Micromilling of Inconel 718. *Metals*, 11(1), pp. 167.
- [103] Geier, N., Davim, J.P., Szalay, T. (2019) Advanced cutting tools and technologies for drilling carbon fibre reinforced polymer (CFRP) composites: A review. *Composites Part A: Applied Science and Manufacturing*, 125, pp. 105552.
- [104] Dornfeld, D.A., Kim, J.S., Dechow, H., Hewson, J., Chen, L.J. (1999) Drilling Burr Formation in Titanium Alloy, Ti-6Al-4V. *CIRP Annals*, 48(1), pp. 73-76.
- [105] Wang, G.C., Zhang, C.Y. (2004) Mechanism of Burr Formation in Milling. *Key Engineering Materials*, 259-260, pp. 278-281.
- [106] Bissacco, G., Hansen, H.N., Chiffre, L.D. (2005) Micromilling of hardened tool steel for mould making applications. *Journal of Materials Processing Technology*, 167(2-3), pp. 201-207.

- [107] Pilný, L., De Chiffre, L., Piška, M., Villumsen, M.F. (2012) Hole quality and burr reduction in drilling aluminium sheets. *CIRP Journal of Manufacturing Science and Technology*, 5(2), pp. 102-107.
- [108] Biermann, D., Hartmann, H. (2012) Reduction of Burr Formation in Drilling Using Cryogenic Process Cooling. *Procedia CIRP*, 3, pp. 85-90.
- [109] Piquard, R., d'Acunto, A., Laheurte, P., Dudzinski, D. (2014) Micro-end milling of NiTi biomedical alloys, burr formation and phase transformation. *Precision Engineering*, 38(2), pp. 356-364.
- [110] Kumar, M., Bajpai, V. (2020) Experimental investigation of top burr formation in high-speed micro-milling of Ti6Al4V alloy. *Proceedings of the Institution of Mechanical Engineers, Part B: Journal of Engineering Manufacture*, 234(4), pp. 730-738.
- [111] Cedergren, S., Olovsjö, S., Sjöberg, G., Nyborg, L. (2013) The effects of grain size and feed rate on notch wear and burr formation in wrought Alloy 718. *The International Journal of Advanced Manufacturing Technology*, 67(5-8), pp. 1501-1507.
- [112] Min, S., Lee, D.E., De Grave, A., De Oliveira Valente, C.M., Lin, J., Dornfeld, D.A. (2006) Surface and Edge Quality Variation in Precision Machining of Single Crystal and Polycrystalline Materials. *Proceedings of the Institution of Mechanical Engineers, Part B: Journal of Engineering Manufacture*, 220(4), pp. 479-487.
- [113] Pramanik, A., Basak, A.K., Uddin, M.S., Shankar, S., Debnath, S., Islam, M.N. (2019) Burr formation during drilling of mild steel at different machining conditions. *Materials and Manufacturing Processes*, 34(7), pp. 726-735.
- [114] Biermann, D., Steiner, M. (2012) Analysis of Micro Burr Formation in Austenitic Stainless Steel X5CrNi18-10. *Procedia CIRP*, 3, pp. 97-102.
- [115] Schoop, J., Hasan, M.M., Zannoun, H. (2022) Physics-Informed and Data-Driven Prediction of Residual Stress in Three-Dimensional Machining. *Experimental Mechanics*, 62, pp. 1-14.
- [116] Rice, J.R., Tracey, D.M. (1969) On the ductile enlargement of voids in triaxial stress fields*. *Journal of the Mechanics and Physics of Solids*, 17(3), pp. 201-217.
- [117] Olvera, O., Barrow, G. (1998) Influence of exit angle and tool nose geometry on burr formation in face milling operations. *Proceedings of the Institution of*

Mechanical Engineers, Part B: Journal of Engineering Manufacture, 212(1), pp. 59-72.

- [118] De Souza, A.M., Sales, W.F., Ezugwu, E.O., Bonney, J., Machado, A.R. (2003) Burr formation in face milling of cast iron with different milling cutter systems. Proceedings of the Institution of Mechanical Engineers, Part B: Journal of Engineering Manufacture, 217(11), pp. 1589-1596.
- [119] Platt, T., Meijer, A., Biermann, D. (2020) Conduction-Based Thermally Assisted Micromilling Process for Cutting Difficult-to-Machine Materials. Journal of Manufacturing and Materials Processing, 4(2), pp. 34.
- [120] Group, A.M., Merwin, J.E., Johnson, K.L. (1963) An Analysis of Plastic Deformation in Rolling Contact. Proceedings of the Institution of Mechanical Engineers, 177(1), pp. 676-690.
- [121] Pomeroy, R.J., Johnson, K.L. (1969) Residual stresses in rolling contact. Journal of Strain Analysis, 4(3), pp. 208-218.
- [122] Hofman, P., Kvasnicka, I. (2000) Analytical Model for Burr Formation During Orthogonal Machining and its Verification. In: Proceedings of the 6th International Conference Precision Surface Finishing and Deburring Technology, St. Petersburg, Russia, pp. 145-158.
- [123] Hashimura, M., Hassamontr, J., Dornfeld, D.A. (1999) Effect of In-Plane Exit Angle and Rake Angles on Burr Height and Thickness in Face Milling Operation. Journal of Manufacturing Science and Engineering, 121(1), pp. 13-19.
- [124] Toropov, A.A., Ko, S.L., Lee, J.M. (2006) A New Burr Formation Model for Orthogonal Cutting of Ductile Materials. CIRP Annals, 55(1), pp. 55-58.
- [125] Abushawashi, Y.M. (2013) Modeling of Metal Cutting as Purposeful Fracture of Work Material. PhD Thesis, Michigan State University.

Hamzah Zannoun was born in Ramallah, Palestine in 1999. He immigrated to the United States with his parents in 2000, where he resides to this day. Following his graduation from STEAM Academy in May of 2017, he attended the University of Kentucky to pursue his Bachelor of Science in Mechanical Engineering, which he completed in May of 2021. Hamzah remained at the University of Kentucky to pursue his Master of Science in Mechanical Engineering, where he worked under the supervision of Professor Julius Schoop as a Research Assistant at the Institute for Sustainable Manufacturing. During his graduate studies, he authored and co-authored five peer-reviewed papers. Following his expected graduation in December of 2022, he plans to join Rolls-Royce in Indianapolis, IN as a Structural Analysis Engineer.

PUBLICATIONS

- [1] Schoop, J., Hasan, M.M., Zannoun, H. (2022) Physics-Informed and Data-Driven Prediction of Residual Stress in Three-Dimensional Machining. *Experimental Mechanics*, 62, pp. 1-14.
- [2] Zannoun, H., Okorafor, J., Asensio, T., Guedes, G., Badurdeen, F., Wang, P., Jawahir, I.S., Campana, G., Mele, M., Cimatti, B. (2023) Leveraging Insights from Unique Artifacts for Creating Sustainable Products. In: Kohl, H., Seliger, G., Dietrich, F. (Eds.) *Manufacturing Driving Circular Economy, Proceedings of the 18th Global Conference on Sustainable Manufacturing*, Berlin, Germany. To Appear in *Lecture Notes in Mechanical Engineering*.

PUBLICATIONS IN PEER REVIEW

- [3] Zannoun, H., Schoop, J. (2023) Analysis of burr formation in finish machining of nickel-based superalloy with worn tools using in-situ techniques. Submitted to the *International Journal of Machine Tools and Manufacture* 10/22.
- [4] Zannoun, H., Thornton, E., Vomero, C., Caudill, D., Schoop, J. (2023) A Review of Constitutive Models and Thermal Properties for Nickel-Based Superalloys Across Machining-Specific Regimes—Part 1. In Pre-Publication with the *Journal of Manufacturing Science and Engineering*.
- [5] Thornton, E., Zannoun, H., Vomero, C., Caudill, D., Schoop, J. (2023) A Review of Constitutive Models and Thermal Properties for Nickel-Based Superalloys Across Machining-Specific Regimes—Part 2. In Pre-Publication with the *Journal of Manufacturing Science and Engineering*.